Astronomy Reports, Vol. 48, No. 6, 2004, pp. 439–448. Translated from Astronomicheskiĭ Zhurnal, Vol. 81, No. 6, 2004, pp. 483–493.

Monitoring Compact Extragalactic Radio Sources at 4.8 and 8.6 GHz Using the 32-m Radio Telescope of the Svetloe Radio Astronomy Observatory

T. B. Pyatunina, I. A. Rakhimov, and A. A. Zborovskiĭ

Institute of Applied Astronomy, St. Petersburg, Russia

Received November 10, 2003; in final form, January 9, 2004

Abstract—We present the results of monitoring of the integrated fluxes of variable extragalactic sources at 4.8 and 8.6 GHz at the Svetloe Radio Astronomy Observatory (Institute of Applied Astronomy, Russian Academy of Sciences) from 1999 up to the present. More than 1000 observations of 36 sources have been carried out over this monitoring interval. We describe some of the most interesting flares detected in a number of sources, including the well-known objects 0851+202, 3C 345, and BL Lac. Even observations of variability at two frequencies can be very useful for planning astrophysical and astrometric observations. We briefly discuss the possibility of enhancing the effectiveness of the monitoring by expanding the range of frequencies to 22 GHz and adding polarization observations. © *2004 MAIK "Nauka/Interperiodica"*.

1. INTRODUCTION

Variability of the compact extragalactic radio sources that serve as reference sources for the radio astronomical coordinate system has been observed over a wide range of wavelengths from radio to gamma rays and is manifest on time scales from fractions of a day to several decades [1]. The fastest intraday variability is probably associated with scintillation on inhomogeneities of the medium both in the immediate vicinity of the source and in interstellar plasma between the source and observer [1], as well as by turbulence in the jets at large angular distances from the core [2]. The slower variability that is the object of our studies can be separated into "primary" variability, associated with evolution of the "central engine" itself and the generation of a disturbance at the base of the jet, and "secondary" variability, associated with the evolution of the jet during the propagation of a primary disturbance [3].

Primary variability is observed on scales from several years (e.g., ~4 yrs in the blazars 0202+149 [4] and 0059+581 [5]) to decades (≥12 yrs in 0133+476 and ≥20 yrs in 1308+326 [6]) and may be due, for example, to interactions between binary black holes and their accretion disks in the nucleus of the host galaxy [7, 8]. Secondary variability develops on scales from fractions of a year to several years and may be due to variations in the angle of the jet to the line of sight (as in the case of 4C39.25 [9]), as well as to the appearance and development of various types of instability in the jet as it propagates from the core [10, 11].

Optical and radio monitoring data show that some of the sources display periodic components in their variability (3C273 [12, 13], OJ287 [7, 14]). Quasi-periodic flux variations over comparatively short time scales, such as the variations with a period of 2.4 ± 0.2 yrs detected in 0133+476 in 1990–1999 [15], could be explained by precession of the jets (another possible case is BL Lac, with $P \sim 2$ yrs [16]). Quasi-periodic behavior in the secondary variability could likewise be associated with quasi-periodic violation of equilibrium between the jet and surrounding medium [4, 10]. However, quasi-periodicity of the primary variations (i.e., in the appearance of primary disturbances at the base of the jet; e.g., 0202+149 [4] and 0059+581 [5]) is of the most interest. Such behavior can be used to predict certain events in the source activity, enhancing the effectiveness of astrophysical observations and providing a means to study both the dynamics and evolution of the central engine as a system of black holes and the launching mechanism for the flare activity [8, 17, 18].

It is especially important for applications that variability of compact extragalactic radio sources that serve as reference sources for the high-precision radio coordinate systems is accompanied by variations in the source structure and, consequently, variations in the effective radio coordinates of the sources. These variations provide a fundamental limit to the accuracy attainable in astrometric and geodetic VLBI observations. For example, it was shown in [19] using the slowly evolving source 4C 39.25 as an example that the coordinate offset residuals can be appreciably

1063-7729/04/4806-0439$26.00

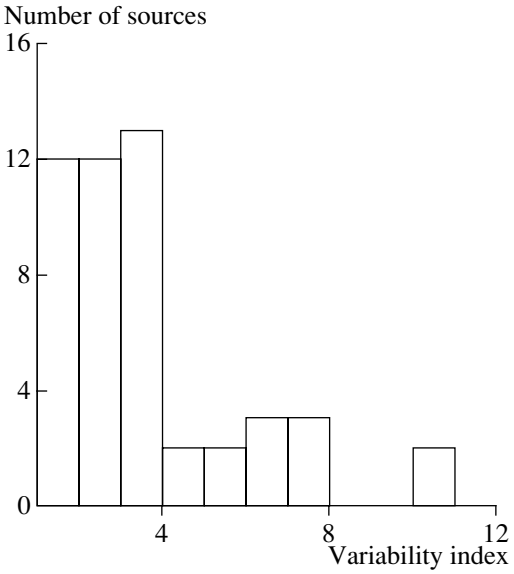

Fig. 1. Distribution of variability indices $I = S_{max}/S_{min}$ for the 50 best studied sources from the University of Michigan database.

decreased, and the precision of the coordinates accordingly increased, if corrections for the structural variations are introduced into the precomputational delays.

We should also bear in mind that variability is accompanied not only by structural variations that shift the center of brightness of the radio emission but also by variations in the absolute coordinates of the core of the radio source. The core, which is identified in VLBI-maps with the most compact optically thick feature, physically represents the part of the jet where the optical depth for radiation at the observing frequency becomes $\tau \approx 1$. In addition, as was shown by Lobanov [20], the absolute distance from the central engine to the layer with $\tau \approx 1$, and therefore the absolute position of the core on the sky, depends on the luminosity of the source as $r \propto (L)^{2/3}$. For example, when the synchrotron luminosity is doubled, the absolute distance from the central engine to the core is increased by a factor of $\sim$1.6. According to the estimates of Lobanov [20], in 3C345, the absolute distance from the core to the central engine at 8.4 GHz projected onto the celestial sphere is $\Delta r \approx (0.34 \pm 0.10)$ mas (milliarcsecond), and is shifted by $\sim$0.2 mas when the luminosity is doubled. The analogous shift at 22 GHz is $\sim$0.08 mas. Of course, these estimates are only approximations, but they show that this effect is large enough to be worthy of study, especially if we consider that about 80% of the 50 variable extragalactic sources monitored by the University of Michigan Radio Astronomy Observatory (UMRAO) [21] show flux variations by more than a factor of two (Fig. 1).

2. SOURCES

It stands to reason that relatively new monitoring program cannot compete with "veteran" programs such as that of the UMRAO [21] and the Metsahovi Radio Observatory (MRO) in Finland [22] in studies of slow processes. Therefore, we selected for our monitoring sources that have been observed to display strong variability over short time intervals of 1–3 yrs, as well as sources with detected or suspected quasi-periodic activity. Since the results of the monitoring will also be used to provide supporting information for planning of astrophysical and astrometric observations on the KVAZAR VLBI array, the list of monitored sources also included bright sources that are often used as calibrators and reference sources in astrometric and astrophysical VLBI observations, such as 0552+398 (DA 193), 0923+392 (4C39.25), 3C273, 3C279, and 3C345, as well as some peculiar objects. The initial list included 36 sources (table), but this list is currently being expanded, and we hope to appreciably increase this number in the future.

3. OBSERVATIONS

The method used for the flux calibration, including the tie between secondary calibrators and standard reference sources recommended for this purpose, and a comparison of the resulting flux scale with the flux scale of the Michigan data are presented in our earlier paper [23]. As was shown in that paper, there are no systematic differences between the two scales; the rms deviation between the scales is 8–10%, which is acceptable for variability studies. Beginning in 2002, the staff of the Nizhni Novgorod Radio Physics Institute have carried out an absolute tie of the Svetloe Observatory flux scale to the primary calibrators Cygnus A and Casseopeia A [24]. More than 1000 observations of variable sources were carried out from 1999 to 2002. The observing method is described in detail by Zborovskiĭ *et al.* [25], who also present the observing statistics for individual years.

The next section presents descriptions of the variability observed for the most interesting individual sources.

4. MOST INTERESTING EVENTS OBSERVED IN THE INTERVAL STUDIED

4.1. 0059+581

The compact, rapidly evolving source 0059+581 [26, 27] is located near the plane of the Galaxy and was recently identified with a weak, starlike object

List of studied sources

Source	Alias	Identification	z	Source	Alias	Identification	z
0016+731	–	LPQ	1.781	0945+408	4C+40.24	LPQ	1.252
0059+581	–	–	0.643	1044+719		Q	1.15
0119+041	–	QSO	0.637	1156+295	4C+29.45	HPQ	0.729
0133+476	DA 55	HPQ	0.859	1308+326	AU CVn	BLac	0.996
0146+056		QSO	2.345	1413+135		BLac	0.247
0202+149	4C+15.05	HPQ	0.833	1611+343	DA 406	LPQ	1.401
0212+735		BLac	2.367	1633+382	4C+38.41	LPQ	1.814
0336–019	CTA 26	BLac	0.852	1637+574	OS 562	LPQ	0.751
0458–020	4C-02.19	HPQ	2.286	1641+399	3C 345	HPQ	0.595
0528+134		LPQ	2.07	1739+522	OT 566	HPQ	1.375
0552+398	DA 193	LPQ	2.356	1741–038		HPQ	1.057
0605–085	OH-010	HPQ	0.87	1749+096	OT 081	BLac	0.32
0749+540	4C+54.15	BLac	–	1803+784		BLac	0.684
0804+499	OJ 508	HPQ	1.43	2007+777		BLac	0.342
0814+425	OJ 425	BLac	0.258	2145+067	4C+06.69	LPQ	0.99
0829+046		BLac	0.18	2200+420	BL Lac	BLac	0.068
0851+202	OJ 287	BLac	0.306	2201+315	4C+31.63	LPQ	0.297
0923+392	4C+39.25	LPQ	0.698	2230+114	CTA 102	HPQ	1.037

($m_V = 19.22$) with redshift $z = 0.643 \pm 0.002$ based on observations at the Special Astrophysical Observatory of the Russian Academy of Sciences, made at our request by V.L. Afanas'ev, A.I. Kopylov, and O.P. Zhelenkova. Analysis of the light curves at 4.8, 8, and 14.5 GHz (Michigan), and also at 22 and 37 GHz (Metashovi), as well as VLBI maps at 5, 8, 14.5, and 22 GHz made from data obtained from 1994 to 2002, suggest the existence of cyclic activity with a period of about four years [5]. Two flares of the radio emission are observed in each activity cycle. The first displays a time delay at low frequencies and is accompanied by an increase in the core brightness against the background of the slowly fading jet. The second flare during its decay phase is accompanied by the emergence of a fast evolving new superluminal component. Figure 2 presents the light curve for 1999–2002 for observations carried out at 4.8 and 8.6 GHz at the Svetloe Observatory. For comparison, the 37-GHz Metsahovi light curve is also shown. We can distinguish a flare associated with the optically thick (core) phase of the source evolution ($T \sim 2000.8$), and also the rising phase of a flare, which is accompanied by the emergence of a superluminal component [4, 17, 28]. The amplitude of the latter flare exceeds that of the flare accompanying the emergence of a new component in the previous cycle by nearly a factor of two, so that the time delay at low frequencies is also preserved during the rising phase of the flare. We can see in Fig. 2 that the flare maximum at 8.6 GHz is delayed relative to the maximum at 37 GHz by about 0.5 yrs. Together with the data cited above, the light curves presented here suggest that we can expect the emergence of a new jet component before the end of 2003 [5].

4.2. 0133+476

The light curve of the quasar 0133+476 (DA 55) displays a unique combination of two different forms of variability. The quasi-harmonic fluctuations of the integrated flux observed in 1990–1999 at all frequencies from 4.8 to 37 GHz [15] subsequently changed to a series of rapid (durations to 0.1 yr), chaotic flares, whose amplitudes reach 100% at 37 GHz (Fig. 2). The origin of the onset of this rapid variability could be instability of both the jet and the accretion disk.

4.3. 0336–019

The quasar 0336-019 (CTA 26) is a source of X-ray [29] and gamma-ray [30] emission. The light

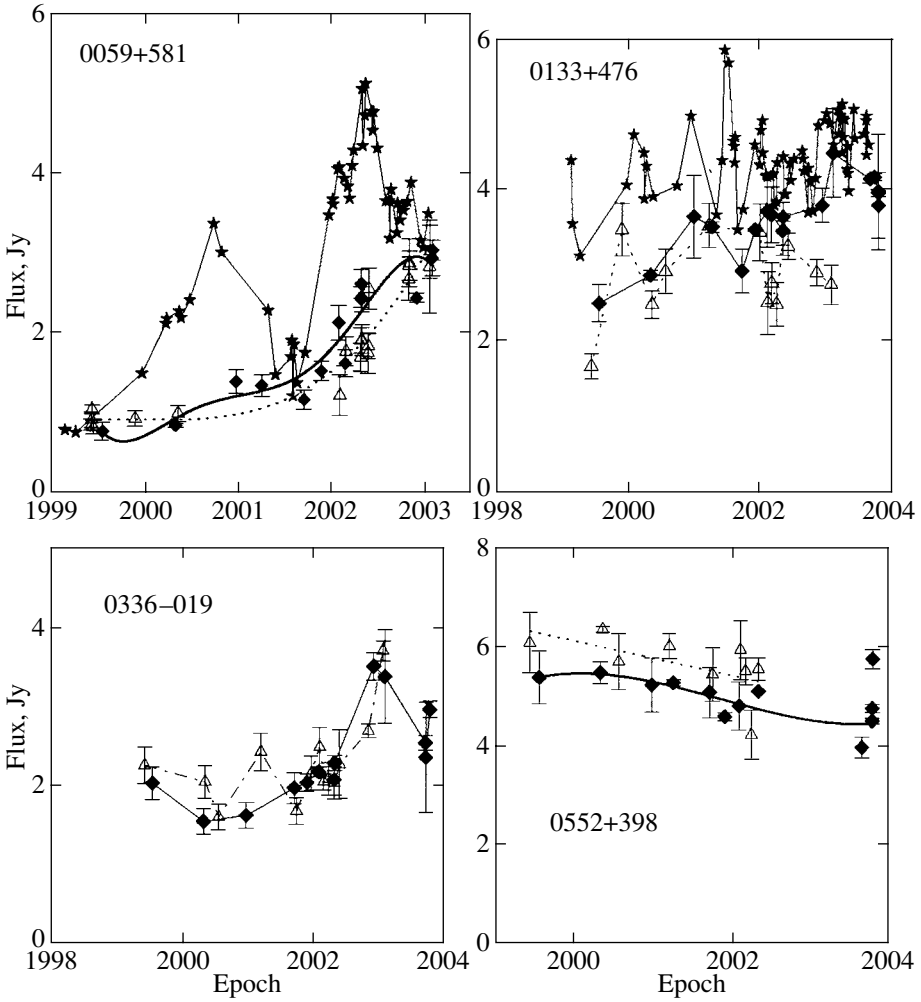

Fig. 2. Light curves for observations at the Svetloe Observatory at 8.6 GHz (filled diamonds) and 4.8 GHz (hollow triangles). Data obtained at the Metsahovi Observatory in Finland at 37 GHz are also presented for 0059+581 and 0133+476 (stars).

curve (Fig. 2) is characterized by the presence of numerous narrow subflares similar to those observed in the late stage of the evolution of 0133+476. A powerful radio flare was recorded in 2002–2004; the flux in the flare maximum, which occurred near the end of 2003, reached a value that had been achieved only once before during the ~20 yrs period of observations (in 1990). It is interesting that, according to the 24- and 43-GHz VLBI maps of the Radio Reference Frame Image Database (RRFID) of the US Naval Observatory, at least one new component appeared in the source in the interval from May to August 2002.

4.4. 0552+398

As we noted above, the compact, weakly polarized quasar 0552+398 (DA 55) is often used as a calibrator in VLBI observations. The source has a standard self-absorbed synchrotron spectrum with a turnover frequency of ~6 GHz [31] and belongs to the relatively small group of sources with gigahertz-peaked spectrum (see [32] and references therein). As a rule, these sources do not display superluminal motions. Mapping carried out using geodetic VLBI observations at 8 GHz with a resolution of ~0.6 mas [26] shows that the source consists of a core and a compact, slightly curved jet in which we were able to distinguish three components: component a, which is 0.29 mas from the core in position angle $-74°$; component b, which is 0.79 mas from the core in position angle $PA = -69.0°$; and the weak outer component c, which is 1.19 mas from the core in position angle $PA = -58°$. Thanks to the length of the available series of geodetic VLBI data, which begins in 1985 [33], it was possible to estimate the angular speed of component b relative to the core: (0.03 ± 0.01) mas/yr [26], which corresponds to an apparent linear speed of $(1.9 \pm 0.6)h^{-1}c$ for $q_0 = 0.1$. This estimate was later confirmed by Lister *et al.* [34]. The birth epoch of component a (the

epoch when its distance from the core is $R = 0$) is estimated to be in 1985. It is interesting that there is a minimum in the light curve of 0552+398 near 1985, in agreement with the suggestion made by Krichbaum *et al.* [35] that the birth epoch of a new component should coincide with a minimum in the light curve. Beginning in 1999, the light curve presented in Fig. 2 shows a gradual decrease in the flux, which may indicate that an activity cycle is in the process of ending.

4.5. 0851+202

Analysis of historical light curves of the gamma-ray blazar 0851+202 (OJ 287) reveals a period for the activity of the source in the optical of 11.9 yrs [14, 36]. The successful observations of a predicted large flare of the optical emission in 1994 in the framework of the international collaborative program "OJ-94" provided a striking confirmation of the presence of flaring with this period [7, 37]. However, the radio variability is much more complex, and the radio light curves display numerous narrow flares with durations of one to two years. Radio flares in 1995 and 1996 that are associated with the predicted large optical flare differ little from neighboring flares. The Svetloe Observatory light curves (Fig. 3) show one such flare with its maximum near 2002. The 43-GHz VLBI map from the RRFID database shows that a new component was ejected from the core in the interval from May to December 2002.

4.6. 0923+392

Like 0552+398, the weakly polarized quasar 0923+392 (4C 39.25) has its turnover frequency somewhere between 5 and 10 GHz. In addition, this is the only source whose structure has both been studied in detail [9, 38, 39] and modeled fairly reliably [19]. Apart from the core, the radio image contains the two bright quasi-stationary features *a* and *c*, which have been interpreted as places where the jet curves. A third component *b* moves between these two features. The core *d*, which has a very high turnover frequency of ~43 GHz [39], is located about 1 mas to the west of component *c*. According to [19], the position of the moving component *b* coincided with the stationary component *c* at epoch ~1982, which corresponded to a minimum in the integrated flux. The motion of component *b* from the location of component *c* further down the jet flow was accompanied by variations of the total integrated flux and the turnover frequency [9]. The turnover frequency was ~8.5 GHz at epoch 1978.04, ~5 GHz at epoch 1983.3, and ~6.5 GHz at epoch 1987.54; this can be explained as an effect of variations in the angle of the jet to the line of sight. The epoch when component *b* approached component *a* (~1998) coincides with a broad maximum in the light curve, which is followed by a gradual decrease in the integrated flux (Fig. 3).

4.7. 1156+295

The light curve of the gamma-ray blazar [42] 1156+295 displays numerous flares with durations ranging from six months to several years. Some of these flares display frequency-dependent delays. The flare shown in Fig. 3 is the most powerful flare over the 20 years of observations. The delay of the flare at 4.8 GHz may comprise two months (0.16 yr). More accurate estimation of this delay requires observations taken more frequently and with higher accuracy. Maps at 24 GHz from the RRFID database show that a new component was ejected from the core in the interval from December 2002 to May 2003.

4.8. 1308+326

Analysis of multifrequency images of 1308+326 for epochs in the interval from 1994 to 1998 [40, 41] have enabled us to trace the structure of the source in detail during a key stage in its evolution. Before ~1996, the source had a compact structure with a dominant core. A rapid expansion of the source began in 1996 and accompanied by increasing complexity of the structure and the development of an extended, diffuse jet. The light curves show that this evolution was accompanied by a decrease in the integrated flux at all frequencies from 4.8 to 37 GHz, right up until the middle of 2000. A gradual growth in the flux began in the middle of 2000 (Fig. 3), most prominently at 22 and 37 GHz. The growth in the flux at high frequencies may signal the onset of a new activity cycle.

4.9. 1633+382

The light curve of this gamma-ray quasar [42] displays several powerful, isolated flares. The brightest of these was observed near 1975, when the flux at 8 GHz reached ~5 Jy. During the period of measurements by the Svetloe Observatory, the flux remained within 2–3 Jy at both 4.8 and 8 GHz. However, the Metsahovi data presented in Fig. 4 demonstrate that the 37 GHz flux more than tripled in 2001, suggesting the appearance of a powerful component that is optically thick at the lower frequencies. The delay in the flare is probably no less than one year at 8 GHz.

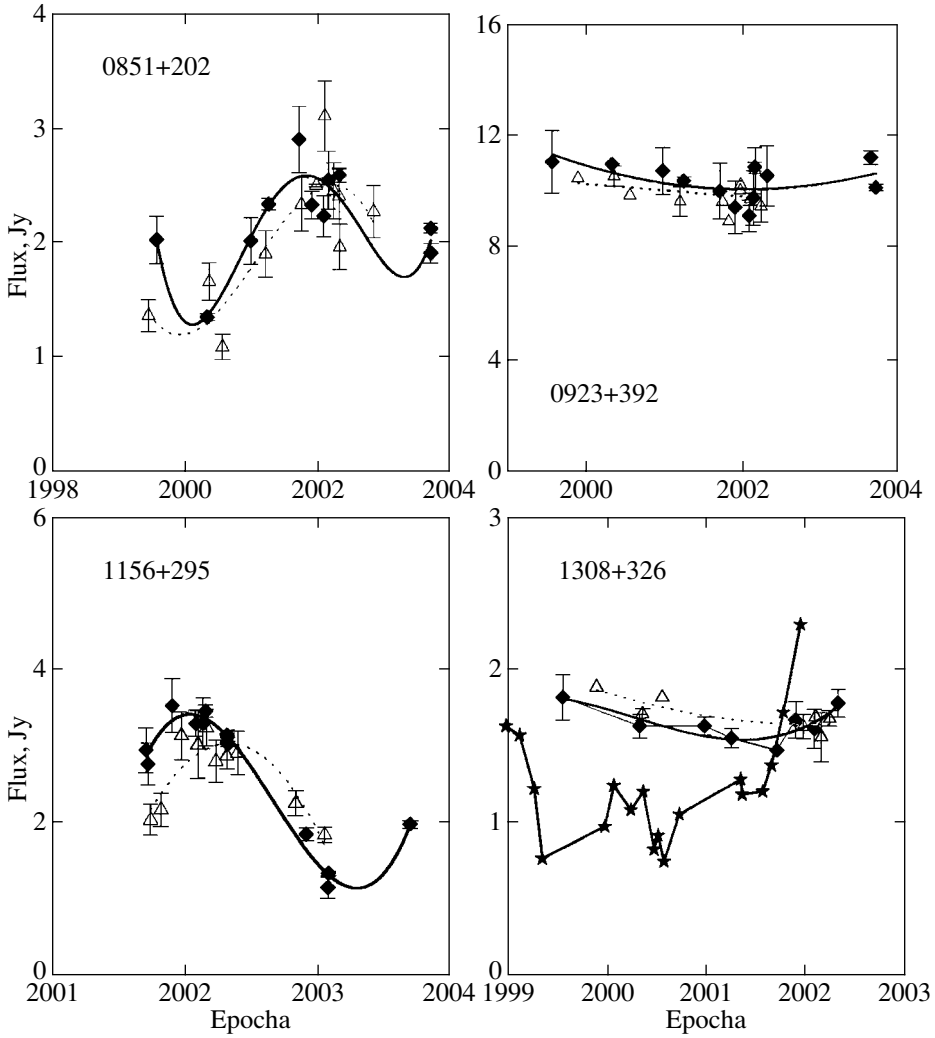

Fig. 3. Light curves for observations at the Svetloe Observatory at 8.6 GHz (filled diamonds) and 4.8 GHz (hollow triangles). Data obtained at the Metsahovi Observatory in Finland at 37 GHz are also presented for 1308+326 (stars).

4.10. 3C 345

Analysis of historical light curves revealed quasi-periodicity in the optical radiation of the quasar with a characteristic time scale of about 11 yrs [43–46]. The most recent maxima in the Michigan 8-GHz data were observed near epochs 1981.5 and 1992.5, suggesting we should expect a new maximum near 2004. The Svetloe Observatory measurements display a flare at 4.8 and 8.6 GHz with its maximum at epoch ~2001.4 (Fig. 4). The 37-GHz Metsahovi data presented on the same plot demonstrate that the 2001 flare was synchronous at frequencies from 4.8 to 37 GHz, suggesting it is associated with the final phase of an activity cycle that began with the 1992 flare.

4.11. 1739+522

The gamma-ray quasar 1739+522 (4C+51.37, OT 566) [42] has a very typical light curve, with numerous narrow subflares with durations of 2–3 months superposed on a larger-scale component; the subflares are accompanied by equally rapid variations in the spectral index [21]. The light curve in Fig. 4 shows the closing phase of a powerful flare with an amplitude of ~2 Jy and its maximum at the end of 1998, as well as a relatively small flare with its maximum in 2003.

4.12. 1741–038

The quasar 1741–038 is a source of X-ray [47] and gamma-ray [42] emission. A powerful radio flare detected at epoch 1997.1 at 37 GHz gradually "drifted" downward in frequency, and the Michigan data show that it reached its maximum at 4.8 GHz only toward epoch 1999.1. Thus, the delay of this flare was about two years at 4.8 GHz. Figure 4 shows that subsequent flares with their maxima in 2001 and 2003

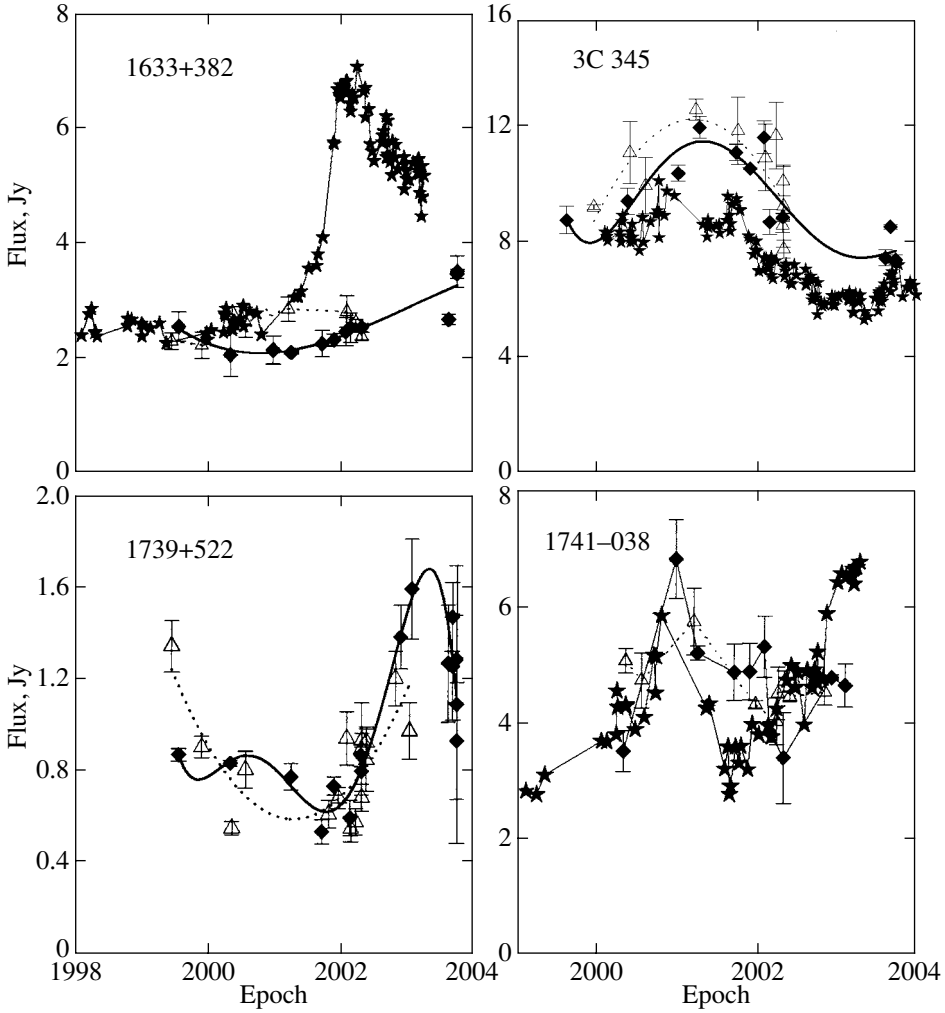

Fig. 4. Light curves for observations at the Svetloe Observatory at 8.6 GHz (filled diamonds) and 4.8 GHz (hollow triangles). Data obtained at the Metsahovi Observatory in Finland at 37 GHz are also presented for 1633+382 and 1741−038 (stars).

occurred nearly simultaneously at 37, 8, and 4.8 GHz. The fine structure in the flares is probably real, but observations with better time resolution are needed to study it. The flares are probably associated with the birth of new superluminal components and subsequent evolution of the jet.

4.13. 1803+784

The BL Lac object 1803+784 is an X-ray source [48]. The light curve presented in Fig. 5 shows what may be the final phases of a complex flare with its maximum in about 1996, as well as the beginning of a new flare.

4.14. 2145+067

The quasar 2145+067 is an X-ray source [47]. The flare we have recorded is clearly associated with the core phase of the source evolution [4, 17, 28]. The delay in the flare at 8 GHz relative to the flare observed at 37 GHz at the Metsahovi Observatory is ∼1.5 yrs (Fig. 5), and this delay may reach 2 yrs at 4.8 GHz, similar to the behavior seen in the 1997−1999 flare in the quasar 1741−038.

4.15. BL Lacertae

Analysis of optical light curves of BL Lac enabled the identification of quasi-periodic components in the brightness variations, with time scales of 7.8 yrs [14] and 14 yrs [49]. The optical, Michigan, and Metsahovi observations show that the leading maximum of the previous activity cycle occurred at the beginning of 1996. The Svetloe Observatory data display a secondary flare (Fig. 5) with its maximum near the middle of 2000. This flare occurred nearly simultaneously at all frequencies and was not accompanied by appreciable spectral variations, as is typical for the advanced phase of the activity. However, precisely

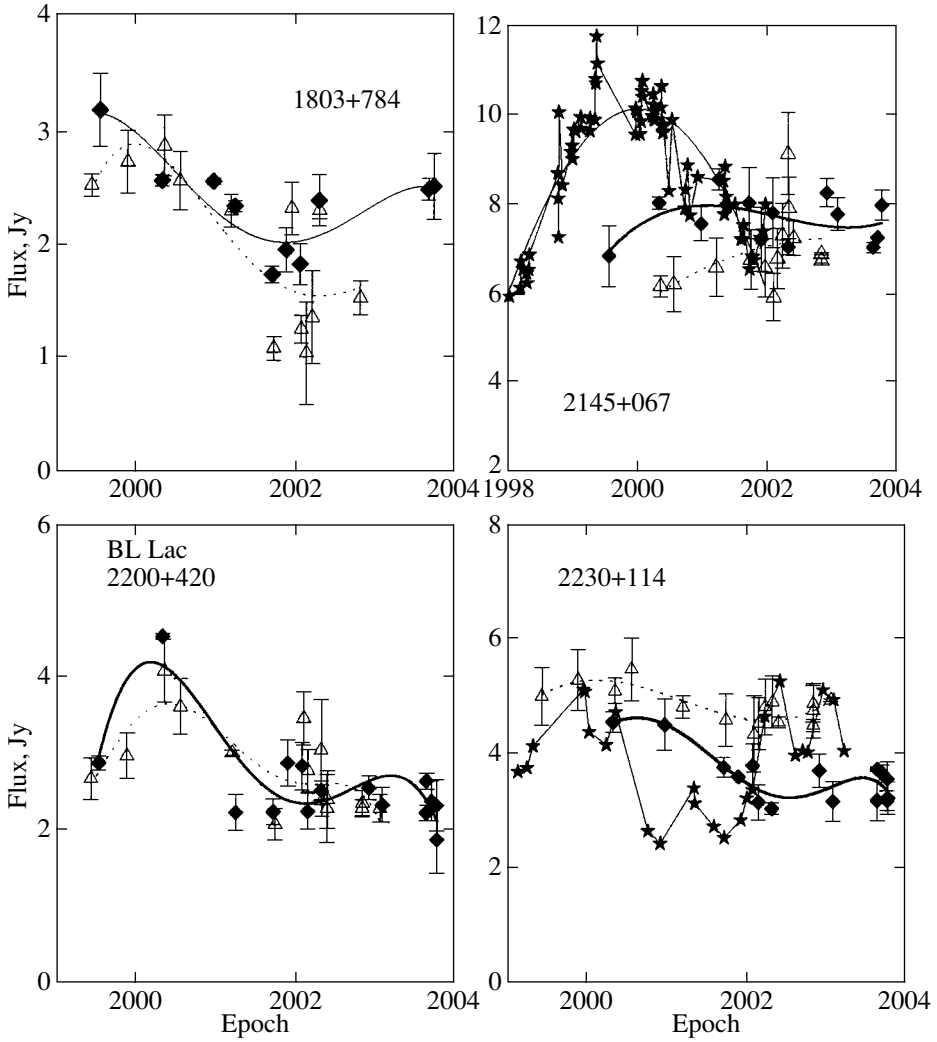

Fig. 5. Light curves for observations at the Svetloe Observatory at 8.6 GHz (filled diamonds) and 4.8 GHz (hollow triangles). Data obtained at the Metsahovi Observatory in Finland at 37 GHz are also presented for 2145+067 and 2230+114 (stars).

this phase is accompanied by rapid variations in the structure and the emergence of new components.

4.16. 2230+114

The quasar 2230+114 (CTA 102) is a source of gamma rays [42]. The Michigan and Metsahovi data show the onset in 1996 of the most powerful radio flare in this quasar observed over the past 20 years. One characteristic feature of this source is the presence of well-developed fine structure in the flares with time scales of less than one year, which is especially prominent at millimeter wavelengths [50]. This flare fine structure could be due to shocks that are formed and then decay or are disrupted at a fraction of a parsec from the central engine [51]. The change in the spectrum from optically thin (falling at short wavelengths) to optically thick (inverted) in the interval from 1996 to 1997 and the presence of a low-frequency delay provide evidence for the onset of a new activity cycle. If so, this heralds variations in the source structure on milliarcsecond scales, accompanied by the emergence of new superluminal components. The Svetloe Observatory data (Fig. 5) show the development of this flare at a late stage of its evolution. Unfortunately, the density of our measurements is not sufficient for us to analyze the fine structure of the flare and estimate the low-frequency delays of its components. However, the data demonstrate dramatic spectral variations, from optically thin between subflares with fine structure to nearly flat at the subflare maxima.

5. CONCLUSIONS

The series of observations carried out in 1999–2003 demonstrates the usefulness of monitoring the fluxes of compact extragalactic sources at the Svetloe

Observatory. Even when only two frequencies are observed, the monitoring can be used to search for new sources with periodic activity, such as 0059+581, as well as to predict the nature of future activity in specific sources and possible variations in their structure. The addition of observations at 1.35 cm (22 GHz) would enhance the trustworthiness of predictions and enable more accurate estimation of the low-frequency delays of optically thick flares, which present new possibilities for estimating the astrophysical parameters of the monitored sources.

The information produced by the monitoring would also be enhanced by carrying out polarization measurements. As has been shown by Gabuzda *et al.* [52] and Gomez *et al.* [53], radio flares associated with the birth of new superluminal components are accompanied by an increase in the degree of polarization and rotations in the polarization position angles.

Combined with maps constructed using either geodetic or astronomical VLBI data, the monitoring of integrated fluxes represents an effective means to study the activity of blazars, as well as a tool for the planning of future astrophysical and astrometric VLBI observations. Such planning is especially important for the selection of reference sources to be used in differential observations, such as observations of spacecraft relative to quasars to be used for coordinate measurements in cosmic navigation.

ACKNOWLEDGMENTS

The authors are grateful to the young staff of the Zelenchuk Observatory for the enthusiasm and persistence with which they are carrying out the labor-intensive monitoring program, and we wish them success in this endeavor. We hope that the participation of the Zelenchuk Observatory will not only expand the list of sources that will be monitored but also make it possible to attack fundamentally new problems.

We have made use of flux monitoring data obtained at the Metsahovi Radio Observatory and the University of Michigan Radio Astronomy Observatory. We have also used the Radio Reference Frame Image Database of the United States Naval Observatory. The authors thank Harri Teräsranta (MRO) and Margo and Hugh Aller (UMRAO) for their collaboration over several years and their kind presentation of the data needed for this study.

REFERENCES

1. S. J. Wagner, *BL Lac Phenomenon*, Ed. by L. O. Takalo and A. Sillanpää, ASP Conf. Ser. **159**, 279 (1999).
2. D. C. Gabuzda, P. Yu. Kochenov, T. V. Cawthorne, and R. I. Kollgaard, *BL Lac Phenomenon*, Ed. by L. O. Takalo and A. Sillanpää, ASP Conf. Ser. **159**, 447 (1999).
3. A. P. Marscher, in *Blazar Continuum Variability*, Ed. by H. R. Miller, J. R. Webb, and J. C. Noble, ASP Conf. Ser. **110**, 248 (1996).
4. T. B. Pyatunina, S. G. Marchenko, A. P. Marscher, *et al.*, Astron. Astrophys. **358**, 451 (2000).
5. T. B. Pyatunina, I. A. Rachimov, A. A. Zborovskii, *et al.*, *High Energy Blazar Astronomy*, Ed. by L. O. Takalo and E. Valtaoja, ASP Conf. Ser. **299**, 89 (2003).
6. T. B. Pyatunina, D. C. Gabuzda, S. G. Jorstad, *et al.*, *Future Directions in High Resolution Astronomy: A Celebration of the 10th Anniversary of the VLBA*, Ed. by J. Romney, ASP Conf. Ser. (2004).
7. E. Valtaoja, H. Teräsranta, M. Tornikoski, *et al.*, Astrophys. J. **531**, 744 (2000).
8. A. P. Lobanov and J. Roland, in *Proceedings of the 6th European VLBI Network Symposium*, Ed. by E. Ros, R. W. Porcas, A. P. Lobanov, and J. A. Zensus (2002), p. 121.
9. A. P. Marscher, Y. F. Zhang, D. B. Shaffer, *et al.*, Astrophys. J. **371** (2), 491 (1991).
10. J. L. Gómez, J. M. Martí, A. P. Marscher, *et al.*, Astrophys. J. **482**, L33 (1997).
11. P. E. Hardee, D. A. Clarke, and A. Rosen, Astrophys. J. **485**, 533 (1997).
12. E. T. Belokon', Astron. Zh. **68**, 1 (1991) [Sov. Astron. **35**, 1 (1991)].
13. M. K. Babadzhanyants and E. T. Belokon', Astron. Zh. **70**, 241 (1993) [Astron. Rep. **37**, 127 (1993)].
14. V. A. Hagen-Torn, S. G. Marchenko, O. V. Mikolaĭchuk, and V. A. Yakovleva, Astron. Zh. **74**, 177 (1997) [Astron. Rep. **41**, 154 (1997)].
15. T. B. Pyatunina, H. Teräsranta, E. Valtaoja, *et al.*, in *Abstracts of Joint European and National Astronomical Meeting JENAM-2000* (2000), p. 154.
16. A. M. Stirling, T. V. Cawthorne, J. Stevens, *et al.*, Mon. Not. R. Astron. Soc. **341**, 405 (2003).
17. T. B. Pyatunina, D. C. Gabuzda, and S. G. Jorstad, in *Proceedings of the All-Russian Astronomical Conference*, *2001*, p. 151.
18. T. B. Pyatunina and V. G. Grachev, in *Proceedings of the All-Russian Astronomical Conference*, *2001*, p. 151.
19. A. L. Fey, T. M. Eubanks, and K. A. Kingham, Astron. J. **114**, 2284 (1997).
20. A. P. Lobanov, Astron. Astrophys. **330**, 79 (1998).
21. H. D. Aller, M. F. Aller, G. E. Latimer, and P. E. Hodge, Astrophys. J., Suppl. Ser. **59**, 513 (1985).
22. H. Teräsranta, M. Tornikoski, A. Mujunen, *et al.*, Astron. Astrophys., Suppl. Ser. **132**, 305 (1998).
23. T. B. Pyatunina, I. A. Rakhimov, V. V. Mardyshkin, *et al.*, Tr. Inst. Prikl. Astron. Ross. Akad. Nauk **5**, 15 (2000).

24. V. P. Ivanov, S. K. Stankevich, A. V. Ipatov, *et al.*, in *Proceedings of a Russian Conference on Radio Telescopes in Commemoration of A. L. Pistol'kors, 2002*, p. 49.
25. A. A. Zborovskiĭ, I. A. Rakhimov, and T. B. Pyatunina, Soobshch. Inst. Prikl. Astron. Ross. Akad. Nauk, 161 (2004).
26. A. T. Bajkova, T. B. Pyatunina, and A. M. Finkelstein, Communications of IAA 87 (1996).
27. T. B. Pyatunina, A. M. Finkel'shteĭn, I. F. Surkis, *et al.*, Tr. Inst. Prikl. Astron. Ross. Akad. Nauk **3**, 259 (1998).
28. J. F. Zhou, X. Y. Hong, D. R. Jiang, and T. Venturi, Astrophys. J. **540**, L13 (2000).
29. J. E. Ledden and S. L. O'Dell, Astrophys. J. **298**, 630 (1985).
30. J. R. Mattox, S. Wagner, T. A. McGlynn, *et al.*, IAU Circ. **6161**, 2 (1995).
31. S. R. Spangler, R. L. Mutel, and J. M. Benson, Astrophys. J. **271**, 44 (1983).
32. C. P. O'Dea, S. A. Baum, C. Stangelini, *et al.*, Astron. Astrophys., Suppl. Ser. **84**, 549 (1990).
33. P. Charlot, Astron. Astrophys. **229**, 51 (1990).
34. M. L. Lister, A. P. Marscher, and W. K. Gear, Astrophys. J. **504**, 702 (1998).
35. T. P. Krichbaum, A. Kraus, K. Otterbain, *et al.*, *IAU Coll. No. 164: Radio Emission from Galactic and Extragalactic Compact Sources*, Ed. by J. A. Zensus, G. B. Taylor, and J. M. Wrobel, ASP Conf. Ser. **144**, 37 (1998).
36. A. Sillanpää, S. Haarala, M. J. Valtonen, *et al.*, Astrophys. J. **325**, 628 (1988).
37. A. Sillanpää, L. Takalo, T. Pursimo, *et al.*, Astron. Astrophys. **305**, L17 (1996).
38. J. M. Marcaide, A. Alberdi, J. L. Gómez, *et al.*, *Compact Extragalactic Radio Sources*, Ed. by J. A. Zensus and K. I. Kellermann (1994), p. 141.
39. A. Alberdi, J. L. Gómez, J. M. Marcaide, *et al.*, Astron. Astrophys. **361**, 529 (2000).
40. T. B. Pyatunina, Kh. D. Aller, M. F. Aller, *et al.*, Tr. Inst. Prikl. Astron. Ross. Akad. Nauk **4**, 135 (1999).
41. T. B. Pyatunina, D. C. Gabuzda, *et al.*, Astron. Astrophys. (in preparation).
42. C. von Montigni, D. L. Bertsch, J. Chiang, *et al.*, Astrophys. J. **440**, 525 (1995).
43. M. K. Babadzhanyants and E. T. Belokon', Astrofizika **23**, 459 (1985).
44. J. R. Webb, A. G. Smith, R. J. Leacock, *et al.*, Astron. J. **95**, 374 (1988).
45. X. Zhang, G. Z. Xie, and J. M. Bai, Astron. Astrophys. **330**, 469 (1998).
46. X. Zhang, G. Z. Xie, J. M. Bai, and G. Zhao, Astrophys. Space Sci. **271**, 1 (2000).
47. V. T. Junkkarinen, A. P. Marscher, and E. M. Burbidge, Astron. J. **87**, 845 (1982).
48. C. M. Urry, R. M. Sambruna, D. M. Worral, *et al.*, Astrophys. J. **463**, 424 (1996).
49. J. H. Fan, G. Z. Xie, E. Pecontal, *et al.*, Astrophys. J. **507**, 173 (1998).
50. T. B. Pyatunina, N. A. Kudryavtseva, D. C. Gabuzda, *et al.*, in *Future Directions in High Resolution Astronomy: A Celebration of the 10th Anniversary of the VLBA*, Ed. by J. Romney, ASP Conf. Ser. (2004, in press).
51. T. Savolainen, K. Wiik, E. Valtaoja, *et al.*, Astron. Astrophys. **394**, 851 (2002).
52. D. C. Gabuzda, C. M. Mullan, T. V. Cawthorne, *et al.*, Astrophys. J. **435**, 140 (1994).
53. J. L. Cómez, A. P. Marscher, and A. Alberdi, Astrophys. J. **522**, 74 (1999).

Translated by D. Gabuzda

Astronomy Reports, Vol. 48, No. 6, 2004, pp. 449–456. Translated from Astronomicheskiĭ Zhurnal, Vol. 81, No. 6, 2004, pp. 494–502.

The Structure of Cool Accretion Disks in Semidetached Binaries

D. V. Bisikalo[1], A. A. Boyarchuk[1], P. V. Kaĭgorodov[1], O. A. Kuznetsov[1,2], and T. Matsuda[3]

[1] *Institute of Astronomy, Moscow, Russia*
[2] *Keldysh Institute of Applied Mathematics, Moscow, Russia*
[3] *Kobe University, Kobe, Japan*

Received January 5, 2004; in final form, January 9, 2004

Abstract—We present a qualitative analysis of possible changes in the structure of accretion disks that occur in the transition from hot to cool disks. We suggest that an additional spiral-density wave can exist in the inner parts of the disk, where gas-dynamical perturbations are negligible. We consider the formation of this wave and its parameters. The results of a three-dimensional gas-dynamical simulation of a cool accretion disk are presented; these results confirm the possibility of the formation of a new, "precessional," spiral wave in the inner regions of a cool accretion disk. Possible observational manifestations of such a wave are discussed. © *2004 MAIK "Nauka/Interperiodica"*.

1. INTRODUCTION

The analysis of the main processes involved in heating and cooling the matter in the accretion disks of binary systems [1] has shown that, for realistic parameters of the accretion disks in semidetached binaries ($\dot{M} \simeq 10^{-12}$–$10^{-7} M_\odot$/yr and $\alpha \simeq 10^{-1}$–10^{-2}),[1] the gas temperature in the outer parts of the disk ranges from $\sim 10^4$ to $\sim 10^6$ K. Earlier, we carried out three-dimensional (3D) gas-dynamical simulations of gas flows for the cases when the temperature of the gas in the outer parts of the disk was 200 000–500 000 K (the "hot" case, [4–14]) and when this temperature did not exceed 13 600 K (the "cool" case, [1]). Analysis of these results showed that, in both cases, independent of the disk temperature, the self-consistent solution does not include a shock interaction between the stream of matter from the inner Lagrangian point L_1 and the forming accretion disk (a "hot spot"). The zone of enhanced energy release ("hot line") due to the interaction of the circumdisk halo and intercomponent envelope with the gaseous stream is located outside the disk. The hot-line model is in good agreement with observations [15–18].

For the high-temperature solutions, in addition to studying the general morphology of the gaseous flows in semidetached binaries, we investigated the structure of forming hot accretion disks (see, e.g., [14, 19]). In particular, we found that only one arm of a spiral shock is generated by the tidal influence of the mass-donating star. Two-armed spiral shocks were detected by Matsuda *et al.* [20, 22]. However, 3D gas-dynamical simulations of hot disks have shown the presence of only a one-armed spiral shock, while the structure of the flow in the region where the second arm should be present is determined by the stream from L_1, which presumably prevents the formation of the second arm of the tidally induced spiral shock. In addition, we found that, in the hot-disk case, varying the mass-transfer rate perturbs the disk, leading to the formation of a spiral-vortex structure in the disk [23, 25].

Even a glance at the morphology of the flows for the cool gas (see, e. g., [1, 25]) shows that, in this case, the accretion disk has fundamentally different parameters from the hot case. In particular, the disk is more circular and contains the second arm of the tidal spiral wave. Analysis of the results presented in [1] shows that, in contrast to the hot case, tidal spiral waves do not propagate into the inner parts of the cool accretion disk and remain in the outer parts of the disk.

The aim of the present study is to investigate the structure of cool accretion disks in semidetached binaries. Section 2 contains a qualitative analysis of possible changes occuring with the transition from the high-temperature to low-temperature solutions for the accretion-disk structure. In particular, we suggest that an additional spiral-density wave can exist in inner parts of the disk, where gas-dynamical perturbations are negligible. We consider the mechanism for the formation of this wave and its parameters. Section 3 presents the results of 3D gas-dynamical

[1] $\dot{M}$ is the mass-transfer rate and α is a dimensionless parameter in the expression for the viscosity coefficient $\nu = \alpha c_s H$ (H is the disk half-thickness and c_s the sound speed) introduced by Shakura and Sunyaev [2, 3].

1063-7729/04/4806-0449$26.00

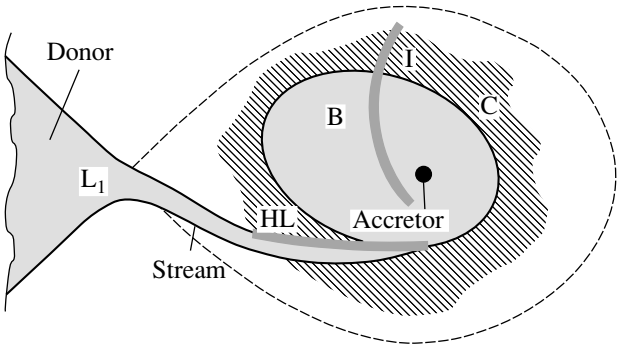

Fig. 1. Sketch of the main features of the morphology of gaseous flows in semidetached binaries for the case of high gas temperature.

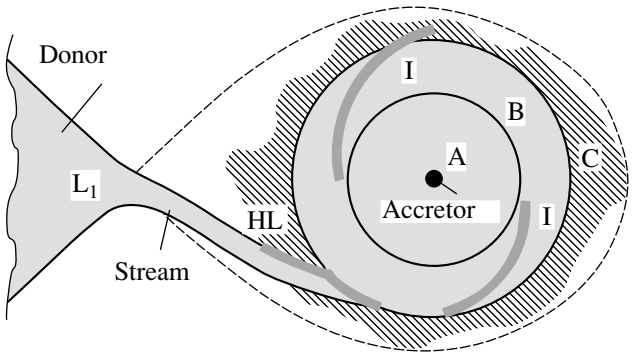

Fig. 2. Sketch of the main features of the morphology of gaseous flows in semidetached binaries for the case of low gas temperature.

simulations of the flow structure for the case when radiative cooling is efficient and the gas temperature drops to $\sim 10^4$ K in the entire computational domain. These results confirm the existence of a new type of spiral wave in the inner regions of the disk. Our main conclusions are summarized in Section 4, where we also discuss possible observational manifestations of this new "precessional" spiral wave.

2. STRUCTURE OF A COOL ACCRETION DISK. QUALITATIVE ANALYSIS

A sketch of the main features of the morphology of gaseous flows in semidetached binaries for the hot case is presented in Fig. 1. This schematic is based on the results of the 3D gas-dynamical simulations of [4–14]. Figure 1 shows a fragment of the donor star, which fills its Roche lobe, the location of the inner Lagrangian point L_1, the stream of matter from L_1, and the location of the accretor. The dashed curve shows the Roche lobe. Following the terminology of [11], the morphology of the gaseous flows in semidetached binaries is governed by the presence of a stream of matter from L_1, quasi-elliptical accretion disk, circumdisk halo, and intercomponent envelope. This classification of the main constituents of the flow is based on its physical properties: (1) if the motion of the gas is not determined by the gravitational field of the accretor, it forms an intercomponent envelope filling the space between the binary components; (2) if the gas moves around the accretor and then mixes with material from the stream, it is not captured by the accretion disk, and forms a circumdisk halo (region "C" in Fig. 1); (3) the accretion disk is formed by material from the stream that is gravitationally captured by the accretor and does not further interact with the stream, instead moving toward the accretor, losing angular momentum as it does so (region "B" in Fig. 1). The interaction of matter of the circumdisk halo and intercomponent envelope with the stream results in the formation of a shock along the edge of the stream. This shock is referred to as a "hot line" and is labelled "HL" in Fig. 1. The tidal action of the donor star leads to the formation of a spiral shock, labelled "I" in Fig. 1. Our 3D gas-dynamical simulations for the hot case show the presence of a one-armed spiral shock, while the flow structure in the region where the second arm should be located is determined by the stream from L_1. We also stress that, in this case, the spiral shock penetrates deep into the inner parts of the disk.

Let us consider the changes occurring in the transition from the high-temperature to the low-temperature solutions for the accretion-disk structure. A sketch of the main features of the morphology of the gaseous flows in semidetached binaries for the case when nonadiabatic radiative cooling reduces the gas temperature is shown in Fig. 2. Our 3D gas-dynamical simulations presented in [1] show that, when volume cooling reduces the gas temperature to $\sim 10^4$ K in the entire computational domain, the solution has the same qualitative features as in the hot case: the interaction between the stream and disk is shockless, and the region of enhanced energy release—the shock HL—is due to the interaction of the stream and circumdisk halo and is located outside the disk. This shock is fairly elongated and can be considered a hot line. At the same time, in the cool case, the accretion disk (regions "A" and "B" in Fig. 2) becomes appreciably more dense (compared to the matter in the stream); in addition, the disk is less thick and its shape changes from quasi-elliptical to nearly circular. The size of the circumdisk halo (region "C" in Fig. 2) is also considerably diminished. The second arm of the tidal spiral shock forms in the disk, but neither arm reaches the accretor, and both are located in the outer parts of the disk. Considering the weak influence of the stream on the dense inner parts

of the disk and the fact that all the shocks (the hot line and the two arms of the tidal shock) are located in the outer parts of the disk, we can distinguish an additional element of the flow structure in the cool case: the presence of an inner region of the accretion disk (region "A" in Fig. 2) where the influence of the gas-dynamical perturbations noted above can be neglected.

Let us consider the flow of matter in the inner parts of the disk that are not subject to gas-dynamical perturbations. In the absence of external forces, a gas particle will have an elliptical orbit around the gravitating center (accretor). In our gas-dynamical solutions (see Section 3), the gas particles have nearly circular elliptical orbits with the accretor located at one of the foci. It is known (see, e.g., [27, 28]) that the influence of a stellar companion leads to retrograde precession of the particle orbit, with the rate of the precession decreasing as the particle approaches the accretor according to the law

$$\frac{P_{pr}}{P_{orb}} \simeq \frac{4}{3}\frac{(1+q)^{1/2}}{q}\left(\frac{r}{A}\right)^{-3/2}, \qquad (1)$$

where P_{pr} is the period of the orbital precession, P_{orb} is the orbital period of the binary, q is the component-mass ratio, r is the orbital radius, and A is the component separation.

The accretion disk is formed by a multitude of particles, each with its own elliptical orbit. Since the particles interact and form a gas, the disk should be treated in a gas-dynamical approximation. Thus, the orbits must be replaced by streamlines that are likewise elliptical. Streamlines cannot intersect and can only touch by being tangent to each other. It is also evident from geometrical considerations that we can construct a disk from nonintersecting ellipses only by embedding them inside each other. In the case of zero eccentricity of all streamlines, we obtain a circular disk. In the case of nonzero eccentricity of the streamlines, we can construct an equilibrium solution with aligned semimajor axes for the ellipses. If there is an external force (as is unavoidable in binaries) and the orbits precess such that the precession of distant streamlines tends to be faster, these distant streamlines will constantly overtake those with smaller semimajor axes. Since the streamlines in a gas-dynamical disk cannot intersect, an equilibrium solution is established with time and all the streamlines begin to precess with the same angular velocity, i.e., to display rigid-body rotation. Accordingly, distant orbits must turn through a larger angle opposite to the direction of the rotation of the disk material, since the precession is retrograde. The precession rate is confined within the range delimited by the precession rates of the outer ("fast") orbits and inner ("slow") orbits. The inner orbits are those for which the gravitational influence of the companion is negligible compared to the gravitational influence of the accretor. The outer orbits are determined by the dimension of the region without gas-dynamical perturbations, since such perturbations would violate the regularity of the streamline precession. It is obvious that the locations of both the innermost and outermost orbits depends on the parameters of the binary system and of the mass transfer; thus, we can expect different mean precession rates in different systems.

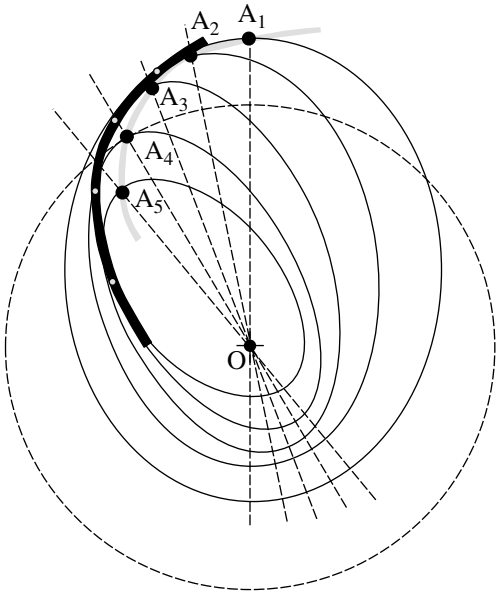

Fig. 3. Schematic of the generation of spiral structures in the inner parts of a cool disk, where gas-dynamical perturbations are negligible.

Let us consider a solution with the semimajor axes of the streamlines misaligned with respect to some chosen direction by an angle (turn angle) that is proportional to the semimajor axis of the orbit (Fig. 3). It is obvious that such a solution should contain spiral structures. In particular, due to the nonuniformity of the motion along a streamline and the formation of a maximum density at apastron, the curve connecting the apastrons (the black circles labelled A_1, A_2, ..., A_5 in Fig. 3) will form a spiral density wave. The curve connecting the places of maximum approach of the streamlines (gray circles in Fig. 3) is likewise a spiral density wave. Since the velocity of a particle (including the radial component of the velocity v_r) increases after passing apastron, we expect an increase in the radial component of the mass flux $F_{rad} = nv_r$ due to the increase of both n and v_r. Note that, if this mechanism is correct, analysis of the parameters of a gas particle moving along a streamline should first show an increase of the density (at apastron), then an increase of the radial velocity. Hence, the peaks of the radial component of the mass flux should

be located behind the density wave, and the curve passing through these peaks will also have the form of a spiral. An increase in the radial component of the mass flux behind the wave will result in an increase in the accretion rate in the region where the precessional wave approaches the surface of the accretor.

Summarizing our qualitative consideration of changes accompanying the transition from a hot to a cool accretion disk, we expect that (1) a region that is not subject to gas-dynamical perturbations appears in the cool accretion disk; (2) the retrograde precession of the particle orbits generates a spiral density wave in the inner parts of the disk that are not subject to gas-dynamical perturbations; (3) the rotational velocity of this wave is determined by the mean precession rate of the streamlines; (4) the radial component of the mass flux increases behind the density wave, with the curve connecting the peaks of the radial flux of matter also forming a spiral.

3. RESULTS OF 3D GAS-DYNAMICAL SIMULATION OF A COOL ACCRETION DISK

To further investigate the possible existence of a spiral precessional wave in the inner regions of cool accretion disks, we performed a 3D gas-dynamical simulation of the disk structure for the case when radiative cooling reduces the gas temperature to $\sim 10^4$ K in the entire computational domain. To achieve good spatial resolution in the inner part of the disk, we used a fairly fine grid ($121 \times 121 \times 32$ grid points in the X, Y, and Z directions, respectively). We adapted our code for parallel processing and executed it on supercomputers of the Moscow Supercomputer Center; this enabled us to obtain solutions with good resolution corresponding to time scales longer than the period of the disk precession.

We applied the model described in [1] for our computations. We considered a semidetached binary containing a Roche-lobe-filling donor with mass M_2 and an accretor with mass M_1. The numerical values of the system parameters are similar to those of the dwarf nova IP Peg: $M_1 = 1.02 M_\odot$, $M_2 = 0.5 M_\odot$, and binary separation $A = 1.42 R_\odot$. A finite-difference Roe–Osher method [29, 30] was used to solve the system of gas-dynamical equations including the effects of radiative cooling. The method was adapted for use on multiprocessor computers via a two-dimensional decomposition of the computational grid into subgrids with synchronization of the boundary conditions [31]. The simulations were performed using a corotating, noninertial Cartesian coordinate frame in the upper half-space (due to the symmetry of the problem about the equatorial plane). We imposed a free boundary condition at the outer boundaries: constant density ($\rho_b = 10^{-8}\rho_{L_1}$, where ρ_{L_1} is the density of the matter at L_1), constant temperature 13 600 K, and zero velocity. The stream was specified in the form of a boundary condition: matter with a given temperature, density, and velocity was injected into a zone ("spot") around L_1 with a radius of 0.014 A. The adopted parameters provided a mass-transfer rate of $\approx 10^{-9} M_\odot$/yr. The accretor was assumed to be a sphere of radius $10^{-2}A$. All matter entering any of the cells forming the accretor was taken to fall onto the star. The size of the computational domain was adjusted to contain the disk and the stream of matter from L_1. We adopted the solution for the model without cooling as the initial conditions [19]. The computer run for the model with cooling covered $\approx$10 binary periods. The total computational time on the MVS1000A supercomputer of the Moscow Supercomputer Center was $\approx$2000 hours.

The morphology of gaseous flows in the binary considered is shown in Figs. 4 and 5. Figure 4 shows the density distribution and velocity vectors in the equatorial plane of the system at $t = 1.26 P_{orb}$ and $t = 2.82 P_{orb}$. The shocks that form in the disk are visible as concentrations of the density contours. The concentrations of the contours at the edge of the circumdisk halo mark regions where the density sharply decreases to the background value. We can see that, in general, the computed flow structure is similar to the schematic in Fig. 2. A dense circular disk and compact circumdisk halo form in the system. The interaction of the gas of the circumdisk halo with the stream generates a shock—the hot line—located outside the disk. A two-armed tidal spiral shock forms in the disk; neither arm touches the accretor, and both arms are located in the outer parts of the disk. A distinctly different spiral wave is located in the region that was supposed to be unaffected by gas-dynamical perturbations in the schematic in Fig. 2. Figure 5 shows an enlarged view of the density distribution and velocity vectors in the inner part of the disk for the same times as in Fig. 4. Figures 4 and 5 show the flows in a coordinate frame that rotates with the orbital period of the binary. The two-armed spiral wave is at rest in this coordinate system, as is quite natural for a tidal wave, while the inner spiral wave moves. Analysis of the computational results shows that the wave moves as a single entity, and its velocity of revolution in the inertial frame (i.e., the observer's frame) is ≈ -0.133 of a revolution per orbital period of the binary. In other words, the spiral wave completes a revolution in the inertial frame in $\approx$7.5 binary periods, $P_{pr} \simeq 7.5 P_{orb}$. The wave ceases at a distance of $\approx 0.16\ A$ from the accretor. The precessional period for the outermost orbit computed using approximate formula (1) is $\approx 16 P_{orb}$, in agreement with the value

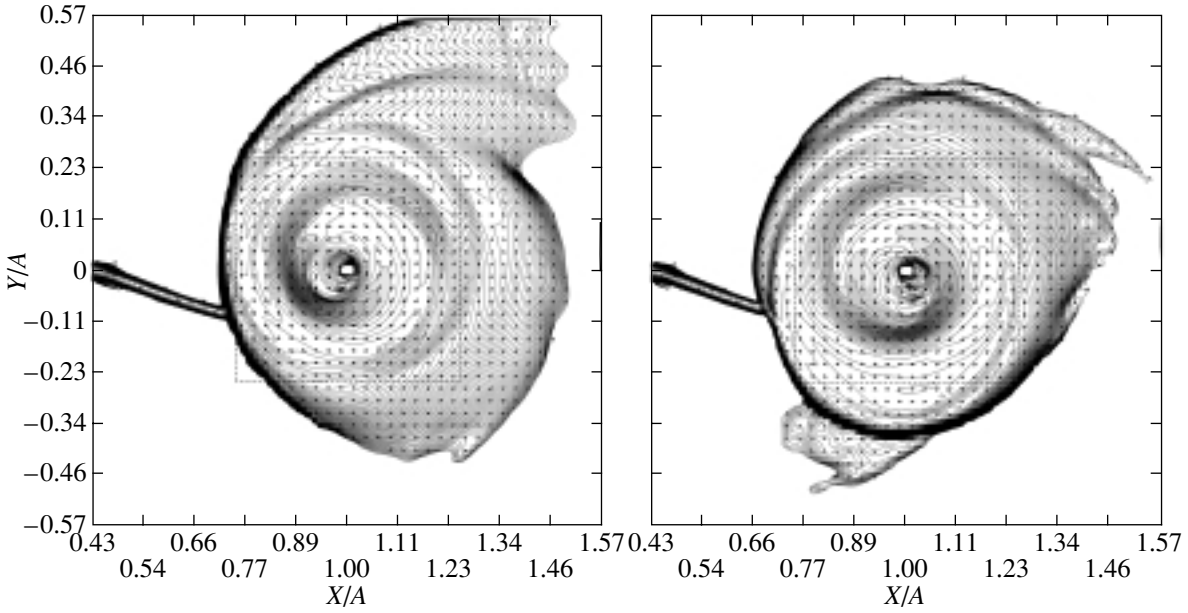

Fig. 4. Density contours and velocity vectors in the equatorial plane of a binary system for times $t = 1.26P_{orb}$ and $t = 2.82P_{orb}$.

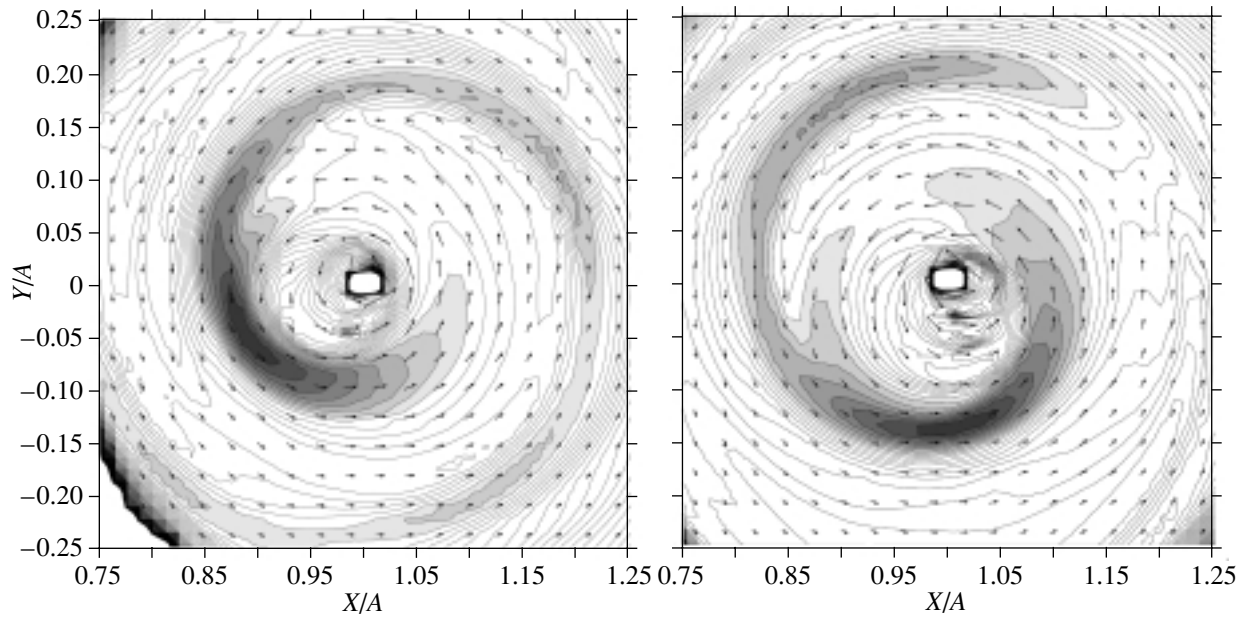

Fig. 5. Enlarged image of the region delimited by the dashed curve in Fig. 4. The structure of the flow (distribution of the density and velocity vectors) is shown for the same times as in Fig. 4.

computed in the gas-dynamical model to within a factor of two.

If the inner spiral wave is generated by precession, the computed streamlines should behave like the contours in Fig. 3. The computed streamlines in the inner parts of the accretion disk are shown in Fig. 6, which also shows the apastrons for each streamline. The shape and position of the curve passing through the apastrons match the density wave drawn in the right panel of Fig. 5 for the same time. Thus, the computed structure is in complete agreement with our qualitative analysis. The curve passing through the apastrons represents a spiral density wave, and the locations of the maximum concentration of the streamlines are detached from this wave and likewise have a spiral shape. The distributions of the density, radial

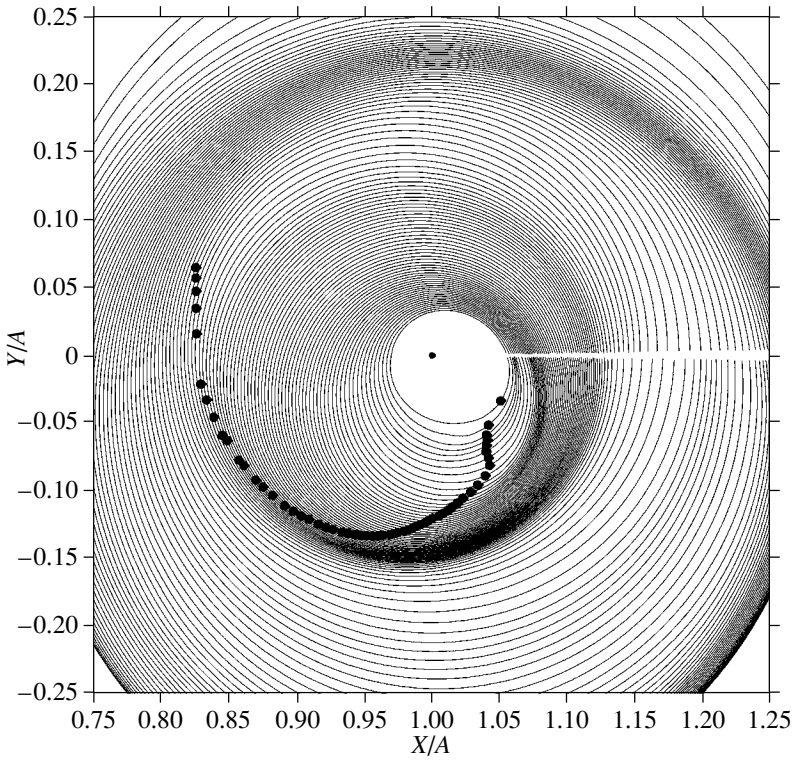

Fig. 6. Calculated streamlines in the inner part of the disk at $t = 2.82P_{orb}$. The apastrons for each streamline are shown by the black circles.

velocity, and radial flux of matter along a streamline close to the apastron also agree with the results of our qualitative analysis (see Fig. 7, which shows part of a streamline close to its apastron). Along a streamline, the density increases first (after passing apastron), after which the radial velocity likewise increases. Thus, in agreement with our expectations, the density wave precedes the peaks of the radial component of the mass flux. Figure 8 shows the distribution of the radial flux of matter in the equatorial plane of the disk at $t = 4.92P_{orb}$ in two ways; the radial flux is normalized to its maximum value. We can clearly see the spiral shape of the curve passing through the flux peaks. Due to the increase of the radial flux of matter behind the precessional density wave, the rate of accretion increases by approximately an order of magnitude compared to the wave-free solution.

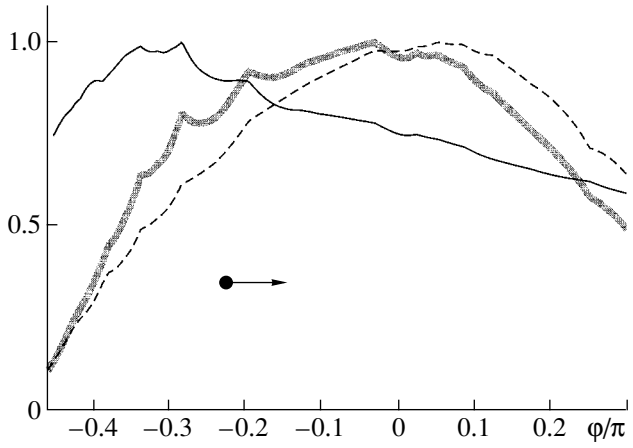

Fig. 7. Distribution of the density (thin solid curve), radial velocity (dashed curve), and radial flux of matter (bold solid line) along one of the streamlines in the vicinity of its apastron at $t = 2.82P_{orb}$. The arrow shows the direction of the motion. All distributions are normalized to their maximum values.

4. CONCLUSIONS

A qualitative analysis of possible changes in the flow structure that occur in the transition from a hot to a cool accretion disk shows that a new type of spiral wave can be generated in the accretion disk. This spiral wave in the inner parts of the disk, where gas-dynamical perturbations are negligible, is due to the retrograde precession of the streamlines in the binary system.

Analysis of the results of a 3D gas-dynamical simulation fully confirms the possibility of the generation of a spiral wave in the inner parts of a cool disk. The agreement between the qualitative analysis and the computational results makes us confident that the wave has a precessional origin. The increase in the

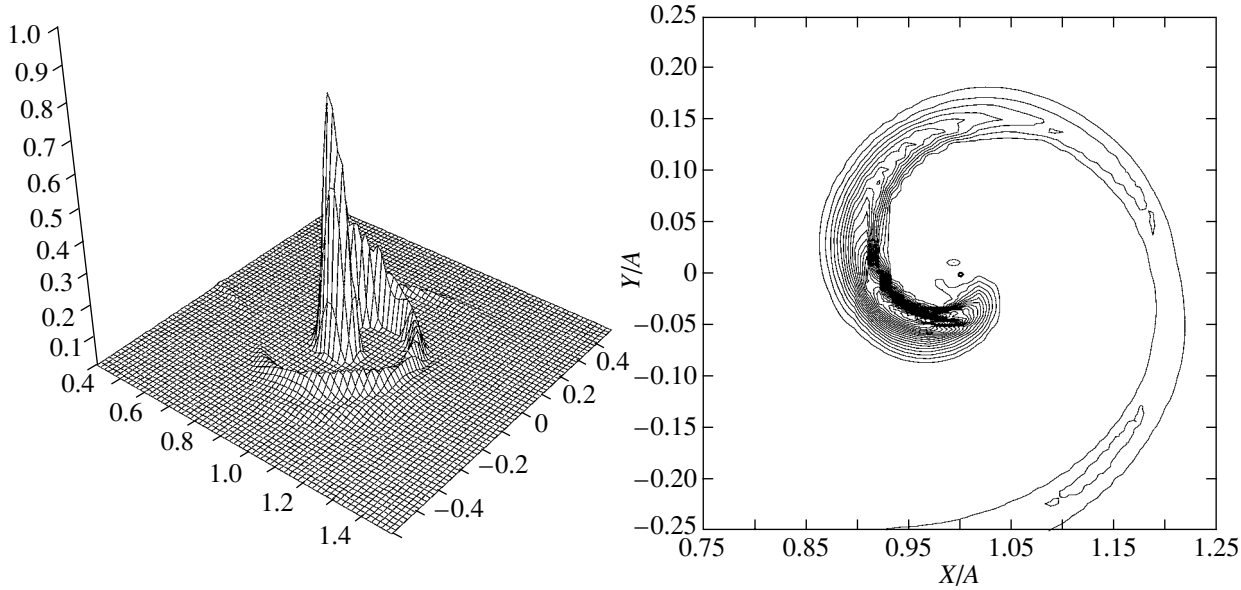

Fig. 8. Distribution of the radial flux of matter in the equatorial plane of the disk at $t = 4.92P_{orb}$. The flux is normalized to its maximum value.

radial flux of matter behind the density wave results in a growth in the accretion rate and the formation of a compact region of energy release at the surface of the accretor. This zone can be observed as a periodic brightness increase in the light curves of semidetached binaries. Observations of this region can be used to determine the precession rate of the wave, and, hence, can not only provide evidence for the existence of precessional waves in the inner parts of cool accretion disks but also be helpful in obtaining information about the characteristics of the inner parts of the disk.

ACKNOWLEDGMENTS

This work was partially supported by the Russian Foundation for Basic Research (project nos. 02-02-16088, 02-02-17642, 03-01-00311, 03-02-16622), the Program of Support for Leading Scientific Schools (project no. NSh 162.2003.2), the Federal Science and Technology Program in Astronomy, and the programs of the Presidium of the Russian Academy of Sciences "Mathematical Modeling and Intellectual Systems" and "Nonstationary Phenomena in Astronomy," and INTAS (grant no. 00-491). O.A. Kuznetsov thanks the Foundation for Support of Russian Science for financial support.

REFERENCES

1. D. V. Bisikalo, A. A. Boyarchuk, P. V. Kaĭgorodov, and O. A. Kuznetsov, Astron. Zh. **80**, 879 (2003) [Astron. Rep. **47**, 809 (2003)].
2. N. I. Shakura, Astron. Zh. **49**, 921 (1972).
3. N. I. Shakura and R. A. Sunyaev, Astron. Astrophys. **24**, 337 (1973).
4. D. V. Bisikalo, A. A. Boyarchuk, O. A. Kuznetsov, and V. M. Chechetkin, Astron. Zh. **74**, 880 (1997) [Astron. Rep. **41**, 786 (1997)].
5. D. V. Bisikalo, A. A. Boyarchuk, O. A. Kuznetsov, and V. M. Chechetkin, Astron. Zh. **74**, 889 (1997) [Astron. Rep. **41**, 794 (1997)].
6. D. V. Bisikalo, A. A. Boyarchuk, O. A. Kuznetsov, and V. M. Chechetkin, Astron. Zh. **75**, 706 (1998) [Astron. Rep. **42**, 621 (1998)].
7. D. V. Bisikalo, A. A. Boyarchuk, V. M. Chechetkin, *et al.*, Mon. Not. R. Astron. Soc. **300**, 39 (1998).
8. D. V. Bisikalo, A. A. Boyarchuk, O. A. Kuznetsov, and V. M. Chechetkin, Astron. Zh. **76**, 270 (1999) [Astron. Rep. **43**, 229 (1999)].
9. D. V. Bisikalo, A. A. Boyarchuk, O. A. Kuznetsov, and V. M. Chechetkin, Astron. Zh. **76**, 672 (1999) [Astron. Rep. **43**, 587 (1999)].
10. D. V. Bisikalo, A. A. Boyarchuk, O. A. Kuznetsov, and V. M. Chechetkin, Astron. Zh. **76**, 905 (1999) [Astron. Rep. **43**, 797 (1999)].
11. D. V. Bisikalo, A. A. Boyarchuk, O. A. Kuznetsov, and V. M. Chechetkin, Astron. Zh. **77**, 31 (2000) [Astron. Rep. **44**, 26 (2000)].
12. D. Bisikalo, P. Harmanec, A. Boyarchuk, *et al.*, Astron. Astrophys. **353**, 1009 (2000).
13. D. Molteni, D. V. Bisikalo, O. A. Kuznetsov, and A. A. Boyarchuk, Mon. Not. R. Astron. Soc. **327**, 1103 (2001).
14. A. A. Boyarchuk, D. V. Bisikalo, O. A. Kuznetsov, and V. M. Chechetkin, *Mass Transfer in Close Binary Stars* (Taylor & Francis, London, 2002).
15. D. V. Bisikalo, A. A. Boyarchuk, O. A. Kuznetsov, *et al.*, Astron. Zh. **75**, 40 (1998) [Astron. Rep. **42**, 33 (1998)].

16. T. S. Khruzina, A. M. Cherepashchuk, D. V. Bisikalo, *et al.*, Astron. Zh. **78**, 625 (2001) [Astron. Rep. **45**, 538 (2001)].
17. T. S. Khruzina, A. M. Cherepashchuk, D. V. Bisikalo, *et al.*, Astron. Zh. **80**, 194 (2003) [Astron. Rep. **47**, 214 (2003)].
18. T. S. Khruzina, A. M. Cherepashchuk, D. V. Bisikalo, *et al.*, Astron. Zh. **80**, 798 (2003) [Astron. Rep. **47**, 621 (2003)].
19. O. A. Kuznetsov, D. V. Bisikalo, A. A. Boyarchuk, *et al.*, Astron. Zh. **78**, 997 (2001) [Astron. Rep. **45**, 872 (2001)].
20. K. Sawada, T. Matsuda, and I. Hachisu, Mon. Not. R. Astron. Soc. **219**, 75 (1986).
21. K. Sawada, T. Matsuda, and I. Hachisu, Mon. Not. R. Astron. Soc. **221**, 679 (1986).
22. K. Sawada, T. Matsuda, M. Inoue, and I. Hachisu, Mon. Not. R. Astron. Soc. **224**, 307 (1987).
23. D. V. Bisikalo, A. A. Boyarchuk, A. A. Kil'pio, *et al.*, Astron. Zh. **78**, 707 (2001) [Astron. Rep. **45**, 611 (2001)].
24. D. V. Bisikalo, A. A. Boyarchuk, A. A. Kil'pio, and O. A. Kuznetsova, Astron. Zh. **78**, 780 (2001) [Astron. Rep. **45**, 676 (2001)].
25. A. M. Fridman *et al.*, Phys. Lett. A **317**, 181 (2003).
26. K. Kornet and M. Różyczka, Acta Astron. **50**, 163 (2000).
27. S. Kumar, Mon. Not. R. Astron. Soc. **223**, 225 (1986).
28. B. Warner, *Cataclysmic Variable Stars* (Cambridge Univ. Press, Cambridge, 1995).
29. P. L. Roe, Ann. Rev. Fluid Mech. **18**, 337 (1986).
30. S. R. Chakravarthy and S. Osher, AIAA Pap. No. 85-0363 (1985).
31. P. V. Kaĭgorodov and O. A. Kuznetsov, Preprint No. 59 (Keldysh Inst. Prikl. Mat., 2002).

Translated by L. Yungel'son

Astronomy Reports, Vol. 48, No. 6, 2004, pp. 457–469. Translated from Astronomicheskiĭ Zhurnal, Vol. 81, No. 6, 2004, pp. 503–516.

Analysis of the Scintillation Pattern of the Pulsar PSR B0329+54 Based on VLBI Data at 1650 MHz

K. V. Semenkov, V. A. Soglasnov, and M. V. Popov

Astro Space Center, Lebedev Institute of Physics, Russian Academy of Sciences, Profsoyuznaya ul. 84/32, Moscow, 119997 Russia

Received August 5, 2003; in final form, January 9, 2004

Abstract—The velocity of motion of the diffraction pattern of the pulsar PSR B0329+54 at 1.6 GHz has been measured. Using a specialized method for the amplitude calibration of the VLBI data, scintillation curves were obtained for the ten ground antennas that took part in the experiment jointly with the orbiting antenna HALCA. The session lasted 12 hours. Our analysis shows that the pulsar has two timescales, 20 and 1 min. The velocity of the scintillation pattern was determined by measuring the shift of the maximum of the scintillation-curve cross-correlation function relative to zero. It turned out that the scintillation spots move independently from each other: there is no ordered motion of the diffraction pattern as a whole. The measured drift velocities are from 25 to 40 km/s; the average magnitude of the drift velocity is 39 ± 15 km/s, whereas the magnitude precalculated from the pulsar proper motion taking into account the Earth's motion around the Sun and the Sun's motion with respect to the Local Standard of Rest is 122 km/s. A thin-screen model is unable to provide an adequate description of this behavior.

1. INTRODUCTION

The radio emission from a pulsar is scattered on inhomogeneities as it passes through turbulent interstellar plasma. This scattering distorts the signal, giving rise to features (maxima and minima) in the radio spectrum with a characteristic frequency scale called the decorrelation bandwidth. The lifetime of such features is characterized by a parameter called the scintillation timescale. The diffraction pattern formed in space moves with respect to the observer, so that enhancements and dips in the signal—scintillations—are observed. The origin of the motion of the diffraction pattern is the mutual movements of the source, medium, and observer with respect to each other. If the lifetime of the turbulent structure exceeds the time of the observations, we can speak of a characteristic drift velocity of the diffraction pattern, which has contributions from the relative velocities of the source, scattering medium, and observer.

In pulsar studies, the drift velocity of the diffraction pattern is used to estimate the pulsar's velocity relative to the the observer, i.e., it's proper motion. Pulsar proper motions can be determined using Very Long Baseline Interferometry (VLBI), timing data, and observations of interstellar scattering. Though the accuracy of the last method is comparatively low, it is more common. There are two generally accepted methods for measuring the drift velocity of the diffraction pattern (V_{iss}).

In the first method, developed by Rickett [1], Cordes [2], Gupta *et al.* [3], and Cordes and Rickett [4], V_{iss} is calculated from the measured scintillation timescale and the decorrelation bandwidth at a given frequency. Scintillations lead to a decorrelation of the signal in the frequency and time domains: in frequency due to loss of coherency and in time mainly due to the drift of the diffraction pattern. If, following Cordes [2], we denote the decorrelation timescale (at the $1/e$ level) by τ_d, the characteristic linear size of the spot by S_{spot}, and the decorrelation bandwidth (at the $1/2$ level) by $\delta\nu$, then

$$V_{iss} = S_{spot}/\tau_d.$$

The spatial size of the spot can be estimated indirectly by measuring the decorrelation bandwidth:

$$S_{spot} \sim \frac{\sqrt{cL\delta\nu}}{\nu},$$

where c is the speed of light in a vacuum, L is the distance to the source, and ν is the frequency of the observations. Hence,

$$V_{iss} = A_{iss}\frac{\sqrt{L\delta\nu}}{\nu\tau_d}. \quad (1)$$

The factor A_{iss} depends on the chosen model for the turbulence in the interstellar medium and the model distribution of the scattering material along the line of sight. This method yields only the magnitude of the velocity vector.

1063-7729/04/4806-0457$26.00

The other method can be considered direct measurement of the scintillation-pattern velocity. The source radiation is simultaneously received by several antennas separated by a distance that is large but does not exceed the size of the diffraction spot. The data for pairs of antennas are then correlated and the shift of the maximum of the cross-correlation function (CCF) relative to zero—the delay in the given direction—is measured. This method was used in solar-wind studies [5] and later applied to pulsar observations.

For example, Galt and Lyne [6] carried out 408 MHz observations of the pulsar PSR B0329+54 using antennas at Jodrell Bank and Penticton and attempted to estimate changes in the delay with the diurnal rotation of the Earth. The estimated velocity of the diffraction pattern was 360 km/s. Rickett and Lang [7] observed PSR B1919+21, PSR B0834+06, and PSR B1133+16 at 318 MHz over several days using antennas at Owens Valley and Arecibo. They found that the velocity of the scintillation pattern of PSR B1133+16 varied randomly during the four days of the observations. Rickett and Lang [7] proposed that such changes in V_{iss} could be due to refractive scintillations on inhomogeneities with scales of 10^6–10^7 km located comparatively close to the observer. Slee *et al.* [8] observed seven pulsars at 326 MHz using antennas in Australia and India. They proposed to estimate the delay in a given direction by measuring the coordinate τ_{ex} of the crossing point of the mean autocorrelation function with the CCF instead of the shift in the CCF maximum with respect to zero. Chasheĭ and Shishov [9] have shown that the error in the position of the CCF maximum can be fairly large in the case of low signal-to-noise ratios. Semenkov *et al.* [10] attempted to determine V_{iss} for PSR B0329+54 using the method of Galt and Lyne [6], based on observations on antennas in Eupatoria and Ussuriĭsk; however, the delays had a fairly irregular character and did not match the theoretical curve.

Recently, interest in determining the velocities of scintillation patterns has increased, since the scintillations are believed to be one possible origin of the rapid (intraday) variability observed for some extragalactic sources. In particular, by comparing light curves of PKS 0405−385 obtained simultaneously on the VLA and ATCA, Jauncey *et al.* [11] found a time delay of 140 ± 25 s between the brightness variations at these locations. Jauncey and Macquart [12] found that the time scale of the intensity variations of 0917+624 depends on the season, i.e., on the direction of the Earth's velocity. They explained this by suggesting that the source is scintillating and that the observer crosses the diffraction pattern at different velocities at different times of year and proposed a method for mapping such radio sources using annual monitoring data [13].

Multiantenna observations of the scintillation pattern provide the fundamental opportunity to measure the magnitude and direction of V_{iss} and to obtain more detailed information on the structure of the diffraction pattern.

In August 1998, VLBI observations of the pulsar PSR B0329+54 were carried out using ten ground-based antennas and the orbiting antenna HALCA. The data obtained include information on the intensity of the pulsar's radio emission at every point in the observations. We present here estimates of the magnitude and direction of the scintillation-pattern drift velocity for PSR B0329+54 derived from our analysis of these VLBI data.

2. BASIC OF THE METHOD

Consider a Cartesian coordinate frame $\{x, y, z\}$ with its origin at the Earth's center; the Z axis is directed toward the source and the X and Y axes lie in the plane of the sky. One example of such a frame is the coordinate frame used in VLBI, $\{u, v, w\}$. Let the diffraction-pattern velocity $\mathbf{V}_{iss}$ be constant. To simplify the calculations, we will assume that the X axis is aligned with $\mathbf{v}$, the component of $\mathbf{V}_{iss}$ in the XY plane. In most cases, with the possible exception of a regime in which the observer is close to the focal point, the scale of the diffraction spot along the line of sight far exceeds its scale in the plane of the sky:

$$s_z \sim k s_\perp^2,$$

where s_z is the correlation scale along the line of sight, k is the wave number, and $s_\perp$ is the field-correlation scale in the plane of the sky (see, e.g., [14, chapter II, § 9]). Therefore, we can neglect the intensity variations $\partial I/\partial z$ along the line of sight and, consequently, the contribution of the Z component of the vector $\mathbf{V}_{iss}$ to the CCF. Thus, the three-dimensional problem is reduced to a two-dimensional one.

Assuming $\mathbf{v}$ is constant, we obtain

$$I(\mathbf{r}, t) = I(\mathbf{r} - \mathbf{v}t),$$

where $\mathbf{r}$ is the radius vector and t is time. Let us calculate the CCF for a pair of antennas. Let $\mathbf{r} = \{x, y\}$ be the position vector of the first antenna and $\mathbf{r}' = \mathbf{r} + \boldsymbol{\rho} = \{x + \rho_x, y + \rho_y\}$ be the position vector of the second antenna. If the duration of the transit of the diffraction spot is much shorter than a day (in our case, 20–40 min), the Earth's rotation (time variation of the vector $\boldsymbol{\rho}$) can be neglected. We will write the cross-correlation function $C_{12}(\tau)$

$$C_{12}(\tau) = \frac{1}{T - v\tau} \qquad (2)$$

$$\times \int_0^{T-v\tau} J(x-vt,y)J(x-v(t-\tau)+\rho_x,y+\rho_y)dt,$$

where T is the duration of the spot transit, $J(x-vt,y) = I(x-vt,y) - \bar{I}$, and $\bar{I} = \int_0^T I(x-vt,y)$ is the mean intensity in the spot at a given antenna. Note that, although the integration is carried out over a time interval T equal to the total duration of the spot, the delay of interest to us is $|\tau| \ll T$. The CCF typically displays a narrow peak with a width of one point at the zero shift due to the intrinsic variability of the pulsar, which is unrelated to scattering and is identical for all antennas. We will take into account the fact that, in our case, the size of the diffraction spot far exceeds the Earth's diameter; we expand $J(\mathbf{r}+\boldsymbol{\rho},t)$ in a Taylor series and retain only linear terms. This yields

$$C_{12}(\tau) = \frac{1}{T-v\tau} \times \int_0^{T-v\tau} J(x-vt,y)J(x-v(t-\tau)+\rho_x,y)dt + \frac{1}{T-v\tau}\int_0^{T-v\tau} J(x-vt,y) \times \left.\frac{\partial J(\xi,\eta)}{\partial\eta}\right|_{\substack{\eta=y \\ \xi=x-v(t-\tau)}} \rho_y dt. \quad (3)$$

The first integral on the right-hand side of (3) is the autocorrelation function $B_J(v\tau-\rho_x)$. It has a maximum at $\tau_v = \rho_x/v$ and is symmetric about this point.

Let us examine the second integral, which we denote $C_{add}(\tau)$, in more detail. Its value depends on the shape of the diffraction spot. We assume that the brightness distribution in the spot is fairly smooth. We can then distinguish several cases:

1. The brightness distribution has circular quasi-symmetry. In this case, at small values of τ, $C_{add}(\tau) \approx 0$. The symmetry of the $C_{12}(\tau)$ curves is one indication of the reliability of the data.

2. The brightness distribution in the spot has axial quasi-symmetry. Then, $C_{add}(\tau)$ will yield a systematic shift of the CCF maximum with respect to zero by some amount τ_{geom}. The symmetry of the $C_{12}(\tau)$ curves must also be conserved.

3. The brightness distribution is irregular and complex, with "protrusions," and the symmetry is difficult to distinguish. In this case, it is difficult to interpret the shift of $C_{12}(\tau)$ with respect to zero; however, as a rule, the CCF symmetry is lost, and the criterion of delay closure (see below) ceases to operate.

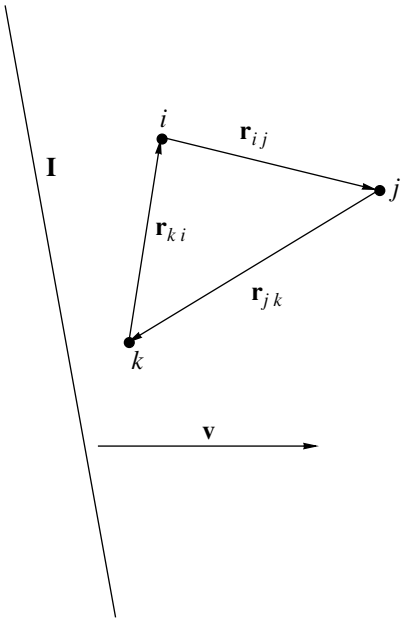

Fig. 1. Derivation of formula (4).

Suppose that the pairwise CCFs of the spot intensity have been plotted and the delays $\tau = \tau_v + \tau_{geom}$ measured. We consider the case when the diffraction spot has linear quasi-symmetry as being more general. Let $\mathbf{v}$ be the constant velocity vector of the diffraction pattern; $\mathbf{l}$ be the direction vector of the spot symmetry axis; and $\boldsymbol{r}_{ij}$, $\boldsymbol{r}_{jk}$, and $\boldsymbol{r}_{ki}$ be the baseline vectors for antennas i, j, and k.

In the configuration considered, the measured delay between antennas m and n (Fig. 1) is

$$\tau_{mn} = \frac{\mathbf{r}_{mn}\mathbf{v}_{eff}}{v_{eff}^2}, \quad (4)$$
$$\mathbf{v}_{eff} = \mathbf{v} - \mathbf{l}(\mathbf{vl}).$$

Here, parentheses denote the scalar product of two vectors and $\mathbf{v}_{eff}$ is the component of the velocity vector perpendicular to the symmetry axis, $v_{eff} = |\mathbf{v}_{eff}|$. It follows from (4) that the sum of the measured delays around any closed loop should be zero. This is the criterion of delay closure mentioned earlier. Note that, for spots with circular symmetry, $\mathbf{v}_{eff} = \mathbf{v}$. Solving a system of equations of type (4) for all pairs of antennas in the spot, we can find $\mathbf{v}_{eff}$ in this spot.

If the orientation of the symmetry axis in each of the spots is arbitrary, then averaging over a sufficient number of $\mathbf{v}_{eff}$ values calculated in different spots yields an estimate of the true velocity $\mathbf{v}$ of the diffraction pattern.

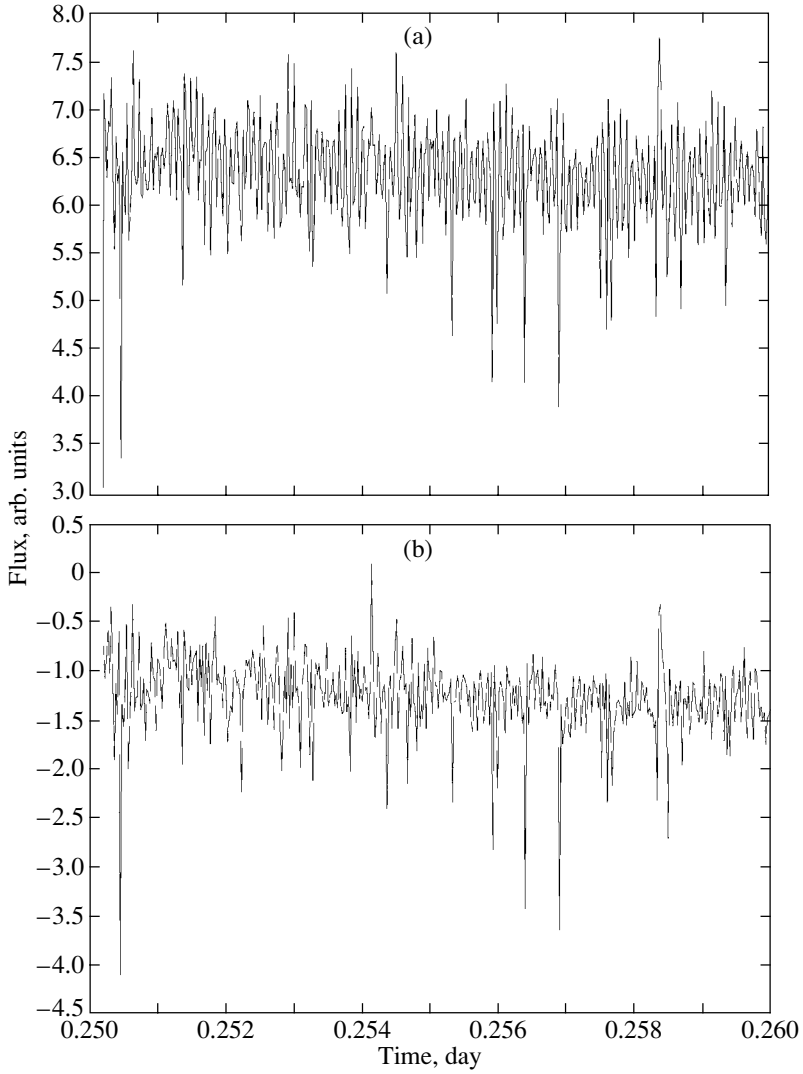

Fig. 2. Segment of the Green Bank scintillation curve in the 1634–1650-MHz band (a) before removal of the periodic component and (b) after removal of the periodic component and subtraction of the mean level.

However, the direction vector **l** of the symmetry axis can have a systematic component; i.e., the diffraction spot can be anisotropic. This systematic contribution of the structure of the diffraction pattern to the velocity vector can be eliminated using several epochs of multiantenna observations of the scintillation pattern separated by time intervals exceeding the lifetime of this anisotropic structure. Otherwise the contribution of the anisotropy of the scintillation pattern will be indistinguishable from that of the Earth's annual motion around the Sun (see also [15]).

3. OBSERVATIONS AND PRELIMINARY REDUCTION

The observations were carried out over 12 hours on August 22, 1998, with the participation of eleven antennas: the orbiting HALCA radio telescope, the 40-m Green Bank telescope, the two 70-m stations of the Deep Space Network at Goldstone and Robledo, and antennas of the Very Long Baseline Array (VLBA). The observations were carried out at 1634 MHz in two adjacent 16-MHz bands. The data were correlated on the VLBA correlator in both a gated mode (to improve the signal-to-noise ratio, only on-pulse segments of the recording were used) and the usual mode.

The preliminary amplitude calibration of the data was carried out using the technique described in [16], which we briefly describe here. The output data of the VLBI correlator contain field correlation functions for the antennas averaged over some time interval (usually several seconds; in our case, 1.96 s). In VLBI jargon, the signal autocorrelation functions obtained as a result of correlating the data for a VLBI experiment are frequently referred to as the total power of

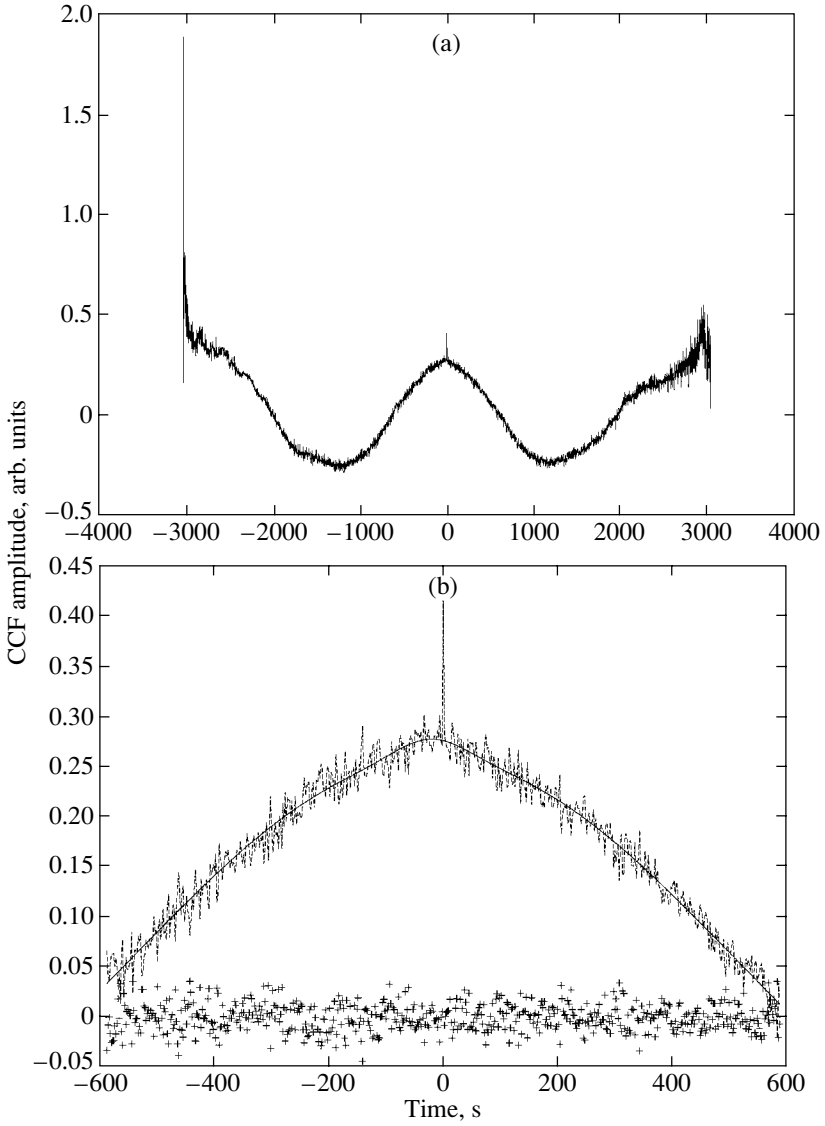

Fig. 3. Cross-correlation function for the Green Bank and Kitt Peak scintillation curves in the 1634–1650 MHz band (a) in one of the diffraction spots and (b) in its central part. In the lower panel, the dashed line shows the CCF and the solid line the approximating function calculated with (7), while the crosses show the difference between the CCF and the approximating function.

the signal, which can sometimes result in confusion. In this paper, we will stick to the standard nomenclature; i.e., we will call the autocorrelation function and intensity by precisely these terms.

Suppose that we have for each pair of antennas the autocorrelation functions A_g and A_k, obtained in the gated and usual correlation regimes, respectively. These are expressed in terms of the noise power and signal power as follows:

$$A_g = W_g S_n^2 + S_s^2,$$
$$A_k = W_k S_n^2 + S_s^2,$$
$$W_g = g W_k,$$

where W_k is the correlator integration time, W_g is the total duration of the correlator windows (gates) falling in the integration interval, S_n^2 is the noise power, and S_s^2 is the signal power, with the factor g being assumed known. Hence, the signal power in each of the correlator integration intervals is expressed as

$$S_s^2 = \frac{A_g - g A_k}{g(1-g)}. \quad (5)$$

We have developed software based on the CFITSIO subroutine library [17] that implements the above scheme. Applying formula (5) to our data, we derived scintillation curves (the time dependence of the intensity) at each of the intermediate frequencies

Table 1. Approximation of the CCF with (7)*

Antenna	2		3		4		5	
1	−1554	4.33 ± 3.94	1239	66.90 ± 8.18	−1734	-10.78 ± 2.41	717	-13.91 ± 2.29
	−1731	-18.52 ± 34.57	−225	0.97 ± 4.76	−2534	6.59 ± 2.42	51	5.72 ± 2.12
	2326		1259		3070		718	
2			2794	60.75 ± 6.91	−179	-14.69 ± 2.18	2272	-32.05 ± 5.17
			1505	-9.37 ± 5.48	−802	4.69 ± 2.54	1783	68.69 ± 38.73
			3173		821		2888	
3					−2973	−	−521	-66.21 ± 7.27
					−2308	−	277	16.15 ± 11.13
					3763		590	
4							2452	-3.96 ± 2.19
							2585	-0.84 ± 2.10
							3562	
5								
6								
7								
8								
9								

* The first column and upper line show the antenna numbers, while the cells show the antenna separations in the UV plane in kilometers and the delays in seconds (the first line in the cell gives the distance Δu and delay τ_l; the second line, the distance Δv and delay τ_s; and the third line, the distance $\Delta R = \sqrt{(\Delta u)^2 + (\Delta v)^2}$). The quoted errors are the formal errors of the approximation with (7). For a positive delay, the velocity is directed from the antenna with the smaller number to the antenna with the larger number. Dashes indicate that no reliable parameters for the approximation could be obtained for this pair of antennas. The table gives approximation results for a spot of duration from 13 h 41 m to 14 h 5 m in the frequency band 1650–1666 MHz.

for all antennas. The sensitivity of the orbiting radio telescope was not sufficient to derive its scintillation curve, and we consider further only the data from the ground antennas.

During the processing of the data, we found that a periodic component (with a period of about 40 s) was present in the scintillation curves. One possible origin for this signal is a mismatch between the actual sizes of the correlation windows and the sizes written with the correlated data. We eliminated this component by removing it from the spectrum of the scintillation curves. Figure 2 shows the retrieved scintillation curves for the ground-based antennas.

We then selected diffraction spots, in which further correlation analysis was carried out. The data were reduced to a uniform grid (the VLBI correlator outputs data with a uniform step δt and identical time markers for all antennas, but, owing to the presence of sporadic technical problems with the antennas and data filtration in the post-correlation processing, this uniformity is not present in the actual data): gaps in the data were filled with zero points. We then calcu-

6		7		8		9		11	
−636	−16.10 ± 2.39	1379	−41.99 ± 2.23	442	20.20 ± 2.11	−2114	−80.26 ± 4.07	5017	−27.12 ± 2.17
−1520	−0.37 ± 2.16	−400	−1.58 ± 1.75	−258	4.10 ± 1.68	−6737	5.35 ± 3.87	718	3.06 ± 1.97
1647		1435		511		7060		5068	
918	−21.29 ± 2.43	2934	−46.71 ± 1.80	1997	17.77 ± 1.87	−559	−91.76 ± 3.43	6572	−
210	−5.10 ± 2.69	1330	−6.24 ± 1.14	1473	0.92 ± 3.75	−5005	1.97 ± 2.90	2449	−
941		3221		2481		5036		7013	
−1876	−67.07 ± 7.30	140	−99.83 ± 8.11	−796	−36.78 ± 6.19	−3353	−	3778	−81.55 ± 7.38
−1295	0.37 ± 9.95	−174	0.12 ± 6.09	−32	−42.65 ± 5.14	−6511	−	943	−0.69 ± 5.03
2279		223		796		7323		3893	
1097	−5.62 ± 2.23	3113	−30.45 ± 2.16	2177	30.08 ± 2.06	−379	−68.96 ± 4.17	6752	−15.89 ± 2.04
1013	−8.82 ± 2.63	2133	−9.47 ± 2.11	2275	−3.07 ± 1.80	−4203	1.26 ± 4.72	3252	−3.76 ± 1.88
1493		3773		3148		4220		7494	
−1354	−0.44 ± 2.07	661	−27.31 ± 1.98	−275	35.85 ± 1.90	−2831	−64.18 ± 3.49	4300	−10.65 ± 1.90
−1572	−6.16 ± 1.75	−452	−7.85 ± 1.55	−309	−1.35 ± 1.40	−6788	−3.49 ± 3.64	666	−2.40 ± 1.50
2074		800		413		7354		4351	
		2016	−26.15 ± 1.99	1079	37.77 ± 1.93	−1477	−66.63 ± 3.77	5654	−11.70 ± 1.98
		1120	−2.60 ± 1.30	1262	4.70 ± 1.26	−5216	3.12 ± 3.17	2239	3.59 ± 1.55
		2306		1660		5421		6081	
				−936	−	−3493	−39.36 ± 3.38	3638	16.06 ± 1.91
				142	−	−6336	7.90 ± 2.73	1118	4.74 ± 1.43
				946		7235		3805	
						−2556	−104.98 ± 4.02	4575	−47.85 ± 1.82
						−6478	3.66 ± 2.98	976	−1.80 ± 1.27
						6964		4677	
								7131	55.01 ± 3.49
								7455	−3.50 ± 3.44
								10 316	

lated the CCFs of the scintillation curves in each spot:

$$C_{lm}(\tau_j) = \frac{1}{T-\tau_j} \times \sum_{i=0}^{N-1} [I_l(i\delta t) - \bar{I}_l][I_m(i\delta t - \tau_j) - \bar{I}_m], \quad (6)$$

$$N = T/\delta t,$$

$$\tau_j = j\delta t,$$

$$j = 0, \ldots, N-1,$$

where T is the duration of the diffraction spot, l and m are the antenna numbers, and $\bar{I}_l$ and $\bar{I}_m$ are the average spot intensities for antennas l and m, respectively. Figure 3 presents an example of a CCF.

The pulsar PSR B0329+54 has several scintillation scales [18], which are also present in our data (Fig. 3). Generally speaking, the diffraction-pattern velocities for these scales can differ. Analyzing a CCF with such complex structure, we will restrict ourselves to the simplest assumptions: first, that these scales are not correlated and, second, that the intensity distribution in a diffraction spot on both scales has a symmetric Gaussian pattern. The expected CCF can then be approximated by a sum of two Gaussian distributions, one broad and one narrow:

$$G(\tau) = a_1 + a_2 \exp -\frac{(\tau-\tau_l)^2}{2\sigma_l^2} + a_3 \exp -\frac{(\tau-\tau_s)^2}{2\sigma_s^2}. \quad (7)$$

We selected 14 spots in the scintillation curves, for each of which we plotted the CCF of the scintillation curves. In each CCF, we isolated the central portion, for which we determined the approximation

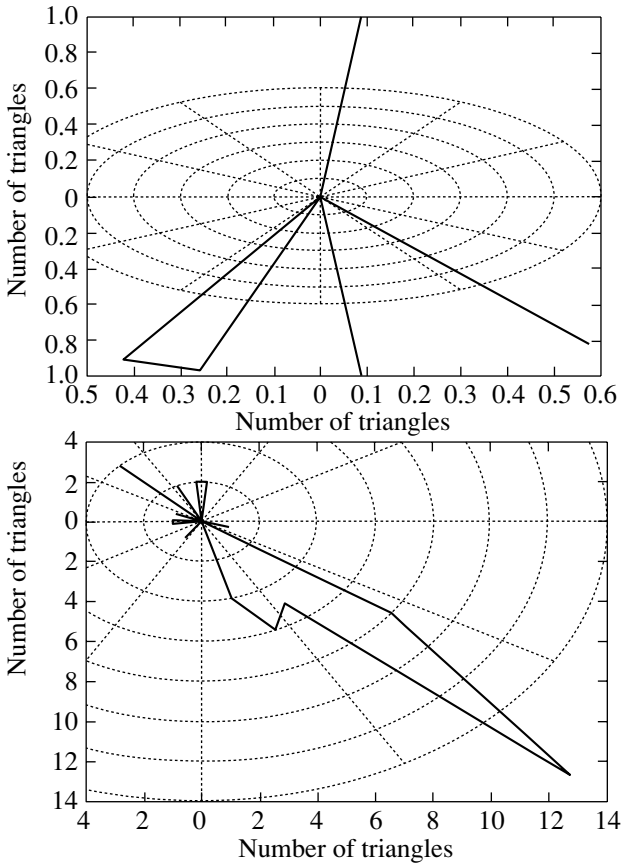

Fig. 4. Examples of the direction distributions of V_{iss}^{Δ} ("wind roses"). The upper panel shows the distribution in a spot with a duration from 10^h5^m to 10^h41^m in which there is no preferential direction of motion of the diffraction pattern. The lower panel shows the distribution in a spot with duration from 13^h41^m to 14^h5^m in which the preferential direction of motion of the diffraction pattern is obvious.

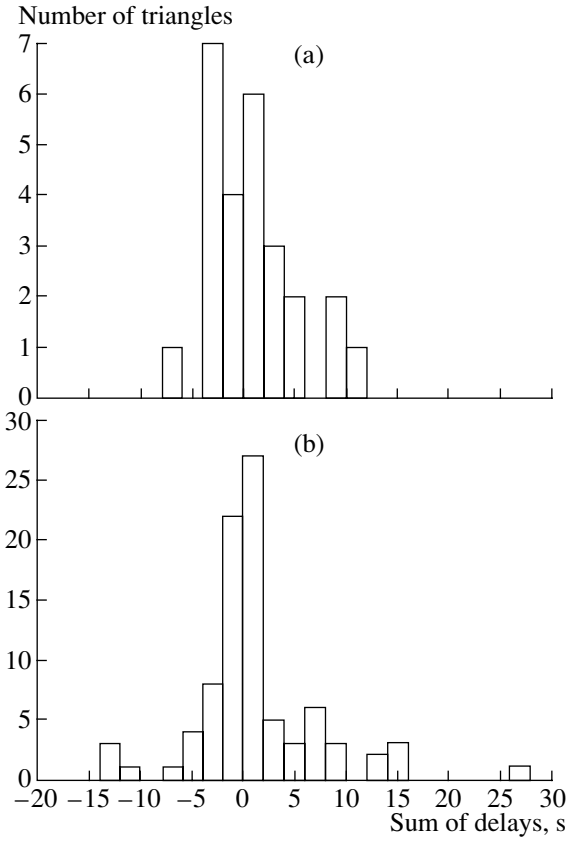

Fig. 5. Examples of closure histograms in triangles: (a) spot with duration from 6^h43^m to 7^h19^m, (b) spot with duration from 13^h41^m to 14^h5^m.

parameters. When approximating the data with (7), we discarded obviously asymmetric CCFs, for which we could not determine the parameters a_1, a_2, τ_l, and σ_l (the "narrow" scale is not manifest in all spots), as well as other CCFs for which we could not determine the parameters of the narrow scale, though it was present. Figure 3 shows an example of such an approximation. The narrow scale of the scintillations was not present in all the CCFs, but the formal determination of the approximation parameters was implemented for both scales (Table 1).

4. ANALYSIS AND DISCUSSION

The further analysis depends on the method chosen to solve system of equations (4). Of course, this system can be solved using the least-squares method, combining the data for all pairs of antennas for which the approximation parameters could be found. However, in this case, we leave out the additional information supplied by the delay-closure criterion: the contributions to the least-squares solution include the contributions of both triangles of antennas with good closure and those that do not satisfy the closure criterion. Therefore, we used another method: we solved system (4) for each triangle satisfying the delay-closure criterion and then combined these results via a least-squares solution.

We solved equations (4) in the $\{u, v, w\}$ coordinate frame widely used in VLBI, where the u and v axes lie in the plane of the sky and are directed eastward and northward, respectively, and the w axis forms a right-hand orthogonal frame with the u and v axes [19, Chapter 4].

In each spot, we derived the value of V_{iss} via a least-squares fit (V_{iss}^{LSQ}) and by solving (4) using good triangles ($\{V_{iss}^{\Delta}\}$). We used an iterative least-squares method. The solution obtained at the kth step was substituted into the initial system of equations, with equations for which

$$(\tau_i^o - \tau_i^c)^2 > 2\sigma^2 \qquad (8)$$

Table 2. Velocities of the scintillation pattern for the "broad" scale (asterisks mark spots whose velocities we consider to be trustworthy, i.e., V_{iss} satisfies the selection criteria. The position angle is measured from the u axis)

No.	Spot duration	Intermediate frequency, MHz	V^u_{LSQ}, km/s	V^v_{LSQ}, km/s	$\lvert V_{LSQ}\rvert$, km/s	p, deg	Dominant direction of the wind rose, deg
1*	6^h43^m–7^h19^m	1650	-22.0 ± 3.5	-22.8 ± 2.5	31.7 ± 3.1	-134 ± 5.5	−130
2	7^h26^m–8^h17^m	1634	23 ± 7	25 ± 6	34 ± 6	47 ± 10	–
3	7^h51^m–8^h21^m	1650	10 ± 9	-37 ± 12	39 ± 11	-75 ± 13	–
4	8^h24^m–8^h53^m	1634	-24 ± 12	-23 ± 7	34 ± 10	-135 ± 17	–
5	8^h27^m–8^h50^m	1650	8 ± 4	18 ± 3	20 ± 3	66 ± 10	−60
6	9^h7^m–9^h32^m	1634	22 ± 40	30 ± 24	37 ± 31	53 ± 53	–
7*	10^h5^m–10^h41^m	1634	-10 ± 13	-45 ± 11	46 ± 20	-103 ± 16	−105
8	11^h14^m–11^h34^m	1650	2 ± 9	45 ± 21	46 ± 21	87 ± 12	–
9	12^h43^m–12^h58^m	1634	-77 ± 115	270 ± 135	280 ± 133	106 ± 23	–
10	13^h24^m–13^h47^m	1634	-53 ± 88	120 ± 83	131 ± 84	114 ± 36	–
11*	13^h41^m–14^h5^m	1650	29 ± 4	-44 ± 5	53 ± 4	-56 ± 4	−45
12	14^h12^m–14^h36^m	1634	54 ± 12	-5 ± 17	54 ± 12	-5 ± 200	–
13*	14^h24^m–14^h54^m	1650	-9.8 ± 1.4	22.2 ± 1.4	24.2 ± 1.4	114 ± 3	115
14	16^h55^m–17^h25^m	1634	15 ± 2	-7 ± 2	17 ± 2	-25 ± 13	–

omitted. Here, τ_i^o is the experimental delay in equation i, τ_i^c is the calculated delay in this equation, and σ^2 is the dispersion of the discrepancies $(\tau_i^o - \tau_i^c)$. Further, we formed the system for the $(k+1)$th iteration step from the remaining equations. The iterative process was terminated when all equations satisfied criterion (8).

To estimate the reliability of the least-squares solutions, we plotted the angular distribution V_{iss}^{Δ} in a given spot (the wind rose, Fig. 4) for triangles for which the magnitude of the delay closure did not exceed 5 s:

$$|\tau_{12} + \tau_{23} + \tau_{31}| \leq 5 \text{ s}. \qquad (9)$$

As a rule, the formal error in the approximation parameters is about 1 s, but the sampling interval in the input data is 1.96 s; therefore, we considered selection criterion (9) to be sufficient. This is confirmed by the histograms of the closures (Fig. 5).

If the wind rose contained a dominant direction (distribution peak) and the direction of this maximum differed from that of V_{iss}^{LSQ} by no more than 20°, we took the value V_{iss}^{LSQ} to be trustworthy. If no obvious maximum was observed in the V_{iss}^{Δ} distribution or the direction of this maximum differed considerably from that of V_{iss}^{LSQ}, the value of V_{iss} in the given spot was rejected. The systems of equations were solved separately for the broad and narrow scintillation scales.

The solutions for the broad scale are listed in Table 2. For the broad scale, we could distinguish four spots with reliable values of V_{iss} (Table 2, Fig. 6).

Based on these results, we can draw the following conclusions.

First, there is no ordered motion of the diffraction pattern as a whole, although each spot moves at a constant velocity and the diffraction spot does not fade during its transit across the VLBI system (Fig. 7). The mean velocity is $\mathbf{V}_{iss} = \{-3 \pm 14, -22 \pm 12\}$ km/s, and the rms deviation of the velocity is $\{19, 27\}$ km/s. The mean magnitude of the velocity is 39 km/s, and the corresponding rms deviation is 15 km/s. It follows that the hypothesis that the motion of the diffraction pattern is ordered and frozen-in is probably incorrect. In [1, 6, 10], which present the results of measurements of V_{iss} using multiantenna data, considerable velocity jumps in different spots or in different observational sessions were noted, supporting our conclusion.

Second, let us compare our results with the predictions of the thin-screen model.

According to formula (C15) from [3], the expected velocity of the diffraction pattern V_{iss}^{exp} in the thin-screen model is estimated to be

$$\mathbf{V}_{iss}^{exp} = |x\mathbf{V}_{pm} - (1+x)(\mathbf{V}_{scr})|, \qquad (10)$$

where $\mathbf{V}_{pm}$ is the velocity of the pulsar found from its proper motion, $\mathbf{V}_{scr}$ is the velocity of the screen

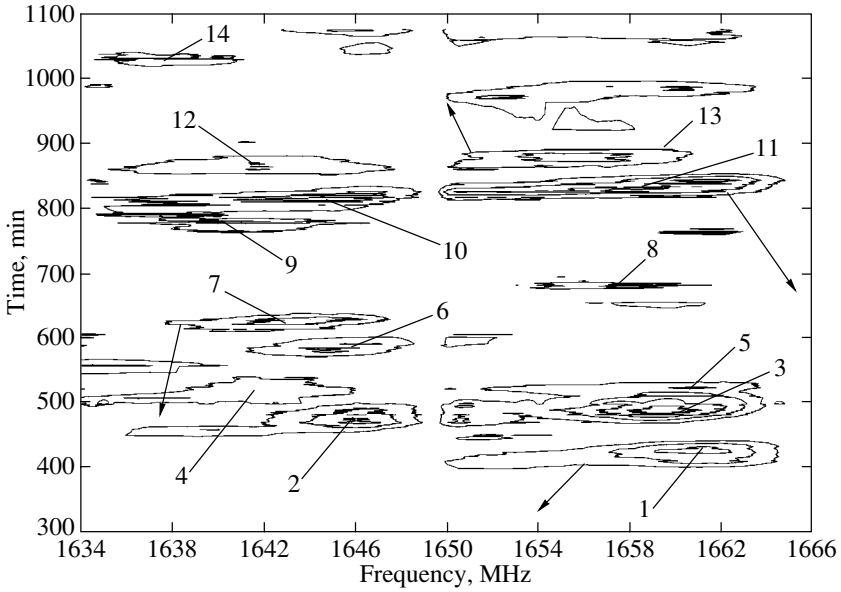

Fig. 6. Dynamic spectrum of the pulsar radio emission during the observations. The data are averaged over 1 min in time and 500 kHz in frequency. The labels denote the spot numbers in Table 2, and the arrows show the magnitudes of V_{iss} from Table 2.

with respect to the observer, and x is the ratio of the pulsar–screen distance to the screen–observer distance.

There have been several measurements of the proper motion of PSR B0329+54, collected in Table 3. In our calculations, we used the VLBI proper motion and parallax obtained by Brisken *et al.* [20]. We found the transverse velocity of the source to be

$$\mathbf{V}_{pm} = \{V^u_{pm}, V^v_{pm}\} \approx \{86, -48\}\ \text{km/s},$$

where V^u_{pm} and V^v_{pm} are the pulsar velocity components in the uv plane.

If we neglect the peculiar velocities of the screen material and the differential rotation of the Galaxy, then $\mathbf{V}_{scr} = -\mathbf{V}_{orb} - \mathbf{V}_\odot$, where $\mathbf{V}_{orb}$ is the velocity of the Earth's orbital motion around the Sun and $\mathbf{V}_\odot$ is the velocity of the Sun relative to the Local Standard of Rest (LSR). On the day of the observations (August 22, 1998), $\mathbf{V}_{orb} = \{11.9, 14.5, 22.8\}$ km/s and $\mathbf{V}_\odot = \{-14.9, 8.3, -10.2\}$ km/s in the $\{u, v, w\}$ coordinate frame.

Table 3. Determination of the pulsar proper motion and parallax

Data source	μ_α, 0.001″/year	μ_δ, 0.001″/year	π, 0.001″
[28]	17 ± 1	-12 ± 1	–
[29]	17 ± 1	-13 ± 1	–
[30]	17.3 ± 0.8	-11.5 ± 0.6	–
[20]	17.0 ± 0.3	-9.5 ± 0.4	0.94 ± 0.11

Substituting numerical values into (10) and assuming, as usual, that $x = 1$, we obtain

$$V^{exp}_{iss} = |\{80, -92.6\}|\ \text{km/s} = 122\ \text{km/s},$$

which is obviously at variance with our measurements.

Third, we plotted the spatial distribution of the brightness $S(u, v)$ in the strongest spot for the interval from 13^h41^m to 14^h5^m (Fig. 8); the recalculation to spatial coordinates was done using the formula

$$S(u, v, t) = S(u_i - V^u_{iss}(t - t_0),\ v_i - V^v_{iss}(t - t_0)),$$

where t is time, t_0 is the beginning of the spot transit interval, u_i and v_i are the coordinates of antenna i at time t_0, and V^u_{iss} and V^v_{iss} are the components of the velocity of the broad component in the scintillation pattern. The characteristic size of the spot is of the order of 60 000 km. The waves in the brightness distribution represent the small scintillation scale.

Thus, the scintillation spots in the diffraction pattern move almost independently of each other. This indicates that the thin-screen model cannot provide a full description of the properties of the scattering medium in the direction of the source. The interstellar medium in the solar neighborhood (i.e., within 1 kpc of the Sun) has a fairly complex structure, described in detail in [21]. The Sun is located in a region with a relatively low electron density (less than 0.02 cm^{-3}), the so-called "local bubble," whose size in the Galactic plane is 50–100 pc [22]. Beyond the local bubble, the integrated electron density increases. The

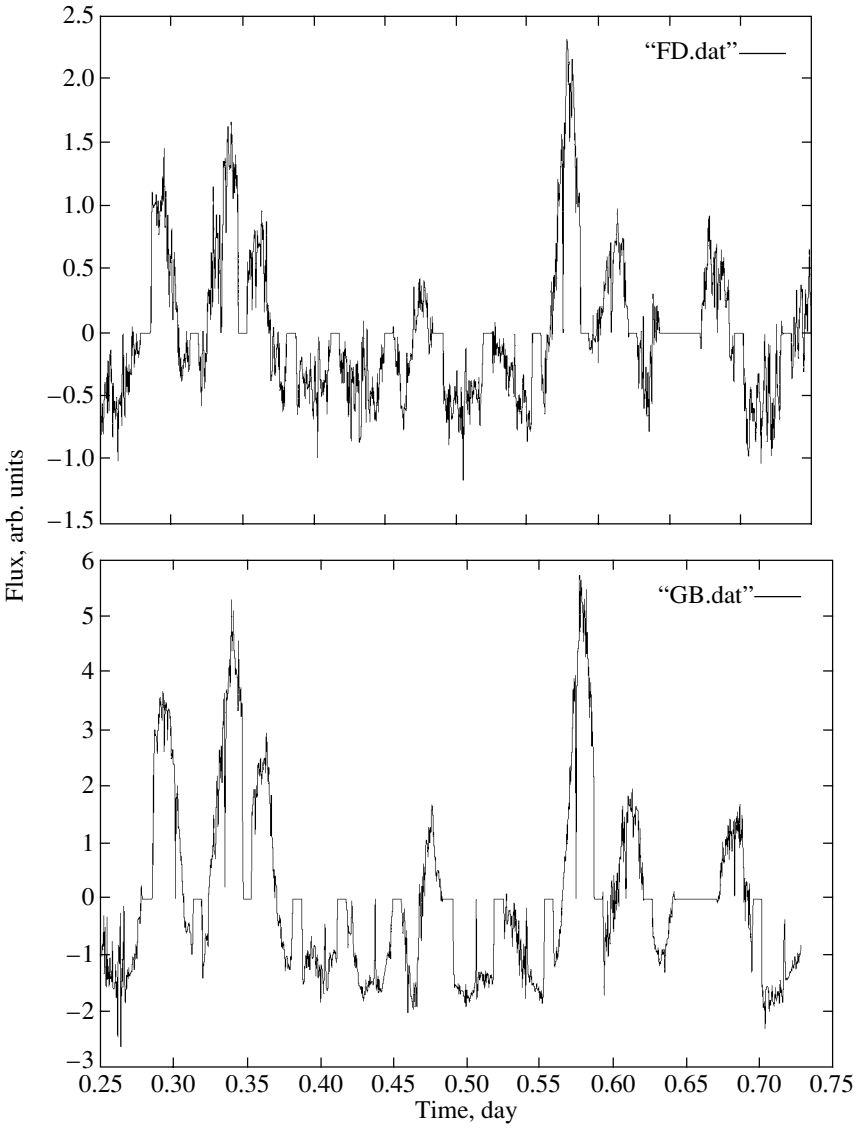

Fig. 7. Upper panel: Fort Davis scintillation curve in the 1650–1666-MHz band. Lower panel: Green Bank scintillation curve in the 1650–1666-MHz band. The data of both curves have been averaged over 40 s.

Galactic longitude and latitude of PSR B0329+54 are 144.9° and −1.9°, respectively, so that the pulsar lies nearly in the Galactic plane. According to the data of Dame *et al*. [23], there are two belts of molecular clouds in the Galactic plane, in the longitude interval $100° \leq l \leq 170°$ at distances of 300 and 800 pc from the Sun. The exact degree of ionization of the material in these regions is unknown but is estimated to be tens of percent. The velocity of the material in the clouds relative to the LSR is 10–20 km/s. In addition, according to the optical catalog of HII regions [24], there is an HII region in the direction of the pulsar—the object S203 of the Sharpless catalog [24, 25]. Its Galactic coordinates (l, b) are $(143.5°, -1.9°)$, and its angular diameter is $d = 45'$; the region is faint, circular in shape, and displays a structure that is between uniform and clumpy. Unfortunately, there are no distance estimates for this region, since its excitation source has not been found. The object appears in the radio catalog of HII regions [26, 27]; however, there are no reliable estimates of the radio size of this region.

Thus, the structure of the scattering medium in the line of sight is complex and cannot be described by a simple model with a thin phase screen as has been used in scattering studies for both pulsars and extragalactic sources [15]. Therefore, the assumption of a constant velocity of the diffraction pattern can be applied only for very nearby (<100 pc) objects if the structure of the interstellar medium between the Sun and these objects is sufficiently simple.

As we noted above, in some spots, the CCFs

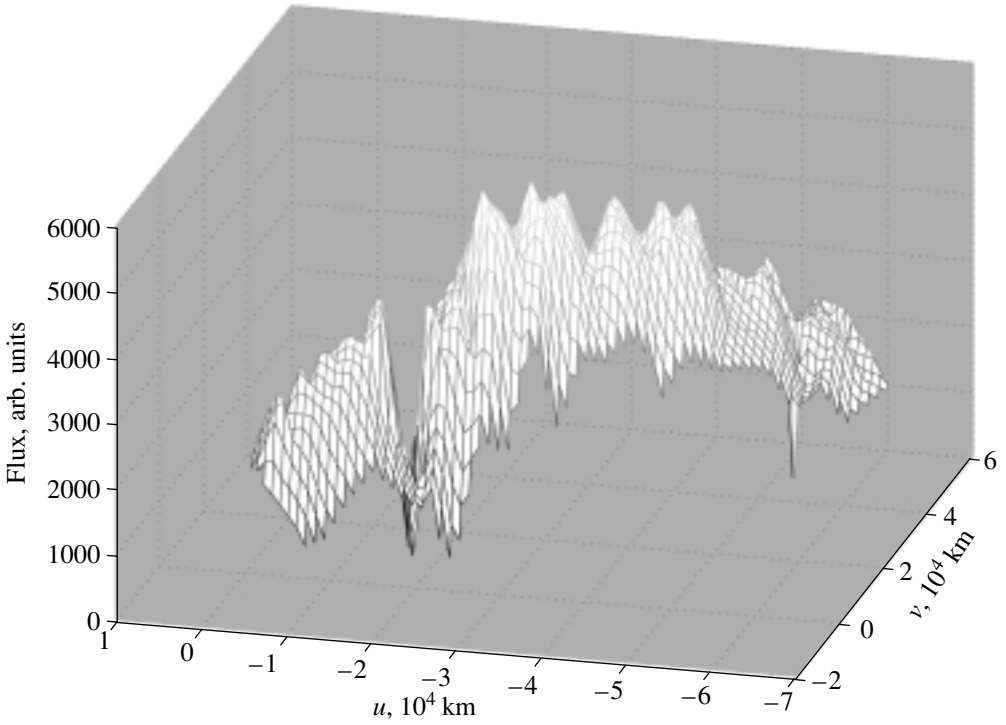

Fig. 8. Brightness distribution in the spot.

demonstrate two scintillation scales: a broad scale with a duration of about 20 min and a narrow scale with a duration of about 1 min. However, we could not find any reliable velocity for the small scale of the scintillations. We propose three explanations for this fact.

(1) The narrow scintillation scales are nonstationary; i.e., the lifetime of these scales is less than the spot transit time across the array of antennas.

(2) The narrow scales move at high velocities (hundreds of kilometers per second) with respect to the broad scales, like ripples on water, so that the delays between antennas are too small to measure using the method described in this paper.

(3) The narrow and broad scales are moving at identical velocities. In this case (Fig. 8), the spatial scale of the small structures in the diffraction pattern is ~10 000 km, which is comparable to the distance between the antennas. Therefore, methods based on the assumption that the distances between the antennas are small compared to the scale size of the diffraction pattern cannot be used.

5. CONCLUSIONS

We have used the method for the amplitude calibration of VLBI pulsar data proposed by us earlier [16] to obtain scintillation curves for each of ten ground-based antennas involved in our VLBI observations. We extracted the pulsar signal power (obtained a record of the source intensity) from the standard autocorrelation functions derived during the correlation of the VLBI data.

As a result, we effectively had two experiments in one: multiantenna measurements of the scintillation curves of PSR B0329+54 together with a usual VLBI experiment. The multiantenna measurements of the scintillation curves enabled us to directly measure the velocity of diffraction pattern with respect to the observer by determining the difference between the arrival times of the diffraction spots at the observation points. Our experiment differs from similar previous observations of pulsars [1, 6, 7, 10] and extragalactic sources [11, 12, 15] in that we have studied the spatial structure of the scintillations using the data from ten antennas simultaneously, instead of only a few. Our analysis (see Section 2) demonstrates that diffraction-pattern drift velocities derived from two-antenna observations are not trustworthy.

In total, we isolated 14 diffraction spots, in each of which we correlated the data between all pairs of antennas. On some spots, the CCFs show the presence of two scintillation scales (20 and 1 min). The shift of the cross-correlation maxima was determined separately for each of these scales. Then, using the method described in Section 4, we found for each of the spots the direction and magnitude of V_{iss}. We consider the diffraction-pattern velocities for

four spots to be trustworthy, in accordance with the selection criteria.

We derived the spatial distribution of the flux density in one of the diffraction spots (Fig. 8). The projected size of the spot at 1650 MHz is about 60 000 km.

However, we found (Table 2, Fig. 6) that the spots move independently of each other, so that there is no ordered motion of the diffraction pattern as a whole. We suggest that the thin-screen model widely used to analyze the spatial structures of scintillation patterns is not able to provide a full description of the phenomenon we are studying, since the structure of the interstellar medium in the near neighborhood of the Sun is quite complex [21]. We suggest that the assumption that the diffraction pattern moves as a whole can be used only for nearby (up to 100 pc) sources.

ACKNOWLEDGMENTS

This work was supported by the Russian Foundation for Basic Research (project no. 01-02-16871) and the Program of the Presidium of the Russian Academy of Sciences on Nonstationary Phenomena in Astronomy. The authors are grateful to the VSOP project, operated by the Japanese Institute of Space and Astronautical Science jointly with many organizations and radio telescopes around the world.

REFERENCES

1. B. J. Rickett, Mon. Not. R. Astron. Soc. **150**, 67 (1970).
2. J. M. Cordes, Astrophys. J. **311**, 183 (1986).
3. Y. Gupta, B. J. Rickett, and A. G. Lyne, Mon. Not. R. Astron. Soc. **269**, 1035 (1994).
4. J. M. Cordes and B. J. Rickett, Astrophys. J. **507**, 846 (1998).
5. J. R. Jokipii, Ann. Rev. Astron. Astrophys. **11**, 1 (1973).
6. J. A. Galt and A. G. Lyne, Mon. Not. R. Astron. Soc. **158**, 281 (1972).
7. B. J. Rickett and K. R. Lang, Astrophys. J. **185**, 945 (1973).
8. O. B. Slee, J. G. Ables, R. A. Batchelor, *et al.*, Mon. Not. R. Astron. Soc. **167**, 31 (1974).
9. I. V. Chasheĭ and V. I. Shishov, Pis'ma Astron. Zh. **1**, 18 (1975) [Sov. Astron. Lett. **1**, 9 (1975)].
10. K. V. Semenkov, M. V. Popov, and V. A. Soglasnov, Pis'ma Astron. Zh. **24**, 536 (1998) [Astron. Lett. **24**, 460 (1998)].
11. D. L. Jauncey, L. L. Kedziora-Chudczer, J. E. J. Lovell, *et al.*, in *Proceedings of the VSOP Symposium*, Ed. by H. Hirabayashi, P. G. Edwards, and D. W. Murphy (Inst. Space Astronaut. Sci., Sagamihara, Japan, 2000), p. 147.
12. D. L. Jauncey and J.-P. Macquart, Astron. Astrophys. **370**, L9 (2001).
13. J.-P. Macquart and D. L. Jauncey, Astrophys. J. **572**, 786 (2002).
14. S. M. Rytov, Yu. A. Kravtsov, and V. I. Tatarskiĭ, *Introduction to Statistical Radio Physics* (Nauka, Moscow, 1978), Part II [in Russian].
15. B. J. Rickett, A. Witzel, A. Kraus, *et al.*, Astrophys. J. **550**, L11 (2001).
16. K. V. Semenkov, M. V. Popov, V. A. Soglasnov, and H. Hirabayashi, Pis'ma Astron. Zh. **29**, 116 (2003) [Astron. Lett. **29**, 96 (2003)].
17. *CFITSIO—A FITS File Subroutine Library*; http://heasarc.gsfc.nasa.gov/docs/software/fitsio/fitsio.html.
18. V. I. Kondratiev, M. V. Popov, V. A. Soglasnov, and S. V. Kostyuk, Astrophys. Space Sci. **278**, 43 (2001).
19. A. R. Thompson, J. M. Moran, and G. W. Swenson, Jr., *Interferometry and Synthesis in Radio Astronomy* (Wiley, New York, 1986; Mir, Moscow, 1989).
20. W. F. Brisken, J. M. Benson, and W. M. Goss, Astrophys. J. **571**, 906 (2002).
21. P. C. Frisch, astro-ph/9705231.
22. S. L. Snowden, D. P. Cox, D. McCammon, and W. T. Sanders, Astrophys. J. **354**, 211 (1990).
23. T. M. Dame, H. Ungerechts, R. S. Cohen, *et al.*, Astrophys. J. **322**, 706 (1987).
24. S. Sharpless, Astrophys. J., Suppl. Ser. **4**, 257 (1959).
25. Electronic Catalogue of HII-Regions (look [24]): http://cdsweb.u-strasbg.fr/viz-bin/Cat?VII/20.
26. R. Paladini, C. Burigana, R. D. Davies, *et al.*, Astron. Astrophys. **397**, 213 (2003).
27. Electronic Catalogue (look [26]): http://cdsweb.u-strasbg.fr/viz-bin/Cat?J/A.
28. A. G. Lyne, B. Anderson, and M. J. Salter, Mon. Not. R. Astron. Soc. **201**, 503 (1982).
29. P. A. Harrison, A. G. Lyne, and B. Anderson, Mon. Not. R. Astron. Soc. **261**, 113 (1993).
30. M. Sekido, M. Imae, Y. Hanado, and Yu. P. Ilyasov, Publ. Astron. Soc. Jpn. **51**, 595 (1999).

Translated by G. Rudnitskiĭ

Astronomy Reports, Vol. 48, No. 6, 2004, pp. 470–475. Translated from Astronomicheskiĭ Zhurnal, Vol. 81, No. 6, 2004, pp. 517–522.

Optical Properties of the Circumstellar Dust around Stars with Aperiodic Fadings

A. F. Pugach

Main Astronomical Observatory, ul. Akademika Zabolotnogo 27, Kiev, 03680 Ukraine

Received August 3, 2003; in final form, January 9, 2004

Abstract—Multicolor observations of 21 rapid, irregular variable stars with Algol-like fadings and of R Coronae Borealis are used to derive the optical extinction coefficients of the circumstellar dust associated with these objects, $\theta(\lambda)$. We used more than 3600 uniform multi-color brightness measurements obtained in a rigorous $UBVR$ system at the Terskol High-altitude Observing Station. The mean extinction coefficient θ for the circumstellar dust for this sample of stars coincides almost exactly with the interstellar extinction coefficient, θ_{is}, but is somewhat higher in the ultraviolet. We suggest an explanation for this difference. © *2004 MAIK "Nauka/Interperiodica".*

1. INTRODUCTION

Although there is no universal opinion about the mechanism inducing the variability of rapid, irregular variable stars with Algol-like fadings (which we will call antiflare stars), it is currently believed that the acting factor is circumstellar dust. Variability models differ in their descriptions of the structure of circumstellar dust. The most widespread model, which is based on photometric and polarimetric observations, includes an equatorial dust disk with a nonuniform density oriented so that the line of sight is in or near the plane of the disk [1, 2]. An alternative is that the variability is due to an eruptive process on the stellar surface [3], similar to the mechanism acting in R CrB stars, in which each global fading is due to the appearance of an individual absorbing dust cloud in the line of sight [4]. Another possibility is the presence of comet-like clouds orbiting the star in highly eccentric orbits, which enter the line of sight from time to time [5, 6]. Knowledge of the optical properties of the dust could help distinguish between different variability models, since these properties are associated *a priori* with the origin of the dust itself. However, this question is not clear at the present. Different researchers have very different opinions about the optical properties of the dust, which range from proposing unusual properties for the dust surrounding some stars [7] to denying the role of dust in the variability based on the fact that the color indices of many antiflare stars decrease, rather than increase, during deep minima [8]. We derive here the optical properties of circumstellar dust based on magnitude—color index relations derived from long series of uniform observations.

2. OBSERVING MATERIAL AND APPROACH TO THE PROBLEM

Our observations were acquired in collaboration with T.U. Koval'chuck in 1975–1990 using the AZT-14 and Zeiss-600 telescopes of the Terskol High-altitude Observing Station in the Mt. Elborus region equipped with a semiautomatic electrophotometer operating in a photon-counting regime. Information about all procedural aspects of the observations and their reduction, such as our measurement program, the selection of standard stars, corrections for nonlinearity, corrections for atmospheric extinction, description of the photometric system, transformation of the measured magnitudes to the standard $UBVR$ system, etc., are discussed in our earlier paper [9].

We emphasize that we paid special attention to the transformation of the measured magnitudes to the standard $UBVR$ system. We convolved the transmission curves of colored filters forming the $UBVR$ system with the spectral sensitivity of the photoelectric multiplier in use, the transmission curve of the quartz field lens, and the refractory coefficient of the aluminum-coated mirror to obtain the reaction curves, S_i, of the instrumental photometric system. We then computed for stars of various spectral types and luminosity classes I and III the theoretical corrections δ_i due to the difference between the instrumental, S_i, and standard, S_{oi}, reaction curves of the $UBVR$ system:

$$\delta_i(\mathrm{Sp, L}) = -2.5 \log \frac{\int F_{\mathrm{sp}}(\lambda) S_{oi}(\lambda) d\lambda}{\int F_{\mathrm{sp}}(\lambda) S_i(\lambda) d\lambda},$$

where i denotes the photometric band and $F_{\mathrm{sp}}(\lambda) = F(\mathrm{Sp, L})$ are tabulated spectral energy distributions

1063-7729/04/4806-0470$26.00

for unreddened stars of various spectral types and luminosity classes.

The computed corrections, δ_i, were compared to the observed corrections using observations of standard stars in the cluster M44. These data were used to determine the true required corrections, δ_{ri}. Comparison of δ_i and δ_{ri} shows that they do not differ systematically over a wide range of effective temperatures corresponding to $V-R$ color indices in the range

$$0.15^m \leq V-R \leq 0.90^m.$$

Material illustrating the issues noted in this section is presented in [9]. The resulting corrections, δ_i, for a given spectral type Sp and luminosity class L can be applied to transform the measured instrumental magnitudes to standard magnitudes.

We consider here the optical properties of the dust in circumstellar envelopes based on an analysis of the relationship between variations of a star's brightness, V, and its color indices, $U-B$, $B-V$, and $V-R$. We determined the angular coefficients, b_i, of the $\Delta \mathrm{CI}_i = b_i \Delta V$ relations, where CI_i is one of the above color indices. This method is quite similar to that applied in studies of the physics of the interstellar matter to determine the ratio of the interstellar extinction to interstellar reddening, which is usually assumed in the case of interstellar material to be close to

$$R_{is} = \Delta V / \Delta(B-V) \approx 3.2.$$

It is obvious that our parameter, b, is simply $b = 1/R$.

One special aspect of this method as applied to antiflare stars is that, as a rule, the relationship between the brightness and the color indices is not linear: it is distorted by the presence of additional light produced by scattering of photospheric photons on the circumstellar-dust grains. This phenomenon, known as "zodiacal light," was first noted by Zaitseva [10] for UX Ori and subsequently explained by Grinin [11]. The color index–magnitude relation acquires the shape shown in Fig. 1 because the relative contribution of the additional scattered light becomes larger during the star's brightness minimum.

It is clearly impossible to determine b_i using this relation considered as a whole. There are two ways to overcome this difficulty.

(1) A limited range of ΔV values can be used near the maximum brightness, where the distortion from the additional light is the least. In this case, the $\Delta \mathrm{CI}_i = b_i \Delta V$ relation can be taken to be linear.

(2) Having approximated the observations with a smooth curve, we can plot a tangent passing through the normal-brightness point (Fig. 1); the angular coefficient of this tangent will be the desired b_i value.

The disadvantage of the first method is that the ΔV range must be as narrow as possible in order to maximally reduce the influence of the zodiacal light. However, in this case, the uncertainty in the position of the approximating line increases. In nearly all cases, we selected ΔV to be 0.5^m–0.6^m from the normal-brightness point. Figure 2 displays our linear approximation of the observations of BH Cep as an example. In all cases, we used a least-squares fit to obtain a linear or quadratic approximation.

The second method is more difficult to apply, since it is not possible for every star to obtain adequate series of observations covering the entire range of magnitudes, including the deep brightness minima. When this was possible, the observations were approximated with a second-order polynomial:

$$\mathrm{CI}_i = c + dV + eV^2.$$

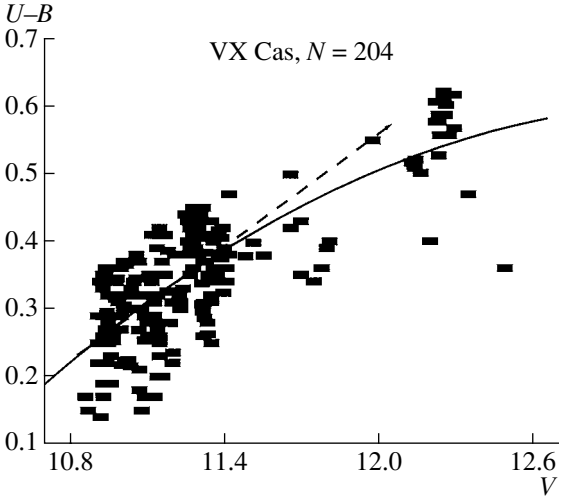

Fig. 1. $V-(B-V)$ relation for VX Cas with a parabolic fit; a tangent to the fit is plotted through the normal-brightness point.

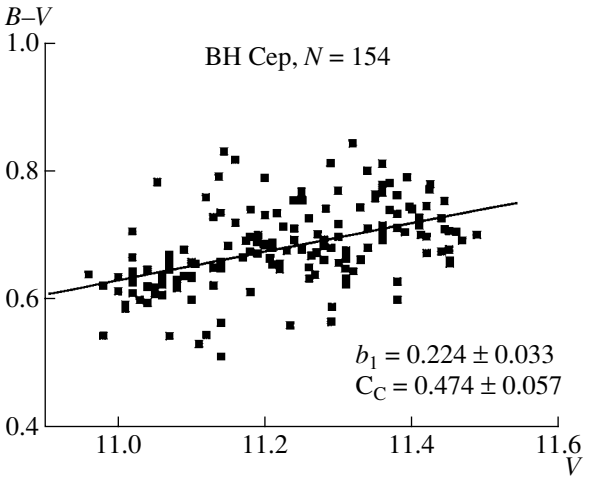

Fig. 2. Derivation of the b_{B-V} coefficient from the observations of BH Cep.

The tangent to this curve at the normal-brightness point,

$$(\mathrm{CI})' = d + 2eV_n,$$

was adopted as the straight line used in the first method to determine the coefficient b. It is obvious that $b = 2e$ in this case.

In all cases, we derived the autocorrelation coefficient, CC, which was subsequently used as a measure of the interconsistency of the observations and also as a weight in our statistical analysis.

3. RESULTS

The program stars and the results of our observations are presented in Table 1. In addition to the names of the stars and the number of observations analyzed, this table also contains the angular coefficients b_i for the $U{-}B$, $B{-}V$, and $V{-}R$ color indices, the correlation coefficients CC for the corresponding bands, and the magnitude range ΔV near the normal-brightness point used to determine b_i in the linear method.

The mean coefficients b_i for the entire sample of stars were obtained via direct averaging:

$$b_{U-B} = 0.3293; \quad b_{B-V} = 0.2453,$$
$$\text{and } b_{V-R} = 0.2004.$$

However, we consider the weighted mean coefficients to be more representative, since they reflect the number of individual measurements for each star, N, as well as their trustworthiness. The weights for each star were taken to be

$$W_i = NCC_i.$$

Applying these weights, W_i, we calculated the weighted mean coefficients b_i for each of the color indices:

$$b_{U-B} = 0.3434; \quad b_{B-V} = 0.2515,$$
$$\text{and } b_{V-R} = 0.2269.$$

These are the values we used in our subsequent calculations.

For several stars, we were also able to obtain b_i values using the second technique (the tangent method); these values are given in Table 2. Inspection of the data in Table 2 shows that the tangent method yielded values close to, but different from, those derived using the first method. There are at least two possible origins for these discrepancies. First, none of the stars were observed at all their brightness levels. The incomplete statistics of the observational data enhances the impact of random deviations on the approximating curves that were derived. This is why, for example, the b_{U-B} values (the second column of Table 2) are so different for different stars. Second, the magnitude–color index relation should probably be approximated by a more complex curve than a parabola. At any rate, the corresponding theoretical relations for R Coronae Borealis [12] are indeed expressed with more complex formulas. For this reason, the use of second-order curves is not fully adequate for the approximation of the observed relations, and we believe that it is better to describe the relationship between the color and brightness using the weighted mean values we obtained.

Using the relation between an absorber's optical depth, τ, and the extinction in magnitudes it creates, Δm,

$$\Delta m_i = 1.086\tau_i$$

and the set of equations

$$\Delta(U{-}B)/\Delta V = 0.3434;$$
$$\Delta(B{-}V)/\Delta V = 0.2515$$
$$\text{and } \Delta(V{-}R)/\Delta V = 0.2269,$$

we derived the relative dust optical depths in each band of the $UBVR$ system, which, normalized by τ_v, are

$$\tau_U = 1.5949; \quad \tau_B = 1.2515;$$
$$\tau_V = 1, \text{ and } \tau_R = 0.7731.$$

The corresponding values are shown in Fig. 3. Approximation of the results with a power law gives the wavelength dependence for the dust extinction coefficient in the optical

$$\theta(\lambda) = \lambda^{-1.1}.$$

4. DISCUSSION

The observational relation we have derived is very close to the generally accepted interstellar-extinction law, $\theta_{is}(\lambda) = \lambda^{-1}$. θ_{is} and θ coincide virtually perfectly in the B, V, and R bands and differ only slightly in the U band. Our estimates indicate that the UV extinction coefficient of the circumstellar dust is 5.6% higher than the extinction coefficient for interstellar matter. The reasons behind the good agreement between θ_{is} and θ are far from obvious. In earlier studies of the extinction properties of circumstellar dust, they were either determined only approximately [13] or were presented for individual stars [14] and interpreted before there was an understanding of the role of the "zodiacal light." In addition, the determinations of these properties were sometimes based on unrealistic models [15], and in some cases the role of dust in forming the color excesses was completely ignored because the authors considered the blueing of the light during minimum brightness to be incompatible with the presence of dust [8]. Our current study is

Table 1. Main results of the observations

Object	Angular coefficient, b				Correlation coefficient, CC			
	N	$U-B$	$B-V$	$V-R$	$U-B$	$B-V$	$V-R$	ΔV
SU Aur	240	0.390 ± 0.024	0.173 ± 0.022	0.168 ± 0.022	0.720 ± 0.042	0.446 ± 0.039	0.490 ± 0.038	9.0–9.6
VX Cas	110	0.234 ± 0.017	0.222 ± 0.008	0.126 ± 0.026	0.732 ± 0.040	0.906 ± 0.018	0.722 ± 0.020	10.8–11.4
SV Cep*	226	0.208	−0.120	0.876	0.744	0.342	0.901	10.95–11.25
BH Cep	154	0.365 ± 0.045	0.224 ± 0.033	Not measured	0.559 ± 0.074	0.501 ± 0.055	Not measured	10.9–11.5
BO Cep	362	0.412 ± 0.025	0.274 ± 0.019	0.193 ± 0.048	0.686 ± 0.039	0.602 ± 0.029	0.329 ± 0.040	11.5–12.0
R CrB	107	**0.306** ± 0.017	**0.188** ± 0.011	**0.169** ± 0.010	0.860 ± 0.051	0.852 ± 0.032	0.863 ± 0.028	5.7–6.6
T Ori	26	0.463 ± 0.120	0.260 ± 0.065	0.329 ± 0.086	0.617 ± 0.136	0.630 ± 0.073	0.621 ± 0.097	9.7–10.6
BF Ori	24	0.328 ± 0.051	0.142 ± 0.051	0.063 ± 0.018	0.805 ± 0.063	0.505 ± 0.064	0.609 ± 0.022	9.9–10.6
BN Ori**	53	0.320 ± 0.031	0.305 ± 0.028	0.268 ± 0.020	0.804 ± 0.096	0.821 ± 0.085	0.871 ± 0.061	9.6–11.3
CO Ori	31	0.279 ± 0.107	0.258 ± 0.069	0.177 ± 0.039	0.438 ± 0.140	0.557 ± 0.108	0.618 ± 0.053	10.0–10.8
EZ Ori	40	0.180 ± 0.119	0.293 ± 0.017	0.254 ± 0.073	0.238 ± 0.106	0.479 ± 0.079	0.492 ± 0.065	11.2–12.0
HK Ori	58	0.323 ± 0.052	0.356 ± 0.051	0.232 ± 0.051	0.633 ± 0.082	0.678 ± 0.080	0.579 ± 0.083	11.4–12.2
IU Ori	444	0.239 ± 0.028	0.453 ± 0.020	0.477 ± 0.023	0.373 ± 0.072	0.730 ± 0.051	0.697 ± 0.059	8.9–9.5
V346 Ori	320	0.381 ± 0.031	0.368 ± 0.029	0.166 ± 0.023	0.558 ± 0.084	0.573 ± 0.078	0.366 ± 0.063	10.2–10.8
V350 Ori	55	0.272 ± 0.073	0.231 ± 0.060	0.267 ± 0.058	0.453 ± 0.117	0.462 ± 0.097	0.530 ± 0.093	10.7–11.4
V351 Ori	352	0.329 ± 0.029	0.232 ± 0.014	0.110 ± 0.011	0.508 ± 0.085	0.647 ± 0.042	0.459 ± 0.033	8.8–9.5
V361 Ori*	32	−0.114	−0.267	0.311	−0.219	−0.491	0.486	7.93–8.22
V380 Ori	42	0.498 ± 0.071	0.221 ± 0.078	0.161 ± 0.040	0.739 ± 0.062	0.394 ± 0.070	0.522 ± 0.035	10.0–10.6
V451 Ori***	61	0.452 ± 0.011	0.314 ± 0.007	0.203 ± 0.006	0.981 ± 0.080	0.985 ± 0.048	0.974 ± 0.042	9.4–12.0
V586 Ori	381	0.473 ± 0.030	0.193 ± 0.026	0.319 ± 0.036	0.628 ± 0.082	0.338 ± 0.097	0.399 ± 0.099	9.3–9.9
XY Per	110	0.283 ± 0.031	0.242 ± 0.020	0.224 ± 0.016	0.650 ± 0.043	0.755 ± 0.027	0.793 ± 0.022	9.0–9.8
IP Per	103	0.274 ± 0.082	0.149 ± 0.045	–	0.542 ± 0.033	0.308 ± 0.023	–	10.3–10.6
RZ Psc	479	0.173 ± 0.020	0.114 ± 0.016	0.276 ± 0.043	0.365 ± 0.067	0.306 ± 0.046	0.459 ± 0.050	
WW Vul	97	0.184 ± 0.044	0.261 ± 0.036	0.233 ± 0.030	0.396 ± 0.049	0.592 ± 0.041	0.624 ± 0.033	10.3–10.8

* The primary variability process was absent. The obtained coefficients were excluded from the analysis because they describe different, secondary variability processes.

** Only five brightness measurements were obtained in the faint state.

*** The reason the ΔV interval is so large is that the star's brightness is restricted to two extreme states: 9.4 and 12.0.

essentially the first to investigate the optical properties of circumstellar dust on the basis of extensive and uniform observational material using a realistic model for the brightness variability of antiflare stars. Note that we have not made use of the numerous observations obtained by other authors. This restriction was intended precisely to preserve the "color" uniformity of our data, since there are known to be small discrepancies between the color systems used by different observers. Such discrepancies are not always obvious during a qualitative comparison of results, but they can distort the final results of accurate quantitative analyses such as that considered here. We were not able to accurately transform the color systems of other

Table 2. b_i values derived as the angular coefficient of the tangent line

Star	b_{U-B}	b_{B-V}	b_{V-R}	N	V_N
RZ Psc	0.296	0.139	0.233	694	11.75
VX Cas	0.213	0.271	0.275	214	11.16
WW Vul	0.242	0.216	0.226	105	10.48
V346 Ori	0.438	0.324	0.172	478	10.5
V586 Ori	0.601	0.333	0.361	395	9.63
V351 Ori	0.424	0.330	0.226	421	8.95
Mean	0.369 ± 0.060	0.269 ± 0.032	0.249 ± 0.026		

observers to our own system, and so we decided to restrict our analysis to our own observations.

Having performed a complete and statistically rigorous analysis of the data, we can now revise our earlier conclusion that extinction by circumstellar dust differs from interstellar extinction [13]. Nevertheless, our earlier conclusion that the extinction coefficient of circumstellar dust is higher than that of interstellar dust in the ultraviolet remains valid. Although the excess is only about 5.6%, we believe it to be real. This difference may be related to the assumption that the dust in the vicninty of an antiflare star appears as a result of an eruption, as is true of R CrB stars [4]. In this case, the young, fresh dust associated with antiflare stars may differ from the older interstellar dust. In addition, we should discuss the fact that the coefficients b_i for R CrB,

$$b_{U-B} = (0.306 \pm 0.017),$$
$$b_{B-V} = (0.188 \pm 0.011),$$

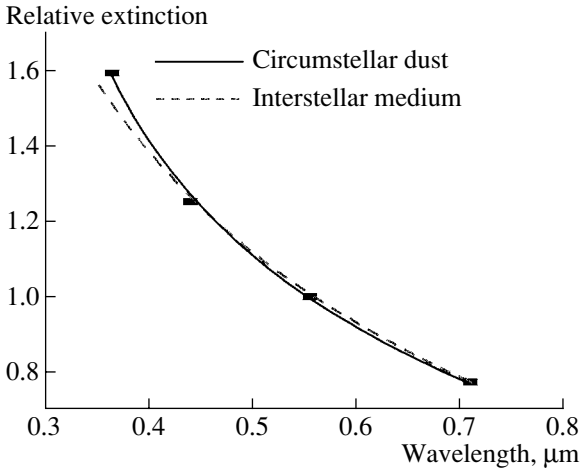

Fig. 3. Comparison of the derived $\theta(\lambda)$ relation and the interstellar extinction law.

and $b_{V-R} = (0.169 \pm 0.010)$,

differ significantly from the weighted mean coefficients for the antiflare stars. Here, the role of differences in the elemental abundances of the stellar atmospheres is probably key: the dust around R CrB contains a large amount of graphite, whereas there is no excess of this element in the dust surrounding the antiflare stars.

Note that the individual b_i values in Table 1 sometimes show considerable deviations from the mean. While it is possible that these deviations could be due to uncertainties in the approximating relations (due to insufficient numbers of observations at all brightness levels), they could also reflect individual differences in the chemical composition of the circumstellar material. For example, the values of b_{B-V} are significantly different for IU Ori and V351 Ori, in spite of the fact that many observations with fairly high correlation coefficients are available for both of these stars.

5. CONCLUSION

The refined dust extinction coefficient enables a reevaluation of earlier conclusions that the optical properties of circumstellar and interstellar dust are different. These differences are small and, if present, are pronounced only in the ultraviolet. This result agrees with the concept that the Galaxy's dusty material is "universal" in some sense. Although the recent results of IR spectroscopy provide evidence that the chemical and morphological compositions of dust differ for different stars, these differences are not large in the optical range. Moreover, it turns out that the crystalline–silicate dust of comets has similar optical properties to the dust surrounding young stars [16]. If confirmed, this similarity could prove to be important for our understanding of the origin of interstellar and circumstellar dust.

REFERENCES

1. V. P. Grinin, P. S. The, G. de Winter, *et al.*, Astron. Astrophys. **292**, 165 (1994).
2. V. P. Grinin, N. N. Kiselev, N. Kh. Minikulov, and G. P. Chernova, Pis'ma Astron. Zh. **14**, 514 (1988) [Sov. Astron. Lett. **14**, 219 (1988)].
3. A. F. Pugach, Kinemat. Fiz. Neb. Tel **17**, 291 (2001).
4. G. C. Clayton, Publ. Astron. Soc. Pac. **108**, 225 (1996).
5. N. V. Voshchinnikov and V. P. Grinin, Astrofizika **34**, 181 (1999).
6. M. L. Sitko, S. A. Grady, D. K. Lynch, *et al.*, Astrophys. J. **510**, 408 (1999).
7. R. D. Schwartz, Astrophys. J. **191**, 419 (1974).
8. W. Herbst, J. A. Holzmann, and R. S. Klasky, Astron. J. **88**, 1648 (1983).
9. A. F. Pugach and G. U. Koval'chuk, Perem. Zvezdy **22**, 9 (1983).
10. G. V. Zaĭtseva, Perem. Zvezdy **19**, 63 (1973).
11. V. P. Grinin, Pis'ma Astron. Zh. **14**, 65 (1988) [Sov. Astron. Lett. **14**, 27 (1988)].
12. A. F. Pugach, Astron. Zh. **68**, 122 (1991) [Sov. Astron. **35**, 61 (1991)].
13. G. U. Koval'chuk and A. F. Pugach, Kinemat. Fiz. Neb. Tel **7**, 33 (1991).
14. G. V. Zaĭtseva and P. F. Chugaĭnov, Astrofizika **20**, 447 (1984).
15. M. R. Perez, J. R. Webb, and P. S. The, Astron. Astrophys. **257**, 209 (1992).
16. C. Waelkens, K. Malfait, and L. B. F. M. Waters, Earth, Moon, Planets **79**, 265 (1997).

Translated by N. Samus'

Astronomy Reports, Vol. 48, No. 6, 2004, pp. 476–491. Translated from Astronomicheskiĭ Zhurnal, Vol. 81, No. 6, 2004, pp. 523–540.

CaII Line Formation in the Spectra of Irradiated Atmospheres

D. V. Ivanova, N. A. Sakhibullin, and V. V. Shimanskiĭ

Kazan State University, ul. Lenina 18, Kazan, 420008 Tatarstan, Russia

Received March 15, 2002; in final form, November 10, 2003

Abstract—We have studied the effect of external radiation on the formation of LTE and non-LTE CaII lines in the spectra of A–M-star atmospheres. Three frequency distributions were chosen for the external radiation: X-ray radiation specified by the power law $I_\nu^+ = I_0\nu^{-0.6}$ at 1–16.5 keV and UV radiation specified by blackbody distributions with the temperatures $T_{rad} = 50\,000$ and 15 000 K. We analyze the influence of variations in the irradiating flux and its angle of incidence on the profiles and equivalent widths of the $\lambda\lambda$3933, 3968 Å resonance doublet and the $\lambda\lambda$8498, 8542, 8662 Å infrared triplet. For any type of external radiation, allowing for deviations from LTE decreases the reflection effects for the CaII lines. We conclude that the CaII profiles do not display emission components in the spectra of optically thick stellar atmospheres irradiated by X-rays. Therefore, CaII emission lines observed in the radiation of cataclysmic variables must be formed in an optically thin plasma. CaII emission lines are likely to form in the spectra of stars with UV irradiation if CaII is the dominant ionization state in atmospheric layers close to the depths at which the continuum is formed. As a result, the spectra of symbiotic variables with hot primaries can contain CaII lines originating on the surfaces of the M-giants and supergiant secondaries due to reflection effects. These lines can be used to analyze the reflection effects and the temperature structure in the atmospheres of the secondaries only if non-LTE effects are included. In the spectra of close binaries with cool white dwarfs, CaII emission lines originate in the irradiated atmospheres of the secondaries under conditions close to thermalization. These lines can be used to study the reflection effects and calcium abundances even in an LTE approximation. We calculated the profiles and equivalent widths of CaII lines in the spectra of the four precataclysmic variables BE UMa, EG UMa, MS Peg, and HR Cam. The observed and theoretical reflection effects in the $\lambda\lambda$3933, 8542 Å emission lines for the specified parameters of the systems and a solar calcium abundance in the atmospheres of the red dwarfs are in good agreement.

1. INTRODUCTION

Reflection effects are characteristic of the radiation of close binary systems. These effects give rise to nearly sinusoidal periodic brightness variations and numerous emission lines in the spectra of some types of close binaries. Reflection effects occur when hard (UV or X-ray) radiation from one of the components is absorbed at the surface of the other component and then reemitted at optical wavelengths. Studies of reflection effects carried out in the 1970s and 1980s initially focused on physical analyses of the processes involved. However, in the early 1990s, it became realistic to use reflection effects to study the close binary systems themselves. The WD [1] and LIGHT2 [2, 3] codes were developed to calculate the light curves of binaries taking into account reflection effects in a blackbody approximation. These codes have proven to be most effective when applied to detached or eclipsing close binaries for which complete sets of parameters have been determined [4–8].

At the same time, the development of quantitative studies of binary-system light curves has been accompanied by substantial difficulties. Numerous models for the eclipsing variable HW Vir [9–11] showed that the brightness variations could be adequately reproduced only if the albedo of the secondary was larger than unity and the limb darkening was negative. It was concluded in [6] that taking into account reflection effects requires that the temperature structure of the atmospheres of the irradiated stars be modeled quantitatively. Theoretical fitting of the emission-line profiles observed in the spectra of close binaries, primarily those of the Balmer lines and lines of HeI and CaII, can serve as a criterion for such modeling.

The available observational data suggest that CaII lines can be used to analyze the temperature structures of irradiated atmospheres only for some types of close binary. In some spectra of semidetached binaries with accretion and X-ray irradiation, emission lines of ionized calcium are either not observed (HZ Her, UX UMa, TT Ari) [12–14] or are observed only in "low" states (RE And, S Aur, IK Nor etc.) [12, 15]. These spectra display numerous emission lines of hydrogen, He, and heavy elements, along with a low radiation flux in the continuum.

1063-7729/04/4806-0476$26.00

In precataclysmic and symbiotic systems in which reflection effects occur when one of the components is irradiated by UV radiation, the intensity of the CaII emission lines depends on the temperature and luminosity of the hot component. In the spectra of systems containing blue subdwarfs or extremely hot white dwarfs (BE UMa, UU Sge, V664 Cas), the CaII λ3933 Å line is very weak or absent. In a model for one such system, NN Ser [16], the theoretical and observed spectra were in good agreement for both the continuum and Balmer profiles, while the observed CaII λ3933 Å emission line was appreciably weaker than the theoretical line. This suggests the presence of substantial deviations from local thermodynamic equilibrium (LTE) in this line in systems with hard UV irradiation.

Close binaries in which the white dwarf has a moderate temperature (EG UMa, IN CMa, V471 Tau) display strong CaII $\lambda\lambda$3933, 3968 Å emission lines, whose intensity is comparable to the intensities of the Balmer lines. The CaII $\lambda\lambda$8498, 8542, 8662 Å IR triplet is observed in the spectra of HR Cam and MS Peg and has been used to estimate the reflection effects in these systems [17, 18]. Since the ionized calcium in the atmospheres of the cool components of all these systems is in the ground ionization state, the calcium lines are likely to display minimum deviations from LTE, so that they can be used to analyze the temperature structure of the irradiated stellar atmospheres. Here, we study prospects for such analyses for various types of close binaries.

Our technique for modeling atmospheres with external irradiation and non-LTE effects in CaII is described in detail in [19]. Here, we will consider the formation of non-LTE level populations and CaII line profiles in stellar atmospheres with irradiation spectra characteristic of various external sources. Sections 2.1–2.3 present our results for X-ray, hard UV, and soft UV irradiation, respectively. Section 3 contains our results of modeling the CaII lines in the spectra of some close binaries.

2. NON-LTE DEVIATIONS IN CaII LINES IN IRRADIATED STELLAR ATMOSPHERES

We consider here the influence of external radiation on the formation of LTE and non-LTE CaII lines in the spectra of stellar atmospheres with $T_{eff} = 4000$, 6000, 10 000 K and $\log g = 4.0$. Results will be presented for three frequency dependences of the external radiation: X rays specified by the power law $I_\nu^+ = I_0\nu^{-0.6}$ in the interval 1–16.5 keV and UV radiation specified by blackbody distributions with temperatures $T_{rad} = 50\,000$ and 15 000 K.

Our calculations indicate that CaII ions can contribute substantially (exceeding 3%) to the total absorption only at wavelengths $\lambda > 912$ Å. Therefore, in the case of hard UV ($T_{rad} = 50\,000$ K) or X-ray irradiation, the external radiation essentially does not interact with the CaII ions, and their distribution of states is determined by the structure of the atmosphere and its radiation field. The temperature structures of the irradiated atmospheres are very different for the three cases considered, which leads to different conditions for the formation of non-LTE deviations in the CaII lines. In the case of soft UV irradiation ($T_{rad} = 15\,000$ K), the external radiation can directly ionize CaII ions and affect their distribution of states, together with the intrinsic radiation of the atmosphere.

The incident radiation is specified by the cosine of the angle of incidence, μ, and the intensity of the external radiation flux. In practice, in the case of an atmosphere with a specified effective temperature T_{eff}, it is convenient to specify the intensity of the external radiation using the irradiation parameter K_x, which is the ratio of the incident flux, H_x, and the total radiative flux of the unirradiated atmosphere, H_0:

$$K_x = \frac{H_x}{H_0}, \tag{1}$$

where

$$H_0 = \sigma T_{eff}^4 \tag{2}$$

and

$$H_x = \mu I_x^+(\tau_r = 0.0). \tag{3}$$

All the presented model atmospheres, level populations, and CaII line profiles were calculated using the methods described in [19] and solar elemental abundances, based on the data of Anders and Grevesse [20]. The model-atmosphere grid of Kurucz [21] was used to obtain models for the non-irradiated atmospheres.

2.1. X-ray Irradiation

In order to obtain a better understanding of non-LTE effects occurring in CaII in irradiated atmospheres, we must first consider these effects in the atmospheres of ordinary stars. It is convenient to analyze deviations from LTE in level populations using their b factors—the ratios of the non-LTE and LTE populations:

$$b_i = \frac{n_i(\text{non-LTE})}{n_i(\text{LTE})}. \tag{4}$$

Figure 1a presents the distribution of the b factors for some levels of the CaII ion over the Rosseland opacity

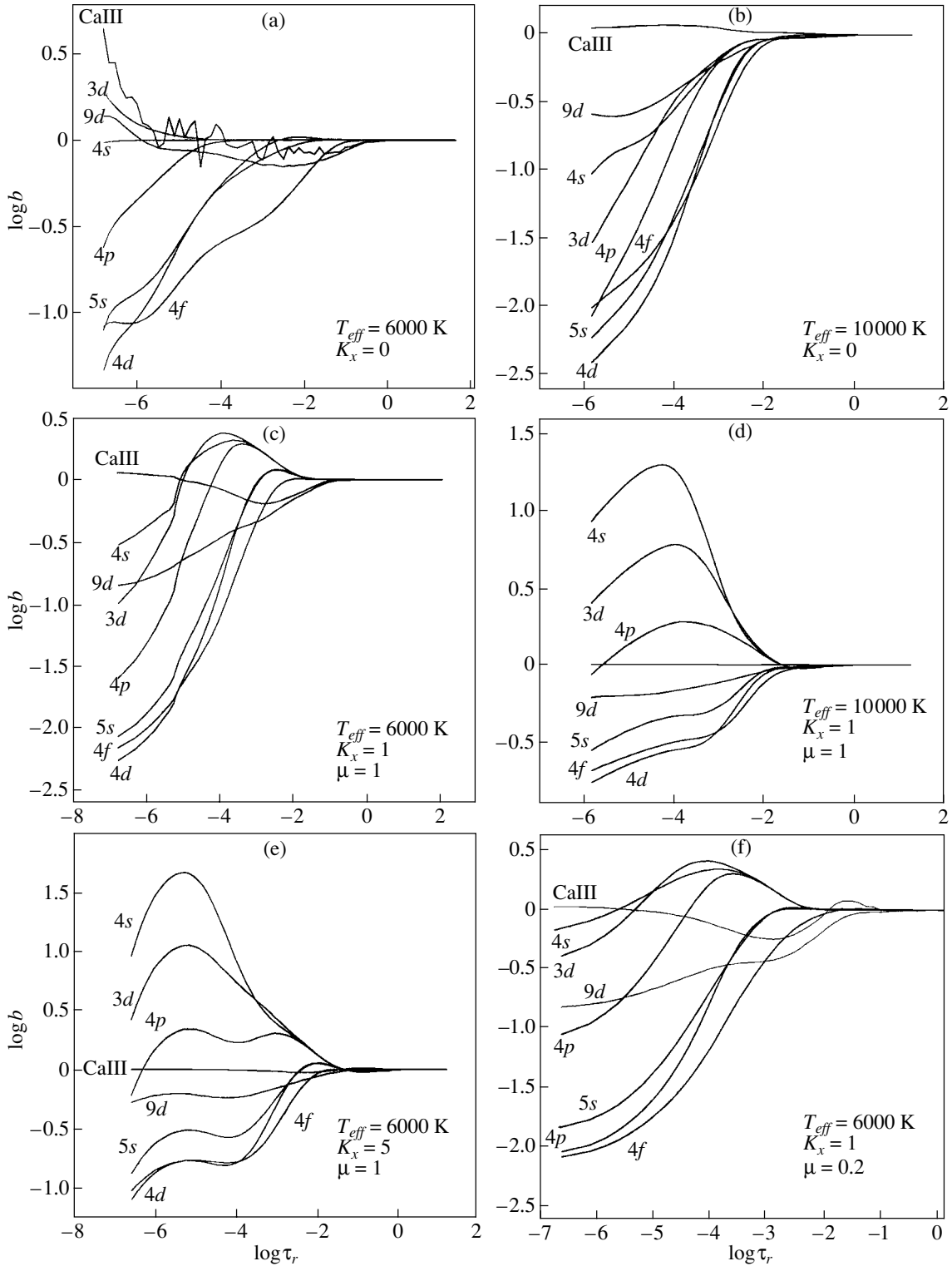

Fig. 1. Distribution of b factors of the main CaII levels over the Rosseland opacity τ_r in the atmospheres of stars (a, b) without and (c–f) with external X-ray radiation of various intensities.

τ_r for a model atmosphere with $T_{eff} = 6000$ K and $\log g = 4.0$ without external radiation.

In the absence of external irradiation, CaII is the main ionization state of calcium. As a result, most atoms (more than 97%) are in the $4s$ state, and this b factor is equal to unity. Deviations from the LTE

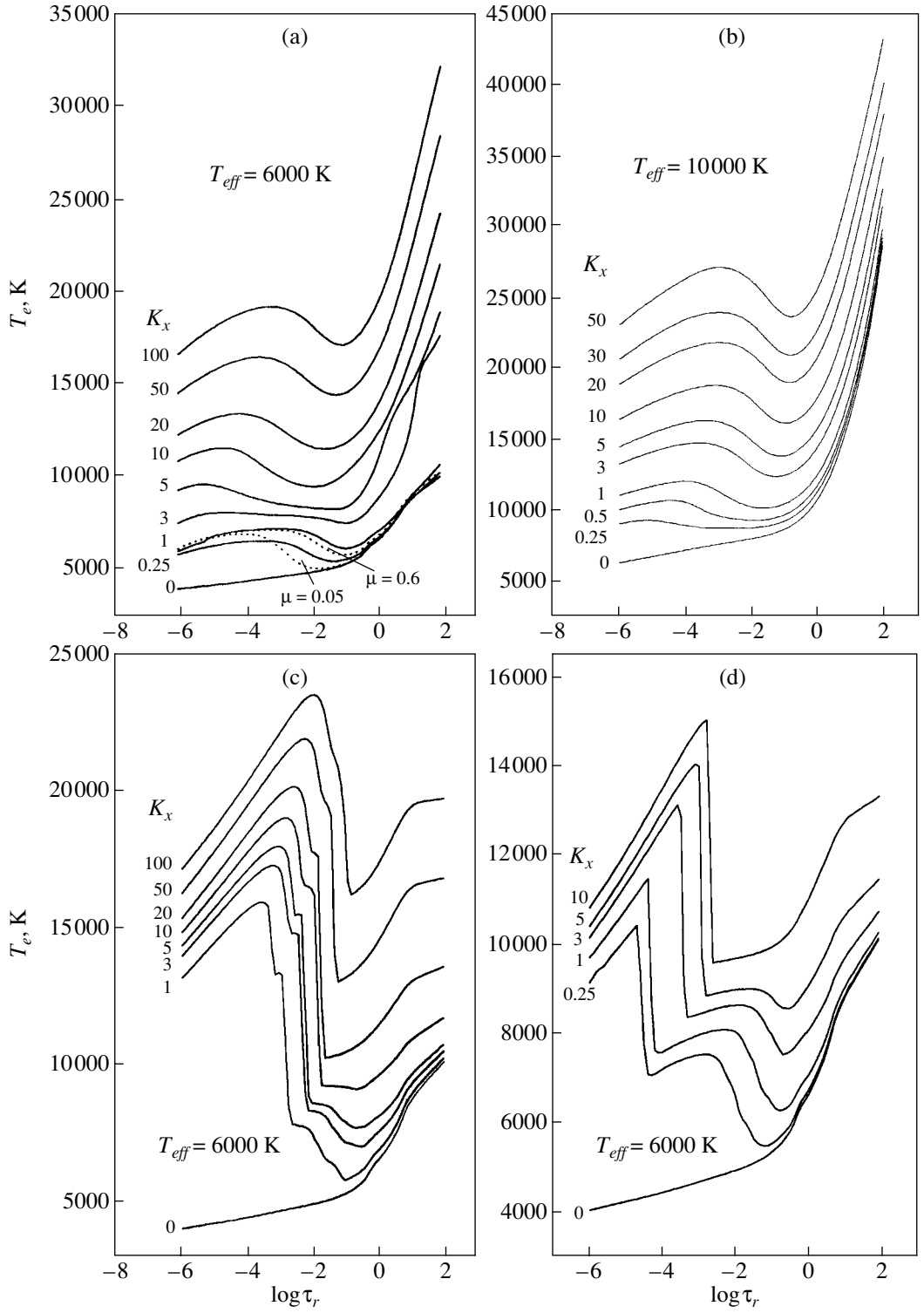

Fig. 2. Distribution of the electron temperature over the Rosseland opacity τ_r in atmospheres with (a, b) X-ray, (c) hard, and (d) soft UV irradiation. The solid lines indicate distributions with various intensities of the radiation for $\mu = 1.0$, while the dotted lines show the distributions for $K_x = 1.0$ and various angles of incidence.

populations of the other levels begin to occur at opacities $\log \tau_r < -1.5$ and are determined by the balance of bound–bound transitions for the weakly excited $4p$ and $3d$ levels and the effect of ionization and recombination on all highly excited levels and the CaIII continuum. We will consider these processes separately.

The saturation of the $4p$ level occurs via the radiative excitation of ions from the ground state in the wings of the $\lambda\lambda$3933, 3968 Å resonance doublet. The mechanism for and origin of radiative excitation in the wings of resonance UV lines have been studied in detail in [22] using the magnesium atom as an example. The balance between excitation and deexcitation in the wings can be disrupted even in deep layers of the atmosphere, where the optical depth in the line core is much higher than unity. However, the radiative excitation does not result in overpopulation of the $4p$ level, since spontaneous $4p$–$3d$ transitions become more efficient in high layers of the atmosphere. As a result, the $3d$ level is overpopulated ($\log b = 0.06$–0.10), while the $4p$ level is underpopulated ($\log b = -0.12$ to 0.20).

Let us consider the formation of the populations of highly excited CaII levels and the CaIII ionization state. At any frequency, the number of atoms ionized at that frequency is proportional to the mean intensity J_ν, while the number of recombining atoms is proportional to the source function S_ν. Recombination dominates if $J_\nu < S_\nu$, while ionization dominates if $S_\nu < J_\nu$. In a nonirradiated atmosphere, the temperature gradient $dT_e/d\tau_r$ is strictly positive (Fig. 2a), and the source function increases with depth at all frequencies. Therefore, there exists for each depth a frequency such that $J_\nu < S_\nu$ at lower frequencies and $J_\nu > S_\nu$ at higher frequencies. As a result, the balance between ionization and recombination for a specific level depends on the region in which most of the absorbing atoms are located.

Our calculations indicate that, in nonirradiated atmospheres, ionization dominates for all the main CaII levels. Note that ionization from the $4p$ and $3d$ levels occurs only in the region with $\log\tau_r < -4.15$, and ionization from the $4s$ level is negligible, since the ionization limits lie in the far UV, which is blanketed by lines of heavy elements. Ionization from upper levels is efficient only in high layers of the atmosphere ($\log\tau_r < -5.0$), and ionization from the $5s$, $5p$, and $4d$ levels, in layers with $\log\tau_r < -0.55$. Photoionization leads to the overpopulation of the CaIII ground state ($\log b = 0.05$) and highly excited CaII levels ($E_{ex} >$ 10.5 eV), which are strongly connected to the continuum via the collision rates. For levels with excitation energies $6.5 < E_{ex} < 10.5$ eV, ionization decreases the b factors (to $\log b = -0.6$ to -0.9 for the $5s$ and $4d$ levels). We thus conclude that the CaII ions in the atmospheres of cool stars with temperatures $T_{eff} =$ 6000 K are in a state of "overionization"; i.e., the following ionization state, CaIII, is overpopulated.

The presence of even low-intensity hard external radiation leads to dramatic changes in the distributions of the b factors. Figure 1c illustrates these changes for a model atmosphere with $K_x = 1.0$ and $\mu = 1.0$, while Fig. 2a presents the corresponding temperature distribution.

In atmospheres with external X-ray radiation, a chromospheric region forms in layers with $\log\tau_r <$ -2.0 to -1.5, whose temperatures are 10–15% higher than at the depth where the continuum forms. Therefore, in the chromosphere of such an irradiated atmosphere, $J_\nu < S_\nu$ in all spectral intervals for which the continuum forms near the temperature minimum. For an atmosphere with $K_x = 1.0$, such intervals correspond to wavelengths $\lambda > 1800$ Å; at shorter wavelengths, blanketing effects shift the depth of formation of the emergent radiation to high-temperature layers with $\log\tau_r < -3.0$ to -2.0. As a result, recombination becomes dominant in all excited levels starting from the $5s$ level. The situation is more complex for the $4p$ and $3d$ levels: ionization remains dominant only in cool layers above $\log\tau_r =$ -5.4 and below $\log\tau_r = -2.0$.

At the same time, the external irradiation results in a rapid increase of the influence of another mechanism for redistributing the atomic level populations—spontaneous transitions from upper to lower levels. According to the detailed analysis of [22–24], in nonirradiated stellar atmospheres, these transitions occur because $J_\nu < S_\nu$ in the cores of all saturated and nearly saturated lines. However, the increase in the efficiency of spontaneous transitions in irradiated atmospheres is due to the increase of the source function in the hot chromosphere, which strengthens the inequality $J_\nu \ll S_\nu$.

The non-LTE deviations in the level populations are due to the combined action of mechanisms that redistribute the atomic states when the ground ionization state makes the transition from CaII to CaIII. The ground CaIII state is close to LTE and saturates highly excited CaII levels via photorecombination. Further, there is a flow of atoms to less excited levels, right down to the $4p$ and $3d$ states, via spontaneous transitions along the chain ng, nf–$5s, 4d$–$4p$–$3d$. The $4p$ and $3d$ levels become overpopulated to $\log b =$ 0.2 and $\log b = 0.3$, respectively, while highly excited levels become underpopulated. For small amounts of irradiation, strong lines of the $\lambda\lambda$3933, 3968 Å resonance doublet remain under the detailed balance conditions, which inhibits the increase of non-LTE deviations for the $4s$ ($\log b = 0.2$) level. Overall, however, the external radiation results in the transition of CaII to a "super-recombination" state, for which the non-LTE populations of the ground $4s$ state and all low-excitation levels exceed the estimates obtained for LTE.

As the intensity of the incident radiation increases, the chromosphere tends to become heated and shifts toward deeper layers (Fig. 2a). However, the patterns

of the distributions of the b factors in all CaII levels do not vary qualitatively.

When the intensity of the external irradiation increases to $K_x = 5.0$, $J_\nu < S_\nu$ at wavelengths $\lambda > 912$ Å, which results in the recombination of atoms from the CaIII state to all CaII levels. As a result, the b factors of the $4s$, $4p$, and $3d$ levels keep increasing, and the $4s$ ground state becomes the most overpopulated. The increase of non-LTE deviations in the $4s$ populations are due to the increase in the efficiency of spontaneous transitions in the lines of the resonance doublet, which are weakened and deviate from the detailed balance conditions in atmospheres with strong irradiation.

With further increase of the intensity of the external radiation ($K_x > 5.0$), non-LTE deviations in the level populations begin to decrease. This can be explained in two ways:

(1) When the temperature increases, CaII ions undergo a rapid transition to the next ionization state (CaIII), which weakens all lines and decreases the role of spontaneous transitions relative to stimulated radiation and absorption; i.e., the condition $J_\nu < S_\nu$ is weakened.

(2) The temperatures at the depth of formation of the continuum and in chromosphere layers (Fig. 2a) become closer; as a result, the domination of recombination relative to ionization lessens.

We studied the influence on the formation of the non-LTE populations of varying the angle of incidence of the external radiation. We can see in Fig. 2a that decreasing μ from 1.0 to 0.05 results in intense absorption of the external radiation in high layers of the atmosphere, as a consequence of which the temperature gradient in these layers increases, together with the difference between the temperatures in the chromosphere and at the depth $\log \tau_r = 0$. These effects enhance recombination in chromospheric layers and decrease recombination in the region of the temperature minimum; i.e., the non-LTE deviations are shifted toward higher atmospheric layers and their amplitude is increased (Fig. 1f). Similar variations in the non-LTE deviations in the populations of the CaII levels due to variations of the angle of incidence are observed for various frequency characteristics of the external radiation in the atmospheres of various types of stars; we will not discuss these further here.

In a nonirradiated atmosphere with $T_{eff} = 10\,000$ K (Fig. 2b), CaIII is the dominant ionization state; its ground-state population is close to LTE. The high effective temperature of the star facilitates the growth of the intensity of the radiation at wavelengths 912 Å $< \lambda <$ 1600 Å, which actively ionizes CaII ions from the $4s$, $3d$, and $4p$ levels in layers with $\log \tau < 0.0$. Simultaneously, all the subordinate CaII lines are weakened and the efficiency of the corresponding spontaneous transitions decreases. As a result, CaII ions become "superionized" in an atmosphere with $T_{eff} = 10\,000$ K; i.e., all levels are underpopulated compared to LTE conditions (Fig. 1b).

The heating of an atmosphere with $T_{eff} = 10\,000$ K by external radiation does not differ qualitatively from the case of a lower-temperature atmosphere (Fig. 1d). Under these conditions, the main mechanisms for the redistribution of the atomic levels in irradiated atmospheres with various T_{eff} values are essentially the same. However, in atmospheres with $T_{eff} > 8000$ K, the efficiency of spontaneous transitions decreases rapidly as the intensity of the external radiation increases due to the transition of the lines to the linear section of the curve of growth. Therefore, the overpopulation of the lower levels is systematically lower for $T_{eff} = 10\,000$ K than for $T_{eff} = 6000$ K (Figs. 1c, 1d) and reaches its maximum at $K_x = 1.0$ (and at $K_x = 5.0$ for $T_{eff} = 6000$ K).

Thus, the character of non-LTE deviations in irradiated atmospheres in stars with effective temperatures $T_{eff} = 5000{-}13\,000$ K remains the same.

Non-LTE deviations in the profiles and equivalent widths of the CaII lines are determined by variations in the depth of their formation and the effect of the level populations on the source function, in accordance with the formula

$$S_\nu = \frac{2h\nu^3}{c^2}\frac{1}{\dfrac{n_i g_j}{n_j g_i} - 1} = \frac{2h\nu^3}{c^2}\frac{1}{\dfrac{b_i}{b_j}e^{\frac{h\nu}{kT}} - 1} \approx \frac{b_j}{b_i}B_\nu(T), \quad (5)$$

where b_i and b_j are the b factors for the lower and upper levels of the transition, respectively.

For a nonirradiated atmosphere with $T_{eff} = 6000$ K, the LTE and non-LTE profiles of the $\lambda\lambda$3933, 3968 Å resonant lines coincide because the b factors of the $4s$ and $4p$ levels are close to unity (Fig. 1a). The b factors of the $3d$ and $4p$ levels differ substantially (Fig. 1a; $\log b_i - \log b_j = 0.25$ in $\log \tau_r < -4.5$), and the cores of the $\lambda\lambda$8498, 8542, 8662 Å IR-triplet lines are enhanced compared with the LTE case (Fig. 3b).

In the chromospheric layers of atmospheres with irradiation of various intensities, the source function exceeds that at the depth of formation of the continuum by a factor of three to five at all frequencies. Since the cores of strong CaII lines in irradiated atmospheres with $T_{eff} = 6000$ K are formed in the chromosphere, they go into emission under LTE

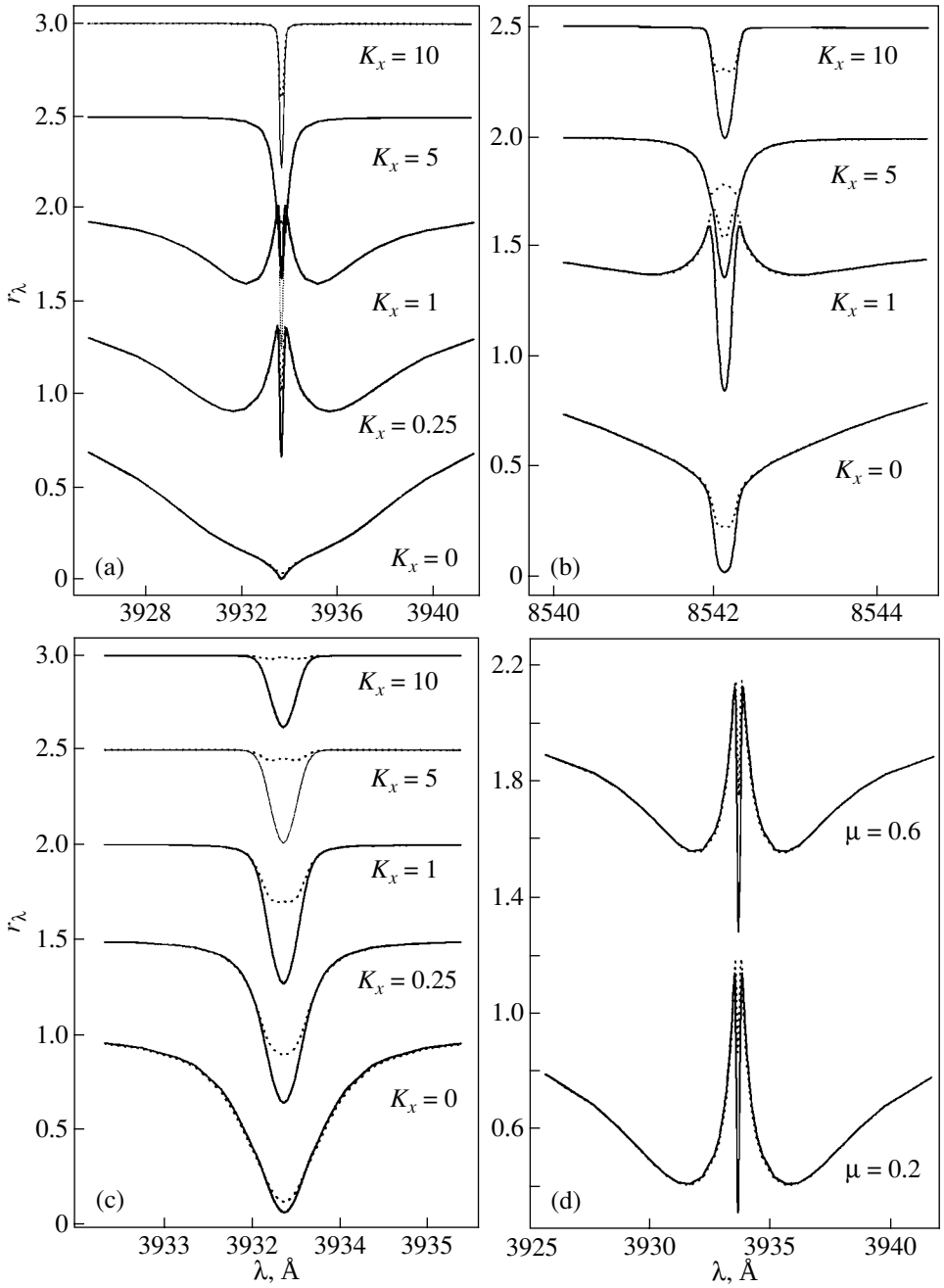

Fig. 3. Non-LTE (solid curves) and LTE (dotted curves) profiles of the (a, c, d) λ3933 Å and (b) λ8542 Å lines for stellar atmospheres with (a, b, d) $T_{eff} = 6000$ K and (c) $T_{eff} = 10\,000$ K with external X-ray radiation with various intensities for (a–c) angle of incidence $\mu = 1.0$ and (d) $K_x = 1.0$. The profiles have been given sequential shifts along the vertical axis by (a–c) 0.5 and (d) 1.0.

conditions (Figs. 3a, 3b). For irradiation with $K_x = 1.0$, the difference between the b factors of the lower and upper levels of the $4s$–$4p$ and $3d$–$4p$ transitions does not exceed 40%, and they cannot substantially decrease the source function. As a result, emission cores are also formed in the non-LTE profiles of CaII lines, although they are weaker than in the LTE case. When the external irradiation is increased to $K_x = 5.0$, the $4s$ and $3d$ levels become a factor of three more overpopulated than the $4p$ level, which makes the source function in the chromosphere smaller than at the depth of formation of the continuum. Therefore, the non-LTE profiles of the CaII resonance doublet and the IR triplet are observed in absorption for all $K_x > 5.0$ (Figs. 3a, 3b). Thus, taking into account

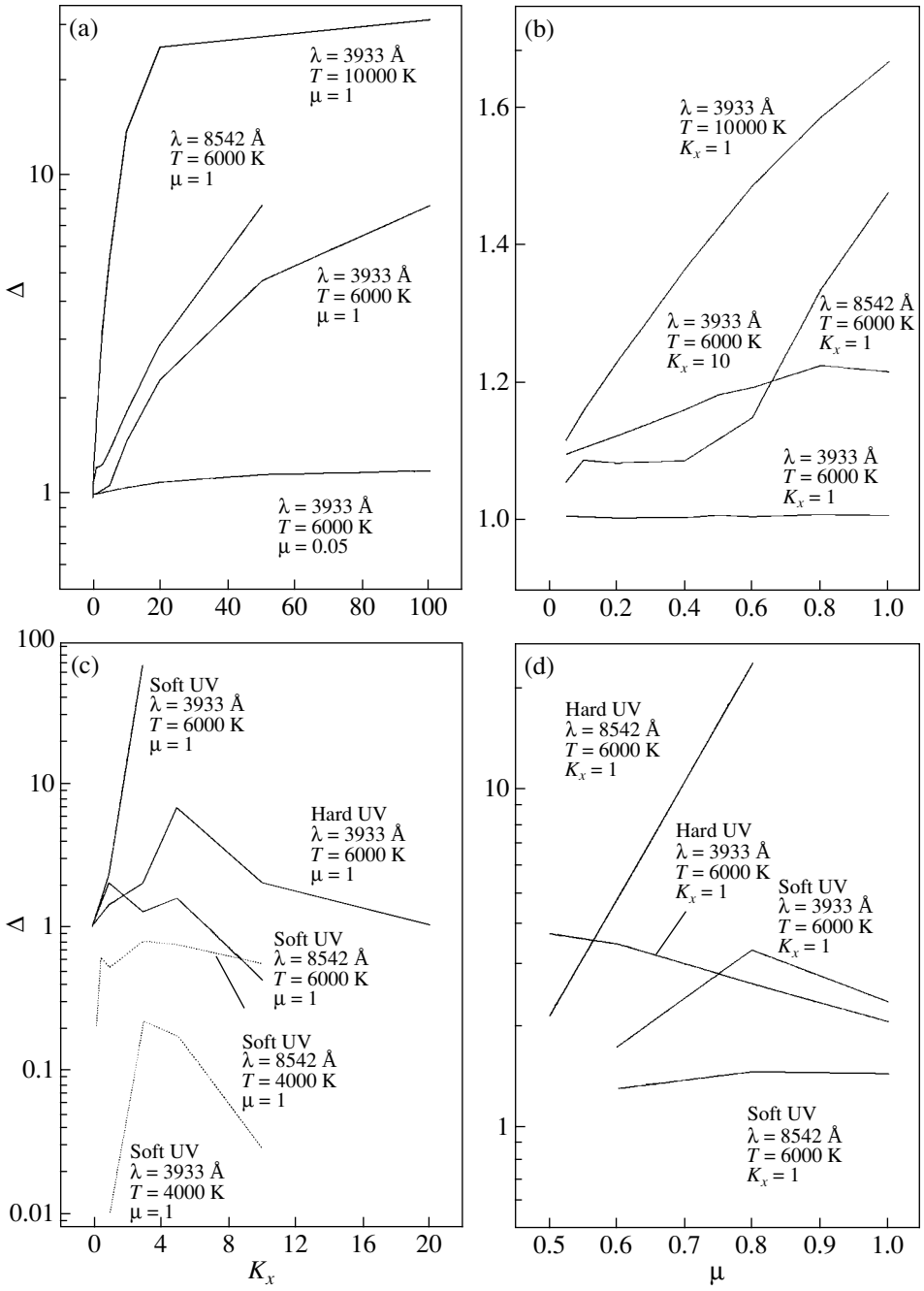

Fig. 4. Deviations from LTE Δ as a function of (a, c) the intensity K_x and (b, d) the angle of incidence μ of (a, b) X-ray and (c, d) UV external radiation for the $\lambda\lambda$3933, 8542 Å lines. The solid curves represent lines with positive LTE and non-LTE equivalent widths, and the dashed curves, those with negative equivalent widths.

non-LTE effects results in a systematic amplification of the CaII absorption lines that increases with K_x.

In a nonirradiated atmosphere with $T_{eff} =$ 10 000 K, the moderate "overionization" of the $4s$ ground state weakens the $\lambda\lambda$3933, 3968 Å doublet lines (Fig. 3c) compared with the LTE case. In the presence of external radiation, as in the atmospheres with $T_{eff} = 6000$ K, a hot chromosphere with a stronger source function forms in high layers. However, due to the weakness of all the CaII lines, they are formed in layers near the temperature minimum and remain in absorption even under LTE conditions. Qualitatively, the impact of non-LTE effects on the line profiles is the same as in the case of a cool atmosphere—strengthening of the lines that

increases with the intensity of the external radiation (Fig. 3c).

As was shown in [25], varying the angle of incidence of the external radiation from $\mu = 1.0$ to $\mu = 0.05$ increases the Planck function in the hot chromosphere and decreases the Planck function at the depth of formation of the continuum, which strengthens the emission components of the LTE line profiles (Fig. 3d). However, the enhancement of the "superrecombination" of the $4s$ and $3d$ levels in chromospheric layers overall compensates the increase of $B_\nu(T)$. Therefore, in stellar atmospheres with various T_{eff}, non-LTE effects in the CaII lines increase as μ decreases, while the emission components in their non-LTE profiles are strengthened only slightly (Fig. 3d).

To characterize the non-LTE deviations in the CaII lines, we introduce the parameter

$$\Delta = \frac{W_{\text{nonLTE}}}{W_{\text{LTE}}}, \qquad (6)$$

where W_{nonLTE} and W_{LTE} are the equivalent widths of the non-LTE and LTE lines, respectively. The distribution of this parameter for various K_x and μ values is presented in Fig. 4. We calculated the equivalent widths within ±25 Å of the center of the resonance doublet and within ±20 Å of the center of the IR triplet; the wings of the Balmer and Paschen hydrogen lines were included in the continuum.

Increasing K_x leads to a growth in Δ for all type lines. K_x can depend on Δ both linearly (λ3933 Å, $T_{eff} = 6000$ K, $\mu = 1.0$—Fig. 4a) and in more complex ways ($T_{eff} = 6000$ K, $\mu = 0.05$—Fig. 4a; $T_{eff} = 10\,000$ K, $\mu = 1.0$—Fig. 4a). As a rule, increasing μ from 0.05 to 1.0 enhances non-LTE effects (λ3933 Å, $T_{eff} = 6000$–$10\,000$ K, $K_x = 1.0$—Fig. 4b), which can display a maximum (λ8542 Å, $T_{eff} = 6000$ K, $K_x = 1.0$—Fig. 4b).

Thus, reflection effects at the surfaces of the secondary components in X-ray binaries cannot lead to the appearance of appreciable CaII emission lines, and the intensity of the corresponding absorption lines is determined by the electron temperature at the depth of formation of the continuum in an irradiated atmosphere. No unambiguous relationship between the non-LTE deviations in the CaII lines and the intensity or angle of incidence of the external X-ray radiation K_x has been found. Therefore, special non-LTE calculations of line profiles are required for the analysis of spectra of close binaries in which the effects of irradiation by X-ray sources are important.

2.2. Hard UV Radiation with $T_{rad} = 50\,000$ K

As was shown in [16, 26], the presence of hard UV irradiation from a white dwarf with $T_{eff} > 50\,000$ K results in the formation of a high-temperature chromosphere in the stellar atmosphere due to the large heating function of the gas in the Lyman continuum (Fig. 2c). The lower boundary of the Lyman chromosphere lies at the depth $\log \tau_r = -2.8$ to -1.8, and the temperature in this region, $T_e = 12\,000$–$14\,000$ K, exceeds the temperature in the first temperature-instability zone, $T_e = 8000$–$12\,000$ K. At the same time, in the atmospheres of cool stars ($T_{eff} \approx 6000$ K) with irradiation intensities up to $K_x = 10.0$, a secondary chromosphere is formed with $T_e \approx 7000$–8000 K, which is heated by the external radiation flux at wavelengths $912 < \lambda < 3000$ Å. No more than 10% of the incident flux reaches layers with $\log \tau_r > -0.8$, so that they are not significantly heated. At temperatures $T_e > 8500$ K and wavelengths $1100 < \lambda < 3000$ Å, the absorption coefficient approaches the Rosseland value, which results in the disappearance of the secondary chromosphere and more efficient heating of the region of the continuum formation in atmospheres with strong irradiation ($K_x = 100.0$) or high effective temperatures ($T_{eff} > 9000$ K).

Three regions can be delineated in the structure of the intrinsic radiation field of the irradiated atmosphere.

(1) In the Lyman chromosphere, $J_\nu \ll S_\nu$ at all wavelengths.

(2) In the secondary chromosphere, at wavelengths $912 < \lambda < 2000$ Å, the mean intensity J_ν is determined by the strong radiation of the Lyman chromosphere and exceeds S_ν. At wavelengths $\lambda > 2000$ Å, the influence of the Lyman chromosphere decreases and $J_\nu < S_\nu$.

(3) In layers with $\log \tau_r > -1.0$, J_ν is determined mainly by the source function at the depth of formation of the continuum; i.e. the conditions are close to those in a nonirradiated atmosphere.

Figure 5a presents distributions of the deviations from LTE in the CaII level populations, using the atmosphere with $T_{eff} = 6000$ K, $K_x = 1.0$, and $\mu = 1.0$ as an example. The non-LTE deviations are determined mainly by the intrinsic radiation field of the star, since more than 85% of the external flux with $T_{rad} = 50\,000$ K is confined to the Lyman continuum, where the contribution of CaII to the total absorption coefficient is small. Ionization by the external radiation with $912 < \lambda < 1600$ Å is more efficient for the $3d$ and $4p$ levels (with threshold cross sections of $\sigma_0 = 7.5$ and 3.2 Mbarn, respectively) than for the $4s$ level ($\sigma_0 = 0.3$ Mbarn).

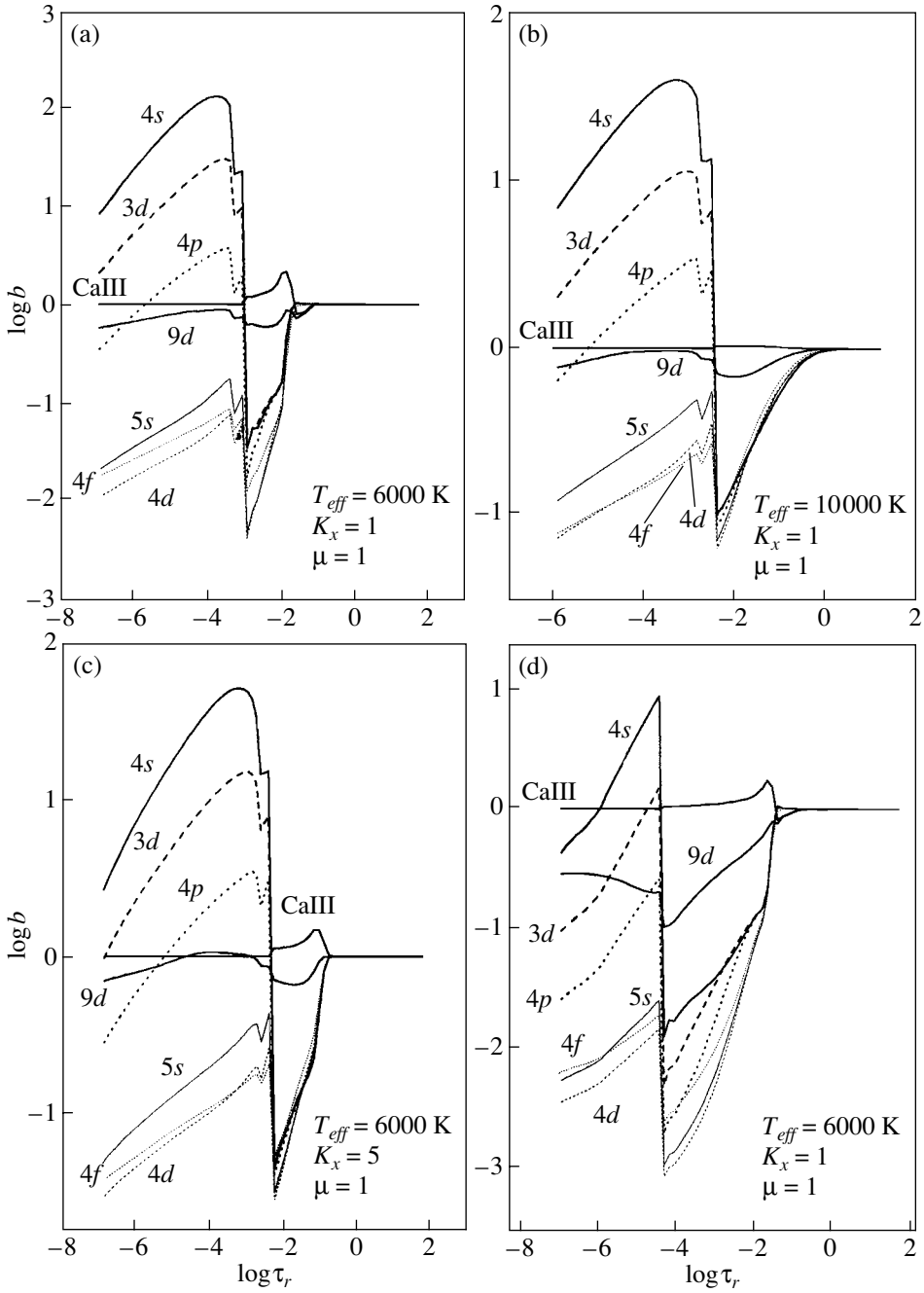

Fig. 5. Distribution of b factors of the CaII ground levels with the Rosseland opacity τ_r in the atmospheres of stars with (a, b) hard and (c, d) soft UV irradiation of various intensities.

In layers with $\log \tau_r > -1.0$, the LTE conditions characteristic of a nonirradiated atmosphere are fully preserved. In the secondary chromosphere, however, ionization by UV radiation from the $3d$ and $4p$ levels dominates over collisional recombination to highly excited CaII levels. Therefore, the $3d$ and $4p$ levels and the CaII ground state, which is connected to them by collisional transitions, are equally underpopulated ($\log b = -1.0$ to -1.6). In the Lyman chromosphere, the fact that S_ν dominates over J_ν results in recombination from the CaIII ground ionization state to all CaII levels and the strong super-recombination of its $4s$ ground state ($\log b = 2.0$). The high efficiency of spontaneous line transitions leads to a strong gradation of the b factors of the lower CaII levels, for which $\log b_i - \log b_j = 0.8-1.7$ for the $\lambda\lambda$3933, 3968 Å doublet and the $\lambda\lambda$8498, 8542, 8662 Å triplet lines.

When the intensity of the external radiation is

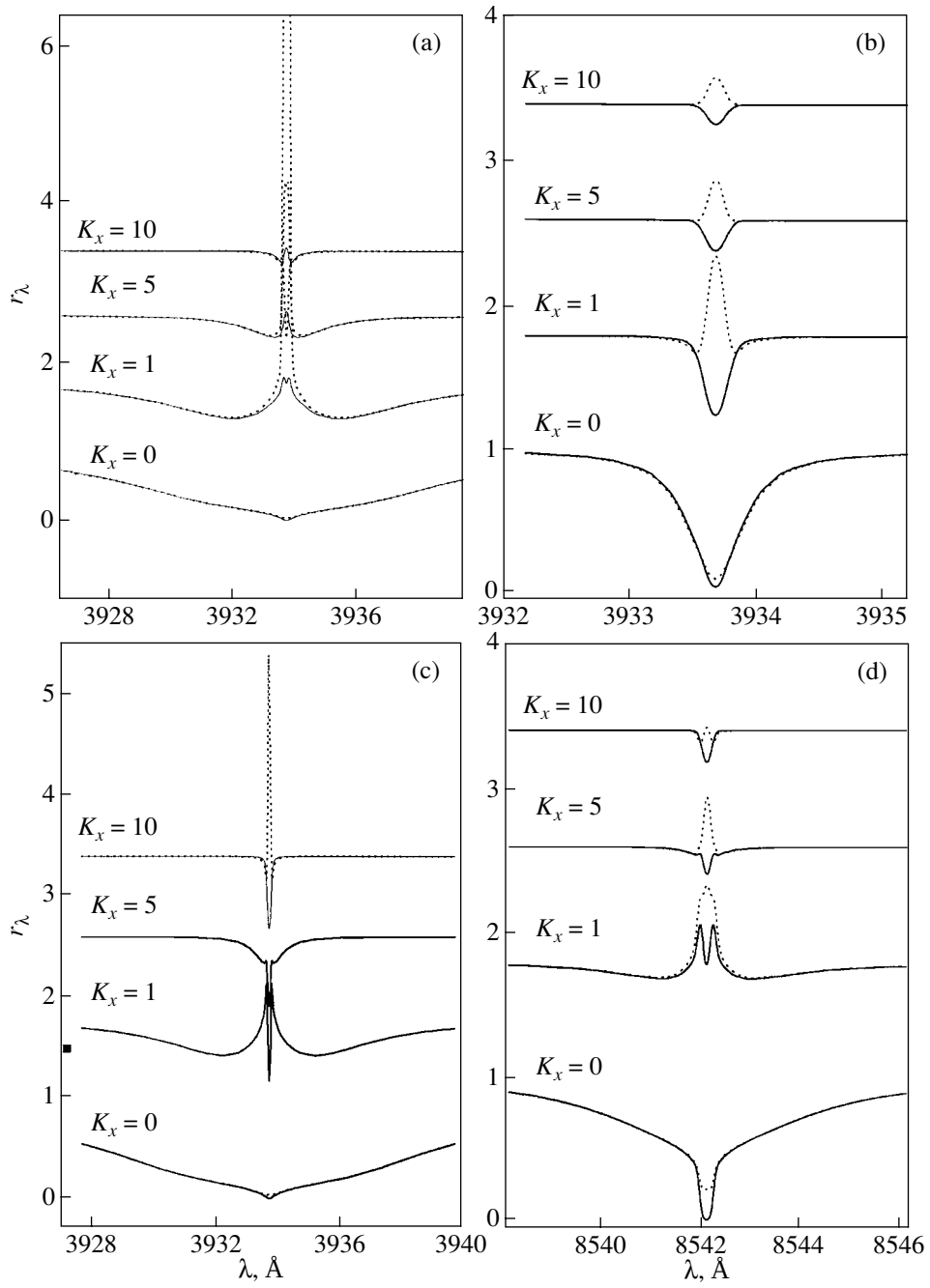

Fig. 6. Non-LTE and LTE profiles of the (a–c) λ3933 Å and (d) λ8542 Å lines in the spectra of stellar atmospheres with (a, c, d) $T_{eff} = 6000$ K and (b) $T_{eff} = 10\,000$ K with external (a, b) hard and (c, d) soft UV irradiation of various intensities for $\mu = 1.0$. The notation is the same as in Fig. 3. The profiles have been given sequential shifts of 0.8 along the vertical axis.

increased to $K_x = 10.0$, the non-LTE deviations in the CaII level populations in layers with $\log \tau_r > -2.5$ remain. However, the increase in the temperature in these layers with increasing K_x strengthens the radiation field at frequencies corresponding to ionization from lower levels and weakens the CaII subordinate lines. As a result, the effects of the superrecombination of the $4s$ level in the Lyman chromosphere decrease to $\log b = 1.3$.

This characteristic formation of CaII non-LTE populations in atmospheres with hard UV irradiation remains in all stars with $T_{eff} = 4000$–$10\,000$ K (Figs. 5a, 5b). Note that the b factors of the $4s$ and $3d$ levels in the Lyman chromosphere decrease, while they increase by $\Delta \log b = 0.40$ in the sec-

ondary chromosphere when the effective temperature increases from $T_{eff} = 4000$ K to $T_{eff} = 10\,000$ K.

The shapes of the CaII line profiles in the atmospheres with UV irradiation are determined by the depth of their formation. For the atmosphere with $T_{eff} = 4000$ K and weak irradiation ($K_x = 1.0$), the core and wings of the $\lambda\lambda$3933, 3968 Å doublet lines in the LTE approximation are formed in the Lyman and secondary chromospheres and display strong emission (Fig. 6a). The superionization of the CaII levels shifts the depth of formation of the line cores by $\Delta \log \tau_r = 1.1-1.3$ into the region occupied only by the secondary chromosphere. As a result, the $\lambda\lambda$3933, 3968 Å lines display moderate non-LTE emission profiles whose equivalent widths are a factor of 8–12 smaller than in the LTE case. When the external radiation increases to $K_x = 10.0-20.0$, the lower boundary of the Lyman chromosphere and the region of formation of the lines shift synchronously by $\Delta \log \tau_r = 1.0-1.3$. As a result, the LTE and non-LTE profiles of the CaII emission lines do not change qualitatively; however, their intensity is reduced by a factor of 2.8–3.9 due to the increase in the continuum radiation.

In the atmospheres with $T_{eff} = 6000$ K and $K_x = 1.0-10.0$, the lines of the resonance doublet are formed $\Delta \log \tau_r = 1.4$ deeper than in the corresponding atmospheres with $T_{eff} = 4000$ K; they are observed in moderate emission for LTE and in absorption with weak core emission for non-LTE (Fig. 6b). Overall, the profile shape is qualitatively preserved in the cases of both higher intensity of the external irradiation and atmospheres with higher temperatures; however, the lines weaken rapidly due to the ionization of CaII. Figures 4c and 4d illustrate the corresponding variations of Δ for various CaII lines and model atmospheres.

The CaII emission components can only be formed in cool atmospheres with weak (to $K_x = 5.0$) hard UV irradiation. At wavelengths $\Delta\lambda = 3600-5000$ Å, however, the radiation of these stars will not exceed 10% of the radiation of the hot components. Therefore, we recommend the IR triplet $\lambda\lambda$8498, 8542, 8662 Å for the analysis of reflection effects in CaII lines.

2.3. Soft UV Radiation with $T_{rad} = 15\,000$ K

The temperature structures of the atmospheres with hard and soft UV irradiation qualitatively coincide (Figs. 2c, 2d, models with $T_{eff} = 6000$ K). However, the fraction of soft UV radiation with $T_{rad} = 13\,000-18\,000$ K lying within the Lyman continuum does not exceed 15%. Therefore, the Lyman chromospheres in the atmospheres with soft irradiation are cooler by a factor of 1.3–1.4 and shifted to higher layers by $\Delta \log \tau_r = -1.0$ to -2.0 (Fig. 2d). At the same time, the increase of the radiation at wavelengths $912 < \lambda < 3000$ Å fosters more efficient heating of the secondary chromosphere (by a factor of 1.4) and of layers at the depth at which the continuum is formed (by a factor of 1.9–2.3).

The similarity of the temperature structures of the atmospheres with soft and hard UV irradiation leads to similar relations between the source functions and mean intensities of the radiation field (see above), as well as similar distributions of the b factors of the main levels (Figs. 6a, 6d). However, in the atmospheres with soft UV irradiation, the incident flux at $912 < \lambda < 1600$ Å interacts directly with CaII ions, enhancing the ionization. Our calculations indicate that, in atmospheric layers with $\log \tau_r < -1.0$ in stars with $T_{eff} = 4000-7000$ K and external radiation with $K_x = 1.0-10.0$, the ionization of Ca ions by the external radiation exceeds ionization by the intrinsic radiation by a factor of three to six. Ionization by the external radiation is more efficient for the $4p$ level, which has an ionization threshold of $\lambda = 1419$ Å, than for the $3d$ ($\lambda = 1219$ Å) and $4s$ ($\lambda = 1044$ Å) levels. As a result, the CaII ions are in a state of superionization for essentially all levels with $-3.5 < \log \tau_r < -0.3$, with the b factor of the ground state decreased to $\log b_i = -1.4$. At the same time, the underpopulation of the $4p$ level exceeds the underpopulations of the lower levels of the $4s-4p$, $3d-4p$ transitions by factors of 5–7 and 2.5–3.5, respectively (Fig. 6b). Similar trends are preserved in all atmospheres with $T_{eff} = 4000-6000$ K with soft UV irradiation with intensities up to $K_x = 10.0$.

Increasing the fraction of soft radiation in the incident flux weakens the core emission components in the LTE profiles of the CaII lines and the absorption components in their wings (Fig. 6a, 6c). This is due to the weakening of the Lyman chromosphere and the increase in the continuum flux. The non-LTE populations of the CaII levels depend on the parameters of the external UV radiation more weakly than they depend on the atmosphere of the star as a whole. As a result, the non-LTE line profiles in the spectra of stars with hard and soft UV irradiation differ only slightly (Figs. 6a, 6c). The formation of purely absorption non-LTE profiles and the presence of strong deviations from LTE are characteristic of the atmospheres with $T_{eff} = 6000$ K (Fig. 6c). In the spectra of atmospheres with $T_{eff} = 4000$ K and irradiations up to $K_x = 20.0$, the strong emission wings in the CaII lines are formed primarily in layers with $\log \tau_r < -2.5$ to 0.0, with minimum deviations from LTE in the level populations. Therefore, as a whole, the non-LTE lines of the resonance doublet and IR triplet are

in emission; their equivalent widths reach $W_{\rm nonLTE} = 15$ Å and are close to their LTE values. Figures 4c and 4d present the corresponding variations of Δ for various values of the external irradiation K_x and μ. It is obvious that the Δ values for the $\lambda\lambda$3933, 8542 Å lines for a star with $T_{eff} = 4000$ K differ from unity by no more than 30–40%, so that LTE can be assumed when analyzing the observed spectra and the temperature structure of such irradiated atmospheres.

Thus, the CaII emission lines are a good indicator of reflection effects in close binaries with soft UV irradiation. In this case, the intensity of the calculated non-LTE emission-line profiles for the $\lambda\lambda$3933, 3968 Å doublet and $\lambda\lambda$8498, 8542, 8662 Å triplet show that they are all suitable for analyses of reflection effects, on a par with photometric observations.

3. FORMATION OF CaII LINES IN THE SPECTRA OF PRECATACLYSMIC VARIABLES

We have calculated the profiles and equivalent widths of CaII lines in the spectra of four precataclysmic variables—close binaries that contain a hot white dwarf or subdwarf and a late-type main-sequence star. Most close binaries of this type display substantial reflection effects in their light curves, due to the large (a factor of 4–40!) difference of the temperatures of their components. We suggested a method for modeling these effects in [27] and [33]. The SPECTR package based on this technique includes code to partition the surface of the irradiated secondary into rings with their centers along the semimajor axis of the system and to determine the parameters of the atmosphere and incident flux for each ring. The calculations of the atmosphere's structure and the radiated spectra are fully analogous to those given in [19]. Finally, the SPECTR package sums the radiation from all the rings for both components, taking into account their radii and radial and rotational velocities. In our present study, we calculated the CaII line profiles in the spectra of these rings taking into account the b factors of the levels, which had been previously calculated using the NONLTE3 code [19] and models for the irradiated atmospheres.

Parameters of precataclysmic variables

Parameter	BE UMa	EG UMa	MS Peg	HR Cam
P_{orb}, d	2.291166	0.667579	0.173666	0.103064
$a/r_\odot$	8.76	3.20	1.17	0.74
i, deg	82.4	58.4	69.2	29.3
$m^w/m_\odot$	0.90	0.63	0.48	0.41
$r^w/r_\odot$	0.078	0.0122	0.015	0.018
T^w_{eff}, K	105 000	13 125	22 200	19 000
$m^r/m_\odot$	0.83	0.36	0.22	0.096
$r^r/r_\odot$	0.96	0.32	0.18	0.125
T^r_{eff}, K	5150	3440	3650	2900

We studied only precataclysmic variables with complete sets of parameters: BE UMa [26, 28–30], EG UMa [31, 32], MS Peg [18, 33], and HR Cam [17, 34]. The table presents a list of the parameters used.

Figure 7 presents the theoretical non-LTE CaII line profiles at various orbital phases, as well as the theoretical and observed variations of their equivalent width as a function of phase.

Let us consider the characteristics of the CaII-line formation for each object individually.

BE UMa. This system contains a blue dwarf with a very high temperature $T_{eff} \approx 105\,000$ K [28], leading to the largest reflection effects observed among all precataclysmic variables, reaching $\Delta m_V \approx 1.5^m$. At phases close to the maximum brightness, the spectra contain emission lines of HI, HeI, HeII, and multiply ionized heavy elements but no CaII lines [27]. In our model for BE UMa, the temperature of the layers where the continuum is formed at the center of the hot spot on the surface of the secondary reaches $T_e \approx 9500$ K. As a result, the equivalent width of the λ3933 Å emission line does not exceed $W_{\rm LTE} = 8$ mÅ in the LTE approximation. Taking into account deviations of LTE leads to the complete disappearance of the λ3933 Å emission component. We therefore conclude that CaII lines cannot be detected in the spectrum of BE UMa.

EG UMa. The system's brightness undergoes periodic variations with a small amplitude, $\Delta m_R = 0.05^m$ [31], as well as flares by up to $\Delta m_V = 0.5^m$ [35], associated with the fact that the secondary is a magnetic red UV Ceti dwarf [31]. The spectra of EG UMa display strong Balmer emission lines (up to H_{11}) and CaII $\lambda\lambda$3933, 3968 Å lines, whose intensities increase by factors of three to five during flares. The photometric and spectroscopic observations of [31] do not support the presence of reflection effects. However, theoretical modeling of the system's spectra [32] indicated that these effects could be present in the CaII $\lambda\lambda$3933, 3968 Å emission lines during the quiescent state of the red dwarf. Figures 7e and 7f present our non-LTE calculations of the CaII λ3933 Å line performed using the model for EG UMa of [32]. Despite the fact that deviations from LTE reduce the emission in this line, the total amplitude of the variations of its equivalent width $W_{\rm nonLTE}$ is consistent with the observational data of [32, 36].

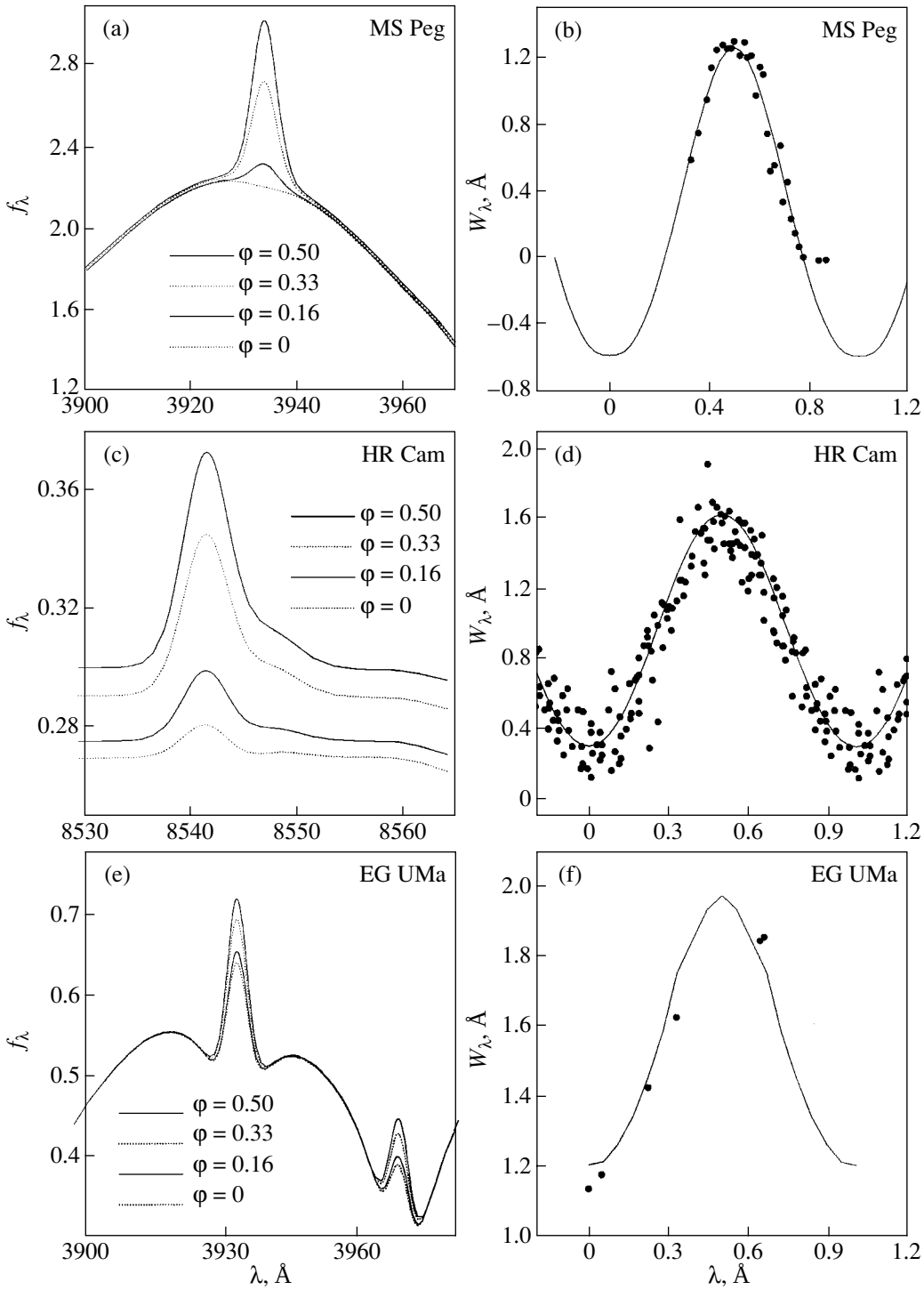

Fig. 7. Theoretical profiles of CaII lines at various phases of the orbital period and curves of their equivalent widths for (a, b) MS Peg, (c, d) HR Cam, and (e, f) EG UMa. In graphs (b), (d), and (f), the theoretical curves are shown by the solid lines, and the observational data, from [17, 33, 32] by the points.

Thus, the conclusion of [32] that reflection effects should be detectable in the spectrum of EG UMa remains valid.

MS Peg. The light curves of this system display substantial reflection effects, from $\Delta m_B = 0.06^m$ to $\Delta m_V = 0.11^m$, and its spectra contain numerous emission lines of hydrogen and heavy elements. It is noted in [33] that accurate quantitative modeling of all the reflection effects is possible using a single

set of parameters for the system. Note, however, that the absence of UV observations of MS Peg leads to uncertainties in the temperature of the white dwarf of about $\Delta T_{eff} \approx 600$ K and in the radius of the secondary of up to 7%. Figures 7a and 7b present the results of our non-LTE calculations of the CaII λ3933 Å line. Non-LTE effects reduce the emission in this line by no more than 10%, and the variations with orbital phase are fully preserved. Modeling of the variations of the observed W_λ (Fig. 7b) measured from the spectra of [33] indicates that the calcium abundance in the atmosphere of the red dwarf is close to the solar value, $[\mathrm{Ca/H}] = -0.08$, consistent with the overall metallicity, $[\mathrm{M/H}] = 0.00 \pm 0.2$ [33].

HR Cam. Due to the low temperature of the white dwarf, $T_{eff} = 19\,000$ K, reflection effects are seen only in the red and IR ($\Delta m_V = 0.015^m$, $\Delta m_I = 0.09^m$ [17]). Emission components whose intensities depend strictly on the orbital phase are observed in the H_α line and CaII $\lambda\lambda$8498, 8542, 8662 Å triplet. Therefore, we modeled the CaII λ8542 Å line in HR Cam; the results are presented in Figs. 7c and 7d. In the atmosphere of the red dwarf, CaII lines are formed in the region where ionized calcium dominates; the deviations from LTE in these lines are the smallest among the studied objects and do not exceed 2–3% of their equivalent widths. The observed amplitudes and variations of the equivalent width of the CaII λ8542 Å line are consistent with the theoretical solar calcium abundance, $\log \varepsilon(\mathrm{Ca}) = 6.32$ [33] (Fig. 7d), confirming the correctness of the system parameters presented in [17].

Overall, we conclude that, in MS Peg, HR Cam, and similar systems containing cool white dwarfs (LM Com, CC Cet, BPM 6502, etc.), CaII lines are formed in the atmospheres of the secondaries under conditions that are close to LTE. Therefore, LTE calculations based on models of irradiated atmospheres can be used to quantitatively analyze the reflection effects in such systems and to determine the system parameters.

4. CONCLUSIONS

We have determined the conditions and mechanisms for the formation of CaII emission lines in the spectra of binaries with various types of irradiation of their components. Our results for CaII lines can with minor corrections be extended to lines of other atoms formed under similar conditions (FeII, MgII, SiII, SI, etc.), which are observed in both semidetached and detached binaries. These results can provide a more detailed understanding of the radiative interaction of the components of binaries, which can be used to determine their basic parameters. The following conclusions are of particular interest for further studies.

(1) Taking into account deviations from LTE in the atmospheres of A–M stars with external X-ray and UV irradiation decreases the reflection effects in strong CaII lines.

(2) CaII lines in the spectra of optically thick stellar atmospheres irradiated by X rays do not display emission components. Therefore, cataclysmic variables with emission lines of ionized calcium must contain a substantial amount of optically thin plasma. For example, the CaII emission lines in low-mass RE And and SS Aur variables are formed in thin accretion disks, whose luminosities undoubtedly exceed those of the M-star secondaries. The CaII emission lines in the spectra of NZ Her objects may arise in the systems' envelopes, since, as a rule, the luminosities of their accretion disks are lower than the luminosities of the massive secondaries.

(3) Spectra of stars with UV irradiation can contain CaII emission lines only if this ion is the dominant ionization state in atmospheric layers close to the depth of formation of the continuum. This will be the case if the intensity of the incident flux does not exceed the total luminosity of a star with $T_{eff} = 6000$ K by more than a factor of three or the luminosity of a star with $T_{eff} = 4000$ K by more than a factor of 15. Thus, CaII emission lines cannot be formed in young close binaries that have undergone a common envelope stage and contain blue subdwarfs (UU Sge, V477 Lyr, HW Vir) or hot white dwarfs (BE UMa, V664 Cas, and others).

(4) Spectra of several symbiotic variables with a hot primary and M-giant or supergiant secondary can display CaII lines that originate due to reflection effects. These lines are suitable for analyses of reflection effects and the temperature structure of the secondary atmospheres only if a non-LTE approach is used.

(5) The CaII emission lines in the spectra of close binaries with cool white dwarfs ($15\,000 < T_{eff} < 35\,000$ K) are formed in the irradiated atmospheres of the secondaries under conditions that are close to thermalization. Therefore, these lines can be used in studies of the reflection effects and calcium abundances even using an LTE approximation. As we have shown, such studies yield the most adequate results for systems with white dwarfs with temperatures $T_{eff} < 20\,000$ K. The reflection effects in such systems do not exceed $\Delta m_R = 0.03^m$ (HR Cam) and are completely absent in some cases (EG UMa), while the equivalent widths of the resonance doublet and IR triplet lines vary by 2–4 Å and can easily be analyzed, even using moderate-resolution spectra.

ACKNOWLEDGMENTS

We thank V.F. Suleimanov and I.F. Bikmaev for useful discussions and N.N. Shimanskaya for her assistance in measuring the equivalent widths in the spectra of MS Peg. This work was supported by the Russian Foundation for Basic Research (project nos. 99-02-17488 and 01-02-06065). V.V. Shimanskiĭ and D.V. Ivanova separately thank the support of the RFBR for several IAU projects (nos. 02-02-06591, 01-02-06065, and 03-02-06763).

REFERENCES

1. R. E. Wilson, Astrophys. J. **234**, 1054 (1979).
2. G. Hill, *LIGHT2*, *User Manual* (Internal Publ. Dominion Astrophys. Observ., 1987).
3. E. A. Antokhina, Astron. Zh. **65**, 1164 (1988) [Sov. Astron. **32**, 608 (1988)].
4. D. L. Pollacco and S. A. Bell, Mon. Not. R. Astron. Soc. **262**, 377 (1993).
5. D. L. Pollacco and S. A. Bell, Mon. Not. R. Astron. Soc. **267**, 452 (1994).
6. R. W. Hilditch, T. J. Harries, and G. Hill, Mon. Not. R. Astron. Soc. **279**, 1380 (1996).
7. E. A. Antokhina and A. M. Cherepashchuk, Astron. Zh. **64**, 562 (1987) [Sov. Astron. **31**, 295 (1987)].
8. E. A. Antokhina, E. P. Pavlenko, A. M. Cherepashchuk, and S. Yu. Shugarov, Astron. Zh. **70**, 804 (1993) [Astron. Rep. **37**, 407 (1993)].
9. J. H. Wood, E. H. Zhang, and E. L. Robinson, Mon. Not. R. Astron. Soc. **261**, 103 (1993).
10. K. Wlodarczyk and P. Olszewski, Acta Astron. **44**, 407 (1994).
11. O. Cakiri and A. Devlen, Astron. Astrophys., Suppl. Ser. **136**, 27 (1999).
12. G. Williams, Astrophys. J., Suppl. Ser. **53**, 523 (1983).
13. J. B. Hutching, E. M. Girson, D. Crampton, and W. A. Fisher, Astrophys. J. **292**, 670 (1985).
14. U. Munari, T. Zwitter, and A. Bragaglia, Astron. Astrophys., Suppl. Ser. **122**, 495 (1997).
15. U. Munari and T. Zwitter, Astron. Astrophys., Suppl. Ser. **128**, 277 (1998).
16. N. A. Sakhibullin and V. V. Shimansky, Odessa Astron. Publ. **10**, 94 (1998).
17. P. F. L. Maxted, T. R. Marsh, C. Moram, *et al.*, Mon. Not. R. Astron. Soc. **300**, 1225 (1998).
18. G. D. Schmidt, P. S. Smith, and D. A. Harvey, Astron. J. **110**, 398 (1995).
19. D. V. Ivanova, N. A. Sakhibullin, and V. V. Shimanskiĭ, Astron. Zh. **79**, 433 (2002) [Astron. Rep. **46**, 390 (2002)].
20. E. Anders and N. Grevesse, Geochim. Cosmochim. Acta **53**, 197 (1989).
21. R. L. Kurucz, SAO CD-ROMs, Cambridge, MA02138, USA, 1994.
22. L. I. Mashonkina, N. N. Shimanskaya, and N. A. Sakhibullin, Astron. Zh. **73**, 212 (1996) [Astron. Rep. **40**, 187 (1996)].
23. J. H. Bruls, R. J. Rutten, and N. G. Shchukina, Astron. Astrophys. **265**, 237 (1992).
24. L. I. Mashonkina, V. V. Shimanskiĭ, and N. A. Sakhibullin, Astron. Zh. **77**, 893 (2000) [Astron. Rep. **44**, 790 (2000)].
25. N. A. Sakhibullin and V. V. Shimanskiĭ, Pis'ma Astron. Zh. **26**, 369 (2000) [Astron. Lett. **26**, 309 (2000)].
26. D. H. Ferguson and T. A. James, Astrophys. J., Suppl. Ser. **94**, 723 (1994).
27. N. A. Sakhibullin and V. V. Shimanskiĭ, Astron. Zh. **74**, 432 (1997) [Astron. Rep. **41**, 378 (1997)].
28. J. Liebert, R. W. Tweedy, R. Napiwotzki, and M. S. Fulbright, Astrophys. J. **441**, 424 (1995).
29. J. H. Wood, E. L. Robinson, and E. H. Zhang, Mon. Not. R. Astron. Soc. **277**, 87 (1995).
30. D. H. Ferguson, J. Liebert, S. Haas, *et al.*, Astrophys. J. **518**, 866 (1999).
31. J. N. Bleach, J. H. Wood, M. S. Catalan, *et al.*, Mon. Not. R. Astron. Soc. **312**, 70 (2000).
32. V. V. Shimanskiĭ and N. V. Borisov, Astron. Zh. **79**, 450 (2002) [Astron. Rep. **46**, 406 (2002)].
33. V. V. Shimanskiĭ, N. V. Borisov, and N. N. Shimanskaya, Astron. Zh. **80**, 830 (2003) [Astron. Rep. **47**, 763 (2003)].
34. T. R. Marsh and S. R. Duck, Mon. Not. R. Astron. Soc. **278**, 565 (1996).
35. S. Y. Shugarov, IAU Inf. Bull. Var. Stars, No. 2612 (1984).
36. J. R. Stauffer, Astron. J. **94**, 996 (1987).

Translated by K. Maslennikov

Astronomy Reports, Vol. 48, No. 6, 2004, pp. 492–510. Translated from Astronomicheskiĭ Zhurnal, Vol. 81, No. 6, 2004, pp. 541–560.

Chemical Composition of 15 Photometric Analogues of the Sun

A. I. Galeev[1,2], I. F. Bikmaev[1], F. A. Musaev[3], and G. A. Galazutdinov[3]

[1]*Kazan State University, Kremlevskaya ul. 18, 420008 Kazan, Russia*

[2]*Department of Physics, Kazan State Pedagogical University, Mezhlauk str. 1, Kazan, 420021 Russia*

[3]*Special Astrophysical Observatory, Russian Academy of Sciences, Nizhniĭ Arkhyz, Karachaĭ-Cherkessian Republic, 369167 Russia*

Received October 13, 2003; in final form, January 9, 2004

Abstract—The results of a spectroscopic analysis of 15 stars that are photometric analogues of the Sun are reported. The effective temperatures and surface gravities in the stellar atmospheres are derived from published photometric indices and the HIPPARCOS parallaxes. The abundances of 33 elements ranging from lithium to europium are analyzed based on high-dispersion spectra taken with the new Coudé echelle spectrometer of the Terskol Observatory in the northern Caucasus. The main parameters of most of the stars agree with the data of an [Fe/H] catalog published in 2001. Our study of the chemical compositions of the sample stars indicates that photometric analogues of the Sun can be divided into three groups according to their elemental abundances: six stars have solar chemical composition, four have abundance excesses, and five have some abundance deficiencies. The sample contains two metal-deficient subgiants (HD 133002 and HD 225239). Our results demonstrate that photometric similarity is not a sufficient criterion to consider a star as solar analogue. When several criteria, including chemical composition, are simultaneously taken into account, only four stars from the sample can be considered true solar analogues: HD 10307, HD 34411, HD 146233 (18 Sco), and HD 186427 (16 Cyg B). These results confirm the previously published suggestion that 18 Sco is the most probable twin of the Sun: essentially all the parameters of the two stars coincide within the errors. © *2004 MAIK "Nauka/Interperiodica"*.

1. INTRODUCTION

So-called solar analogues can be identified among solar-type stars, which make up a large group of late-F to early-K dwarfs located on or near the main sequence of the Hertzsprung–Russell diagram. According to the criteria of Soderblom and King [1], these stars must have temperatures within 500 K of the solar temperature and metallicities that differ from that of the Sun by no more than a factor of two. These objects must be no more than one magnitude from the main sequence and must not belong to close binaries (with periods of the order of 10 days).

Searching for a full analogue (twin) of the Sun remains an important problem. A solar twin is a star whose physical parameters—temperature, luminosity, mass, radius, rotational velocity, velocity field, age, magnetohydrodynamical structure, chemical composition, etc.—all coincide with the solar parameters within the errors. Such stars are taken [1] to have temperatures within 10 K of the solar temperature, metallicities within ±0.05 dex of the solar metallicity, ages with 1 Gyr of the solar age, etc. Table 1 gives the parameter intervals that enable a star to be classified as a solar analogue or twin (note that we give 50 K as the temperature tolerance for solar twins since this is the accuracy with which stellar temperatures can currently be determined). This table also gives the main parameters of the Sun. In 1997, Porto de Mello and da Silva [2] suggested the star 18 Sco (HD 146233) as the most likely solar twin. The main parameters of this star indeed match the criteria listed in Table 1.

Solar analogues are usually selected based on photometric parameters—the color indices and spectral energy distributions of these stars must be close to those of the Sun [3]. However, these are far from the only criteria used for selecting solar twins. In particular, chromospheric analogues [4] and analogues based on ultraviolet spectra [5, 6] have been identified. In her classic work, Cayrel de Strobel [7] identified 26 temperature-based solar analogues among stars in the HIPPARCOS catalog. Only five of the stars in this list are solar analogues according to three parameters simultaneously (temperature, luminosity, and metallicity). Objects with spectra similar to the solar spectrum can be considered spectroscopic analogues [8].

However, these criteria cannot by themselves conclusively identify solar analogues or twins, since the star must satisfy simultaneously all or most of the criteria, not just one of them. The atmospheric

1063-7729/04/4806-0492$26.00

chemical composition can serve as an additional objective criterion. It can be determined by applying the well-developed modern theory of stellar atmospheres to large numbers of lines of various elements in high-resolution spectra. The chemical compositions of solar-type stars remain virtually unchanged throughout their main-sequence lifetimes (except for the abundances of the lightest elements—hydrogen, helium, lithium, beryllium, and boron). However, the determination of stellar chemical compositions is a very labor-intensive task, beginning with the acquisition of high-quality spectra and their reduction and ending with allowance for the specific characteristics of theoretical modeling of spectral-line intensities.

We should therefore search for a chemical analogue of the Sun—a star whose elemental abundances (not only the abundance of iron) coincide with the corresponding solar abundances within the errors. The elemental abundances for solar-type stars can now be determined, on average, with accuracies of about 0.10–0.20 dex.

No specialized searches for chemical analogues of the Sun have been carried out previously, as solar-analogue candidates include many sixth- to seventh-magnitude stars for which it was not possible to obtain quality spectroscopic data until recently. The modest quality of plate spectra taken with classic spectrographs prevented detailed analyses of the chemical compositions of the atmospheres of cool stars for a large number of elements. The use of reticon linear arrays and CCDs increased the quality of the spectra obtained, but only the abundances of individual elements (carbon, oxygen, nitrogen [9–11]) or of light elements were analyzed in the 1980s. Such studies include the excellent work of Tomkin *et al.* [12], who analyzed the abundances of Na, Mg, Al, Si, Ca, and Sc in 20 disk stars.

In 1993, Edvardsson *et al.* [13] published their well-known paper presenting a detailed analysis of the elemental abundances of almost two hundred stars of the Galactic disk with metallicities $-1.0 <$ [Fe/H] $< +0.1$. In a series of papers, Carretta, Gratton, and Sneden (see [14]) reanalyzed the data of [13] and of other studies. High-quality spectra of 90 Galactic-disk stars taken with an echelle spectrometer equipped with a CCD detector mounted on a 2.16-m telescope allowed Chen *et al.* [15] to achieve even higher accuracy. The resulting trends for the abundances of various elements as functions of metallicity confirm the results of previous analyses. Reddy *et al.* [16] recently obtained high-dispersion spectra of 180 F–G stars and calculated local-thermodynamic-equilibrium (LTE) abundances for almost 30 elements. Analysis of these abundances and their dependence on [Fe/H] combined with data on space velocities and positions of the stars in the Galaxy enable the identification and comparison of the parameters of thick-disk and thin-disk stars.

Table 1. Intervals of stellar parameters for selection of solar analogues and solar twins compared to the corresponding solar parameters

Parameter	Analogue	Twin	Sun
T_{eff}, K	5200–6200	5720–5820	5770
$\log g$, dex	4.0–4.7	4.35–4.55	4.44
[Fe/H], dex	±0.30	±0.05	0.00
M_{bol}, mag.	4.2–5.2	4.5–5.0	4.75
Mass, $M_\odot$	0.8–1.2	0.9–1.1	1.0
Age, 10^9 yr	0.5–10	4–5	4.5

However, all the above authors analyzed extensive samples of stars with various atmospheric parameters, most of them metal poor, or, conversely, stars with [Me/H] > 0.1 [17, 18], whose elemental abundances reflect the chemical evolution of various populations of the stellar disk. There are essentially no studies focusing on a narrow interval of parameters, such as those of solar analogues; a notable exception is the work of Gaidos and Gonzalez [19], who derived the atmospheric parameters and chemical compositions for a group of "young" solar analogues.

Detailed spectroscopic analyses of stars as solar analogues have been performed only for components A and B of 16 Cyg [20] and the solar-twin candidate 18 Sco [21]. Friel *et al.* [20] used CCD observations to determine the main atmospheric parameters ($T_{\rm eff}$, $\log g$, [Fe/H], ξ_t) of 16 Cyg A and B and estimated their luminosities, chromospheric activity, and the abundances of eight elements. These parameters satisfy the requirements for a star to be a solar analogue, but the temperatures of the two stars differ slightly from that of the Sun. Both stars are somewhat overabundant in heavy elements and, most importantly, are older than the Sun.

Porto de Mello and da Silva [21] performed a similar analysis for HD 146233 (18 Sco, HR 6060). The results of their study indicate that virtually all parameters of this star are identical to the corresponding solar parameters within the errors, except for the somewhat higher abundances of some elements.

We continue here the above studies and perform a detailed analysis in order to search for probable chemical solar analogues, using the group of photometric solar analogues from [22] for this purpose. This sample is described in Section 2 and the observations are briefly outlined in Section 3. In Section 4, we give the derived atmospheric parameters, and in Section 5,

Table 2. Photometric solar analogues

Number	Name	α_{2000}	δ_{2000}	Spectrum	V	$B-V$
HD 146 233	18 Sco	$16^{\rm h}\ 15.6^{\rm m}$	$-08^\circ\ 22'$	G2Va	5.499^m	0.650^m
HD 159 222		17 32.0	+34 16	G2V	6.537	0.646
HD 186 408	16 Cyg A	19 41.8	+50 32	G1.5V	5.986	0.659
HD 186 427	16 Cyg B	19 41.9	+50 31	G2.5V	6.244	0.671
HD 187 237		19 48.0	+27 52	G2III	6.896	0.654
HD 187 923		19 52.2	+11 38	G0V	6.164	0.664
HD 4307	18 Cet	00 45.5	−12 53	G2V	6.158	0.612
HD 4915		00 51.2	−05 02	G0V	6.982	0.666
HD 8262		01 22.3	+18 41	G3V	6.973	0.630
HD 10 307	41 And	01 41.8	+42 37	G1.5V	4.965	0.623
HD 29 310	V998 Tau	04 37.5	+15 09	G1V	7.547	0.608
HD 34 411	λ Aur	05 19.1	+40 06	G2IV/V	4.705	0.622
HD 95 128	47 UMa	10 59.5	+40 26	G0V	5.037	0.622
HD 126 053		14 23.3	+01 14	G1V	6.266	0.644
HD 133 002		14 50.3	+82 31	F9V	5.643	0.682
HD 141 004	λ Ser	15 46.4	+07 21	G0V	4.419	0.611
HD 152 792		16 53.5	+42 49	G0V	6.827	0.645
HD 160 269	26 Dra	17 35.0	+61 52	G0Va	5.233	0.608
HD 168 874		18 20.8	+27 32	G2IV	7.014	0.637
HD 177 082		19 02.6	+14 34	G2V	6.895	0.641
HD 190 771		20 05.2	+38 29	G5IV	6.185	0.668
HD 197 076		20 40.8	+19 56	G5V	6.444	0.628
HD 222 143		23 38.0	+46 12	G5	6.591	0.652
HD 225 239		00 04.9	+34 40	G2V	6.111	0.640

the errors of these parameters and of the elemental abundances. Section 6 reports the abundances themselves and compares them with previously published data. We analyze and discuss our results in Section 7.

2. SAMPLE OF PHOTOMETRIC SOLAR ANALOGUES

We study here the sample of photometric solar analogues proposed by Kharitonov and Mironov [22], who selected these stars based on the similarity of their photometric indices adopted from three different catalogs to the corresponding solar indices. Note that the photometric color indices of the Sun are not precisely known; in particular, the $B-V$ color indices published by different authors vary from 0.62 to 0.68.

Kharitonov and Mironov [22] selected six stars with color indices close to the solar indices in all three (Vilnius, UBV, and $WBVR$) photometric systems and another 18 stars that satisfied the similarity criteria for two of the three systems. Table 2 lists the HD numbers, names, J2000 coordinates, spectral types,

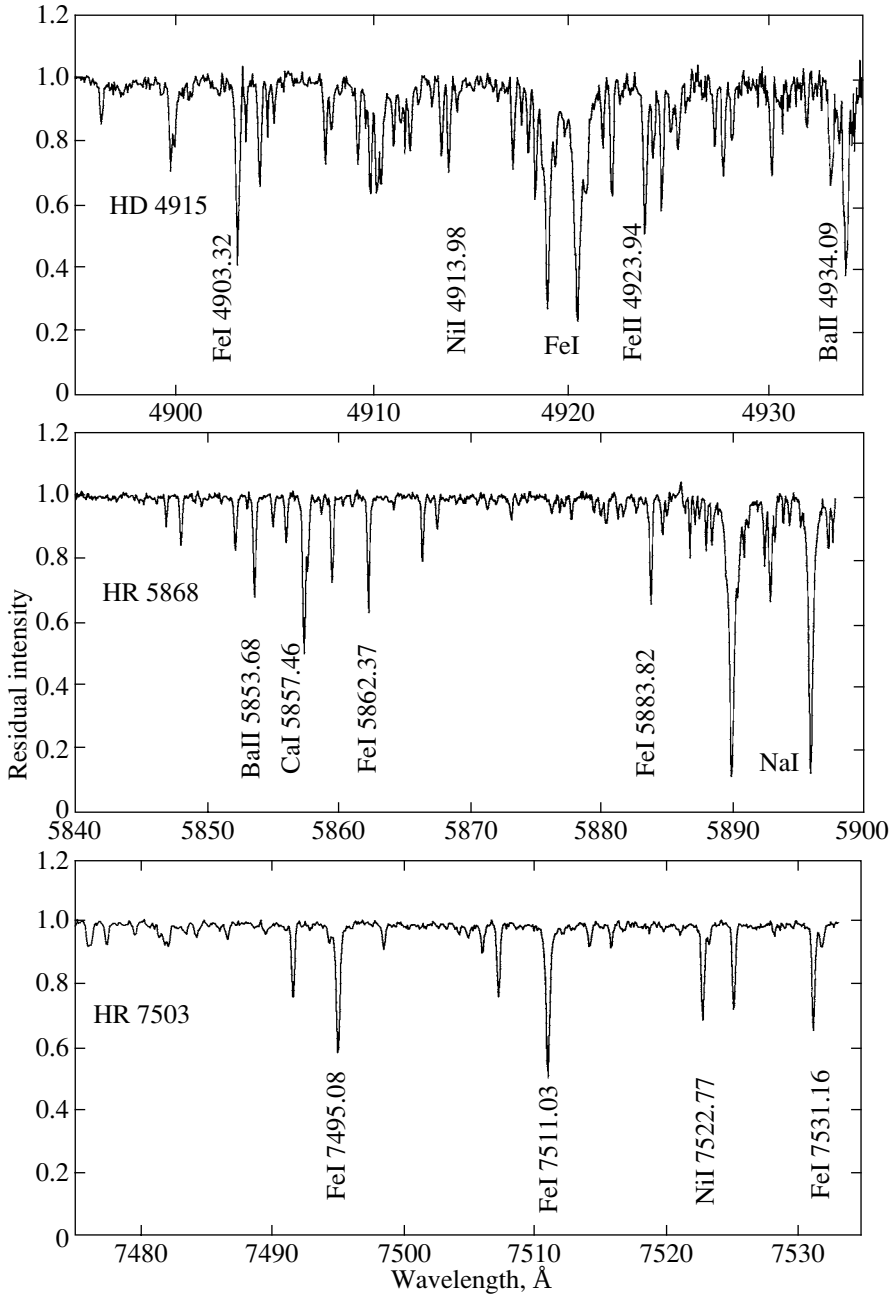

Fig. 1. Characteristic fragments of the spectra of three stars of the sample.

V magnitudes, and $B-V$ color indices for all 24 stars. The stars in this sample have spectral types G0–G5.

All the sample stars are fairly nearby, located at heliocentric distances of 10–40 pc, and have apparent magnitudes 4^m-7^m, enabling spectroscopic observations with high resolution on 2-m-class telescopes. Analysis of the data in Table 2 shows that some of these stars are not eligible to be solar analogues. For example, HD 187237 (which is among the first six closest solar analogues) is spectroscopically classified as a giant (G2III), and HD 29310 is a variable (V998 Tauri). This contamination is due to the fact that Kharitonov and Mironov [22] selected their solar-analogue candidates based exclusively on photometric criteria without taking other factors into account.

The sample contains a number of well-known stars, such as the solar-twin candidate HD 146233 (18 Sco) and components A and B of 16 Cyg, which have long been known as solar analogues. In her review, Cayrel de Strobel [7] analyzed half of the 24 sample objects and identified six of them (HD 126053, HD 146233, HD 160269, HD 186408, HD 186427,

and HD 187923) as temperature analogues of the Sun (see Table 5 in [7]). This list also contains two stars with planets—47 UMa and 16 Cyg B.

3. OBSERVATIONAL DATA

We took the spectra of the 15 stellar photometric solar analogues given in Table 2 (printed in bold) using the 2-m Zeiss-2000 reflector of the Terskol Observatory of the International Center of Astronomical and Medico-Ecological Research in the northern Caucasus. In the late 1990s, the telescope was equipped with a modern echelle spectrometer [23] mounted at the stationary Coudé focus of the 2-m telescope.

The spectra have a resolution of $R = 45\,000$ and were recorded on a 1242×1152 Wright Instrument CCD. One special feature of the spectrometer is that, with this resolution and CCD size, it enables simultaneous recording over a wide wavelength interval from 3500 to 10 000 Å. This is of fundamental importance if we wish to determine the abundances of the largest possible set of elements. The signal-to-noise ratio is 150–200 over most of the spectrum (except for the blue). We observed most of the stars in July–August 1998. We supplemented the initial sample with two more solar-type stars—HD 213575 and HD 225239, which were identified as solar analogues by Glushneva *et al.* [3] and Kharitonov and Mironov [22] (Table 2). We took the spectra of these objects with the same instrument in September and October 1999, respectively.

We analyzed the spectra using a version of the DECH package operating under Windows [24] (DECH20T). We used this program to transform the spectra into one-dimensional form by performing all the necessary reduction of the echelle images. We cleaned the arrays of cosmic rays and normalized them. The wavelength scale was calibrated using spectra of solar light scattered in the Earth's atmosphere, which we exposed every day at dusk. We fully reduced the interval from 4000 to 9000 Å (from the blue to the near infrared) for all the spectra. Figure 1 illustrates fragments of the spectra of three stars.

4. FUNDAMENTAL PARAMETERS OF THE STARS

4.1. Effective Temperatures and Surface Gravities

We calculated the effective temperatures of all the stars from published photometric indices using the calibrations of Alonso *et al.* [25] based on the infrared-flux method. We derived the surface gravities from the HIPPARCOS [26] parallaxes. The errors in the resulting $T_{\rm eff}$ values do not exceed 100 K, and those in $\log g$ are about 0.1–0.2 dex. These results agree with those obtained by other authors. Columns 2 and 3 and 5 and 6 of Table 3 give the effective temperatures and surface gravities for the program stars calculated by us and taken from the catalog of Cayrel de Strobel *et al.* [27]. See our earlier paper [28] for a more detailed description of the methods used to determine these atmospheric parameters.

Table 3 gives no published data for HD 4915, HD 197076, HD 213575, and HD 222143. This reflects the fact that the fundamental parameters of these stars have not been determined with high accuracy. We note the large discrepancy in the measured temperatures of HD 225239, for which the previous value was taken from a comparatively old paper published in 1982 [29].

4.2. Microturbulence Velocity

We determined the microturbulence velocities, ξ_t, for all 15 stars from atomic and ionic lines (EW $<$ 100 mÅ) of iron-group elements by requiring that the abundances be independent of the line equivalent widths. To minimize the errors, we used elements with more than ten lines. Table 4 lists the ξ_t values for five stars based on five groups of spectral lines. The accuracy of this parameter is 0.2 km/s.

Subsequently, in accordance with our results, we assumed that the microturbulence velocity was 1.0 km/s for all the stars except for HD 4915, whose elemental abundances we calculated using $\xi_t = 0.8$ km/s.

4.3. Iron Abundances

The iron abundance is one of the fundamental parameters of a stellar atmosphere. We determined the Fe abundance from the equivalent widths of lines of ionized iron using the WIDTH6 program and the LTE model atmospheres of Kurucz [30]. We gave preference to results based on ion lines, since they represent the dominant stage (rather than neutral atoms) in the atmospheres of solar-type stars. We adopted the gf factors from the VALD database [31]. The number of measured FeII lines varied from 5 to 40 for various stars. The accuracies of the derived [Fe/H] values for individual stars are better than 0.10 dex. We list the [Fe/H] values calculated by us and adopted from [27] in the fourth and seventh columns of Table 3, respectively. In this table, the stars are arranged in order of decreasing metallicity and are subdivided into three groups (see Section 6). The parameters of all the stars except for HD 10307 and HD 222143 coincide within the errors in [Fe/H].

Table 3. Fundamental atmospheric parameters calculated here and taken from the catalog of metallicties [27] and the ages, masses, and radii of the stars

HD	This paper			Metallicity catalog			Age, 10^9 yr	Mass, $M_\odot$	Radius, $R_\odot$
	T_{eff}, K	$\log g$	[Fe/H]	T_{eff}, K	$\log g$	[Fe/H]			
1	2	3	4	5	6	7	8	9	10
159 222	5805	4.39	0.13	5845	4.28	0.09	3 [32]	1.07	1.35
186 408	5740	4.24	0.10	5800	4.26	0.06	6.61 [16]	0.99	1.24
222 143	5720	4.41	0.10	–	–	–	–	1.03	1.30
34 411	5800	4.20	0.08	5875	4.18	0.03	7.21 [33]	1.05	1.32
10 307	5815	4.32	0.05	5776	4.13	−0.05	5.90 [34]	1.06	1.34
141 004	5870	4.18	0.05	5864	4.09	−0.03	8.162 [35]	1.08	1.36
186 427	5700	4.34	0.05	5760	4.40	0.06	6.61 [16]	0.97	1.22
213 575	5630	4.15	0.05	–	–	–	10.826 [35]	0.98	1.23
146 233	5710	4.37	−0.01	5786	4.36	0.01	6.0 [21]	1.00	1.25
197 076	5810	4.46	−0.05	–	–	–	–	1.05	1.32
187 923	5700	4.08	−0.12	5729	4.01	−0.17	9.1 [32]	1.05	1.32
4307	5780	3.98	−0.17	5809	4.06	−0.23	6.11 [33]	1.09	1.38
4915	5660	4.59	−0.24	–	–	–	–	0.83	1.03
133 002	5610	3.45	−0.38	–	–	–	2.459 [35]	1.53	1.64
225 239	5650	3.79	−0.39	5478	3.8	−0.50	12.77 [33]	1.14	1.44

4.4. Ages, Masses, and Radii

The eighth column of Table 3 gives the ages of the stars compiled from various published sources (references are given next to the ages). The ages for different stars differ appreciably. The following columns give the masses and radii. We estimated the masses by fitting evolutionary tracks in our previous paper [36] and derived the radii from empirical mass–radius relations derived for main-sequence eclipsing binary components [37]. It is obvious from Table 3 that these stars are similar to the Sun in terms of all the above parameters.

5. ESTIMATED ACCURACY OF THE DERIVED ELEMENTAL ABUNDANCES

We used 16 Cyg B (HD 186427) to investigate the effect of the errors in a star's parameters on the accuracy of the derived LTE abundances. As is noted above, the errors in the temperatures, surface gravities, and microturbulence velocities do not exceed 100 K, 0.2 dex, and 0.3 km/s, respectively. We used these uncertainties to estimate upper limits for the errors in the derived elemental abundances.

As a result, we calculated for each atom and ion the abundance differences

$$\Delta = (star)_r - (star)_v,$$

where $(star)_r$ is the abundance derived from the observed parameters $T_{\rm eff} = 5700$ K, $\log g = 4.34$ dex, and $\xi_t = 1.0$ km/s and $(star)_v$ is the abundance

Table 4. Estimated microturbulence velocities (in km/s) for five stars based on five groups of atomic and ionic lines

	HD 34 411	HD 141 004	HD 146 233	HD 186 427	HD 187 923
FeI	1.0	1.0	0.8	1.0	1.0
FeII	1.2	1.2	1.2	1.2	1.2
NiI	1.0	1.0	1.0	1.0	1.0
ScII	1.0	1.0	0.8	1.2	1.2
TiI	0.8	1.2	1.0	1.2	1.2

Table 5. Effect of errors in the atmospheric parameters on the abundances derived for 16 Cyg B

Element	$\log\varepsilon$ (Sun)	$\log\varepsilon$ (16 Cyg B)	Δ_T	Δ_g	Δ_ξ	Δ_{EW}	N	σ_{el}
Li I	−10.52	−10.82	0.09	0.00	−0.01	–	1	0.10*
C I	−3.16	−3.11	0.08	−0.06	−0.01	0.10	10	0.11
N I	−3.73	−3.74	0.09	−0.07	0.00	0.09	5	0.11
O I	−2.92	−3.03	0.09	−0.06	−0.01	0.02	5	0.14
Na I	−5.65	−5.56	−0.06	0.03	−0.04	0.03	7	0.08
Mg I	−3.99	−4.38	−0.07	0.04	−0.04	0.04	6	0.10
Al I	−5.68	−5.49	−0.04	0.02	−0.01	0.08	6	0.09
Si I	−4.37	−4.22	−0.01	0.00	−0.02	0.02	22	0.03
S I	−4.46	−4.14	0.06	−0.06	−0.01	0.04	8	0.09
K I	−6.46	−6.42	−0.11	0.06	−0.09	–	1	0.10*
Ca I	−5.65	−5.62	−0.08	0.06	−0.06	0.03	33	0.12
Ca II	–	−5.29	0.07	−0.05	−0.03	0.17	4	0.19
Sc I	−8.80	−8.84	−0.10	0.01	−0.02	0.10	6	0.14
Sc II	−8.72	−8.62	0.00	−0.07	−0.06	0.03	21	0.09
Ti I	−7.00	−7.00	−0.10	0.01	−0.05	0.01	64	0.11
Ti II	−6.96	−6.82	−0.01	−0.06	−0.10	0.02	34	0.12
V I	−7.96	−8.01	−0.11	0.01	−0.02	0.02	26	0.11
V II	−7.02	−7.48	0.00	−0.09	−0.05	0.12	5	0.16
Cr I	−6.24	−6.19	−0.08	0.03	−0.06	0.02	43	0.11
Cr II	−6.24	−6.05	0.03	−0.08	−0.08	0.03	12	0.12
Mn I	−6.46	−6.45	−0.09	0.03	−0.08	0.02	28	0.12
Fe I	−4.39	−4.32	−0.06	0.02	−0.07	0.01	376	0.09
Fe II	−4.49	−4.44	0.03	−0.08	−0.09	0.02	36	0.12
Co I	−6.96	−6.98	−0.06	0.00	−0.03	0.03	14	0.07
Ni I	−5.68	−5.61	−0.05	0.01	−0.07	0.01	116	0.09
Cu I	−7.60	−7.27	−0.08	0.03	−0.14	0.18	5	0.24
Zn I	−7.39	−7.22	−0.01	−0.02	−0.13	0.08	4	0.15
Sr II	−9.20	−9.22	−0.02	−0.02	−0.03	0.13	3	0.14
Y I	–	−9.41	−0.09	0.00	−0.01	0.16	2	0.13
Y II	−9.69	−9.62	−0.01	−0.08	−0.09	0.05	11	0.13
Zr I	−9.40	−9.39	−0.12	0.00	0.00	0.11	2	0.16
Zr II	−9.15	−9.27	−0.01	−0.08	−0.04	0.07	11	0.11
Mo I	−9.76	−9.33	−0.11	0.00	−0.03	0.02	2	0.12
Ru I	−8.34	−8.55	−0.11	0.00	−0.03	0.02	2	0.12
Ba II	−9.55	−9.61	−0.02	−0.04	−0.13	0.03	5	0.14
La II	−10.46	−10.31	−0.02	−0.08	−0.10	0.10	7	0.16
Ce II	−10.37	−10.44	−0.02	−0.09	−0.03	0.03	13	0.10
Pr II	−11.00	−11.13	−0.02	−0.08	−0.01	0.08	4	0.12
Nd II	−10.43	−10.23	−0.02	−0.08	−0.03	0.08	12	0.12
Sm II	−10.58	−10.60	−0.02	−0.09	−0.02	0.07	7	0.12
Eu II	−10.34	−10.93	−0.01	−0.09	0.00	0.24	3	0.26

* The errors σ_{el} for Li I and K I were taken from [28] and [36], respectively.

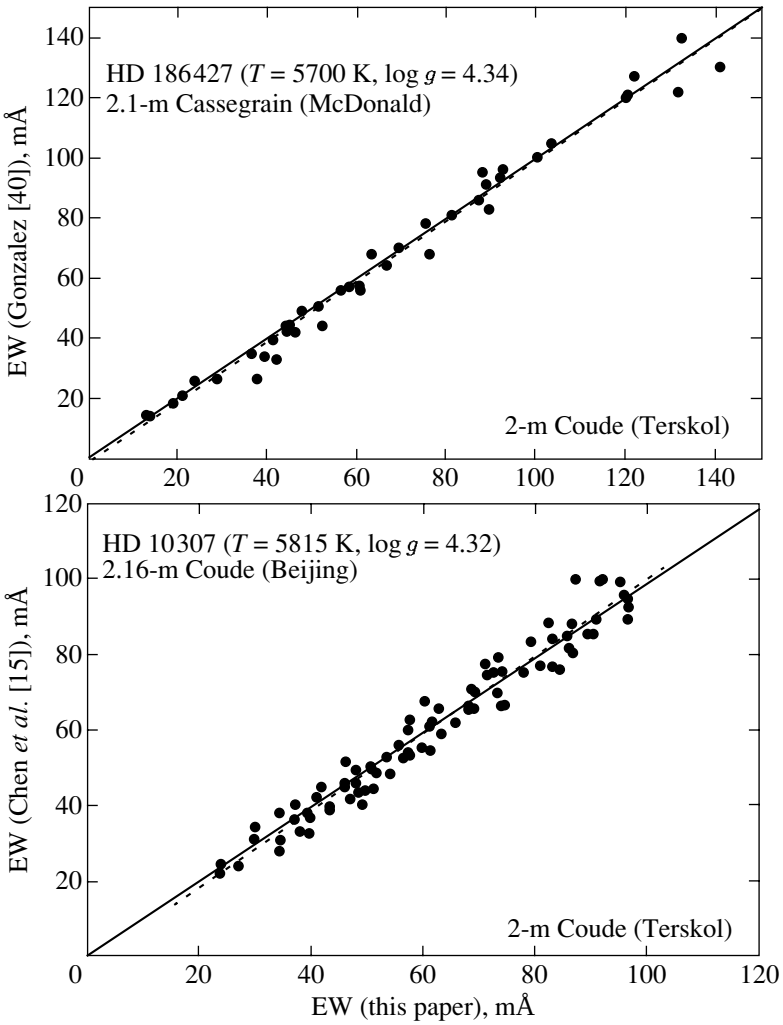

Fig. 2. Comparison of the line equivalent widths for HD 186427 and HD 10307 measured by us and published by Gonzalez [40] and Chen *et al.* [15].

derived using the modified parameters $T_{\rm eff} = 5600$ K, $\log g = 4.14$ dex, and $\xi_t = 1.3$ km/s. The results of these calculations are listed in the fourth, fifth, and sixth columns of Table 5, which give the uncertainties in the derived abundances in dex for atmospheric-parameter changes of $\Delta T = -100$ K, $\Delta \log g = -0.2$ dex, and $\Delta\xi_t = +0.3$ km/s. The third column lists the logarithms of the elemental abundances derived for 16 Cyg B. For comparison, the second column lists the corresponding abundances for the Sun, which we determined using the atlas [39] and the same set of lines and atomic data as for the 15 program stars.

We used these differences to estimate the abundance errors, σ_{el} (last column in Table 5), which we calculated using the formula

$$\sigma_{el} = \sqrt{\Delta_T^2 + \Delta_g^2 + \Delta_\xi^2 + \Delta_{\rm EW}^2}\,.$$

In addition to the uncertainties noted above, this takes into account the effect of the equivalent-width error ($\Delta_{\rm EW}$), which we assumed to be equal to the standard error of the mean abundance based on all the N measured lines.

Analysis of these data (Table 5) shows that the total abundance error is 0.10–0.15 dex for the overwhelming majority of elements.

6. ELEMENTAL ABUNDANCES

6.1. Calculations of the Chemical Composition

In this section, we analyze the elemental abundances in the atmospheres of the stars studied.

We calculated the elemental abundances from the measured equivalent widths of the lines of neutral and singly ionized atoms. We measured the equivalent widths of at least 400 lines at wavelengths of 4000–9000 Å in the spectrum of each star, the twilight-sky

Table 6. Elemental abundances in the solar analogues with [Fe/H] > 0.05 dex

Element	HD 159 222	HD 186 408	HD 222 143	HD 34 411
Li	1.00*	0.05*	0.92*	0.99*
C	0.15	0.07	0.04	−0.04
N	0.10	−0.06	0.30	−0.14
O	0.16	0.13	0.12	0.09
Na	0.20	0.16	0.03	0.17
Mg	0.24	0.18	0.03	0.12
Al	0.14	0.14	0.09	0.11
Si	0.25	0.19	0.14	0.14
S	0.28	0.11	0.03	0.07
K	0.05*	0.01*	0.00*	−0.04*
Ca	0.24	0.18	0.19	0.15
Sc	0.17	0.17	0.11	0.11
Ti	0.03	0.08	−0.05	−0.03
V	0.02	0.02	−0.03	0.05
Cr	0.12	0.11	0.06	0.02
Mn	0.11	0.05	−0.08	0.05
Fe	0.13	0.10	0.10	0.08
Co	0.10	0.00	−0.12	−0.07
Ni	0.13	0.11	0.02	0.04
Cu	0.23	0.16	−0.09	0.08
Zn	0.22	0.23	0.20	0.06
Sr	0.09	0.05	0.13	0.02
Y	0.27	0.11	0.12	0.02
Zr	0.14	0.08	0.05	−0.02
Mo	0.29	0.12	0.18	–
Ru	0.14	–	0.18	–
Ba	0.19	−0.01	0.19	0.00
La	0.09	0.04	0.12	−0.05
Ce	0.13	−0.05	0.06	−0.04
Pr	−0.10	−0.14	−0.11	−0.02
Nd	0.02	0.15	0.27	0.05
Sm	−0.02	−0.02	−0.03	−0.03
Eu	0.16	0.01	0.10	−0.02

* The lithium and potassium abundances were taken from [28] and [36], respectively.

spectra, and the spectra of the Solar Flux Atlas [39] and more than 1200 lines of various atoms and ions in the spectrum of 16 Cyg. The large number of lines accessible to analysis enabled us to discard the lines yielding the largest deviations from the mean due to uncertain atomic data, blending, and other factors.

Figure 2 compares the equivalent widths measured in this study and published previously. We can see that the accuracy of our measurements matches that of the data of other authors.

We calculated the elemental abundances using the WIDTH program and the LTE models of Kurucz [30]. We adopted the atomic parameters (gf factors and excitation energies) from the VALD database [31]. The accuracies of the elemental abundances are discussed in the previous section and listed in Table 5 (for 16 Cyg B). In this table, the atomic and ionic abundances that have not been used to analyze the chemical composition of the stars under study because of the lower accuracy are highlighted by italics.

The VALD database is currently the most complete compilation of atomic data, making it possible to calculate elemental abundances based on virtually all the identified and measured spectral lines. However, the oscillator strengths for some of the data may have been subject to substantial errors and biases. To reduce the effect of these errors and biases, we calculated the differential abundances relative to the corresponding "solar" values, which we derived from the equivalent widths measured from the Solar Flux Atlas using the same atomic parameters (and the solar model atmospheres from the same grid of models) as for the 15 program stars. Column 2 of Table 5 lists the abundances derived in this way using the data of [39].

The differential abundances of 33 elements relative to the corresponding solar abundances derived in this study using the "line minus line" method are listed in Tables 6–8 and are shown in Figs. 3–6. In some of the figures, the arrows with a value alongside indicate the lithium abundances which differ by an order of magnitude from the solar value in some of the stars.

Our homogeneous sample of solar analogues based on photometric color indices breaks up into three groups: six stars show abundances close to or coinciding with the corresponding solar abundances within the errors, while four and five stars, respectively, show over- and underabundances of the elements considered.

We subdivided the 15 stars into three tables according to their metallicities. Tables 6, 7, and 8 give the abundances in the four stars with [Fe/H] > 0.05 dex, the six stars with iron abundances from −0.05 to +0.05 dex, and the five metal-poor stars ([Fe/H] < −0.10), respectively.

Table 7. Elemental abundances in the solar analogues with $-0.05 < [Fe/H] < 0.05$ dex

Element	HD 10 307	HD 141 004	HD 186 427	HD 213 575	HD 146 233	HD 197 076
Li	0.89*	0.89*	−0.39*	–	0.56*	1.17*
C	−0.04	0.05	−0.03	−0.02	−0.06	−0.24
N	−0.02	−0.16	0.06	−0.01	0.04	−0.24
O	0.10	0.01	−0.05	0.17	0.04	−0.07
Na	0.10	0.07	0.11	0.02	0.04	−0.14
Mg	0.06	0.05	0.14	0.30	0.05	−0.11
Al	0.06	0.09	0.16	0.12	0.06	−0.12
Si	0.07	0.07	0.15	0.08	0.06	−0.02
S	0.07	−0.04	0.15	−0.02	0.11	−0.16
K	0.08*	0.04*	0.02*	−0.09*	−0.04*	−0.09*
Ca	0.09	0.08	0.03	0.09	0.11	0.01
Sc	0.13	0.14	−0.05	0.07	0.04	−0.10
Ti	−0.07	−0.04	0.13	0.11	0.04	−0.07
V	−0.09	−0.10	−0.05	−0.12	−0.07	−0.11
Cr	0.00	−0.01	0.05	−0.20	−0.02	−0.06
Mn	0.03	−0.02	0.01	−0.20	0.02	−0.27
Fe	0.05	0.05	0.05	0.05	−0.01	−0.05
Co	−0.01	−0.02	−0.02	−0.07	−0.03	−0.17
Ni	0.03	0.01	0.07	−0.16	−0.02	−0.15
Cu	−0.06	0.11	0.17	0.13	−0.02	−0.31
Zn	0.18	0.08	0.08	0.21	0.06	−0.18
Sr	0.17	0.13	−0.02	−0.12	0.10	−0.03
Y	0.12	−0.05	0.18	−0.15	0.09	−0.14
Zr	0.02	−0.04	0.01	−0.17	−0.06	−0.10
Mo	0.28	0.11	0.11	−0.20	–	−0.03
Ru	−0.24	–	−0.21	−0.35:	−0.06	−0.04
Ba	−0.03	0.10	−0.01	−0.06	0.04	0.12
La	0.05	0.06	0.02	0.00	0.02	−0.07
Ce	−0.03	0.04	−0.07	−0.27	0.03	0.07
Pr	−0.10	−0.10	−0.08	−0.02	−0.12	−0.20
Nd	−0.02	−0.06	0.18	0.04	0.15	0.14
Sm	−0.10	−0.19	0.01	−0.10	−0.05	−0.14
Eu	0.00	−0.04	0.06	−0.10	−0.04	0.02

* The lithium and potassium abundances were taken from [28] and [36], respectively.

Table 8. Elemental abundances in the solar analogues with [Fe/H] < −0.10 dex

Element	HD 187 923	HD 4307	HD 4915	HD 133 002	HD 225 239
Li	0.00*	1.32*	0.03*	–	–
C	−0.16	−0.28	−0.31	−0.60	−0.53
N	−0.05	−0.42	−0.16	−0.09	−0.46
O	0.03	−0.06	−0.23	−0.35	−0.30
Na	−0.04	−0.25	−0.26	−0.12	−0.42
Mg	0.11	−0.08	−0.14	−0.16	−0.28
Al	0.11	−0.19	−0.24	−0.22	−0.42
Si	0.06	−0.15	−0.13	−0.25	−0.30
S	0.08	−0.33	−0.18	−0.41	−0.47
K	−0.02*	−0.13*	−0.30*	−0.38*	−0.36*
Ca	0.09	−0.08	−0.17	−0.23	−0.28
Sc	0.03	−0.06	−0.14	−0.19	−0.27
Ti	−0.13	−0.13	−0.23	−0.19	−0.43
V	−0.15	−0.23	−0.28	−0.32	−0.43
Cr	−0.10	−0.29	−0.29	−0.31	−0.38
Mn	−0.15	−0.31	−0.42	−0.43	−0.63
Fe	−0.12	−0.17	−0.24	−0.38	−0.31
Co	−0.13	−0.21	−0.29	−0.31	−0.54
Ni	−0.13	−0.25	−0.33	−0.37	−0.49
Cu	−0.07	−0.31	−0.28	−0.36	−0.47
Zn	0.05	−0.10	−0.29	−0.12	−0.21
Sr	−0.09	−0.26	−0.33	−0.10	−0.25
Y	−0.10	−0.29	−0.24	−0.46	−0.55
Zr	−0.04	−0.36	−0.37	−0.46	−0.44
Mo	–	−0.18	−0.14	−0.43	−0.90:
Ru	–	–	−0.08	−0.66	–
Ba	−0.05	−0.08	−0.12	−0.37	−0.32
La	−0.05	−0.25	−0.16	−0.38	−0.53
Ce	−0.07	−0.35	−0.22	−0.13	−0.47
Pr	–	−0.22	−0.10	−0.39	−0.41
Nd	−0.02	−0.30	−0.11	−0.28	−0.26
Sm	−0.08	−0.33	−0.18	−0.46	−0.50
Eu	0.08	−0.14	−0.09	−0.14	−0.48

* The lithium and potassium abundances were taken from [28] and [36], respectively.

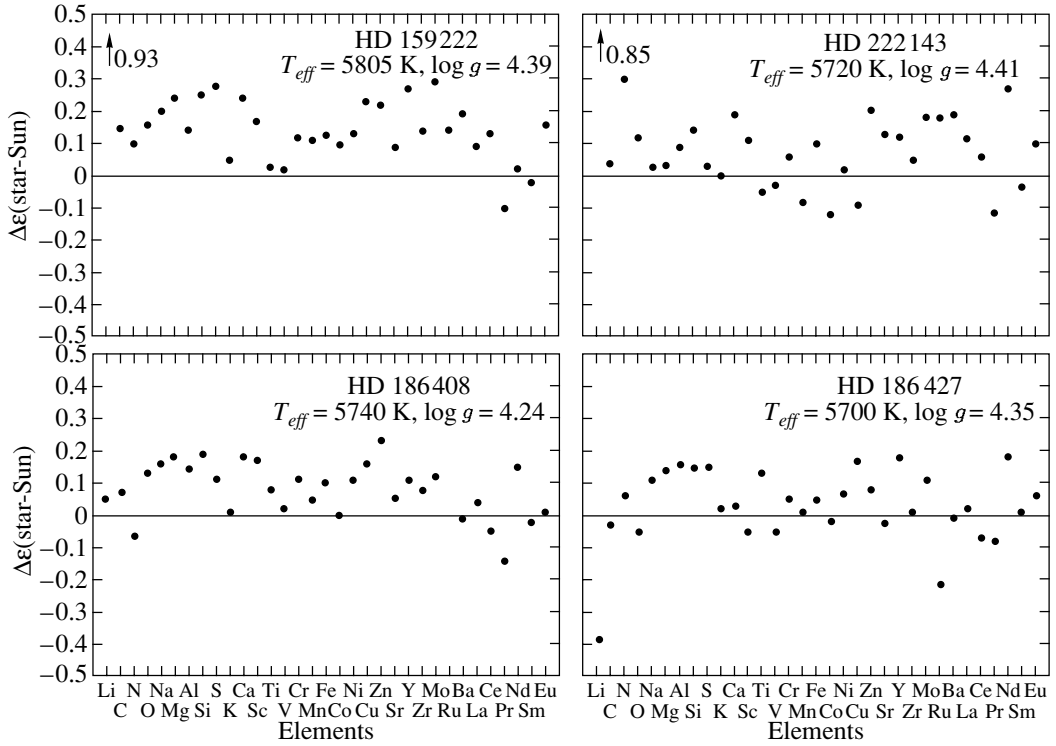

Fig. 3. Chemical composition of four stars with supersolar abundances: HD 159222, HD 222143, and 16 Cyg A and B. These and the following plots show the parameters of the stellar atmospheres; the horizontal line at $\Delta\varepsilon = 0$ corresponds to the solar abundances adopted in this study.

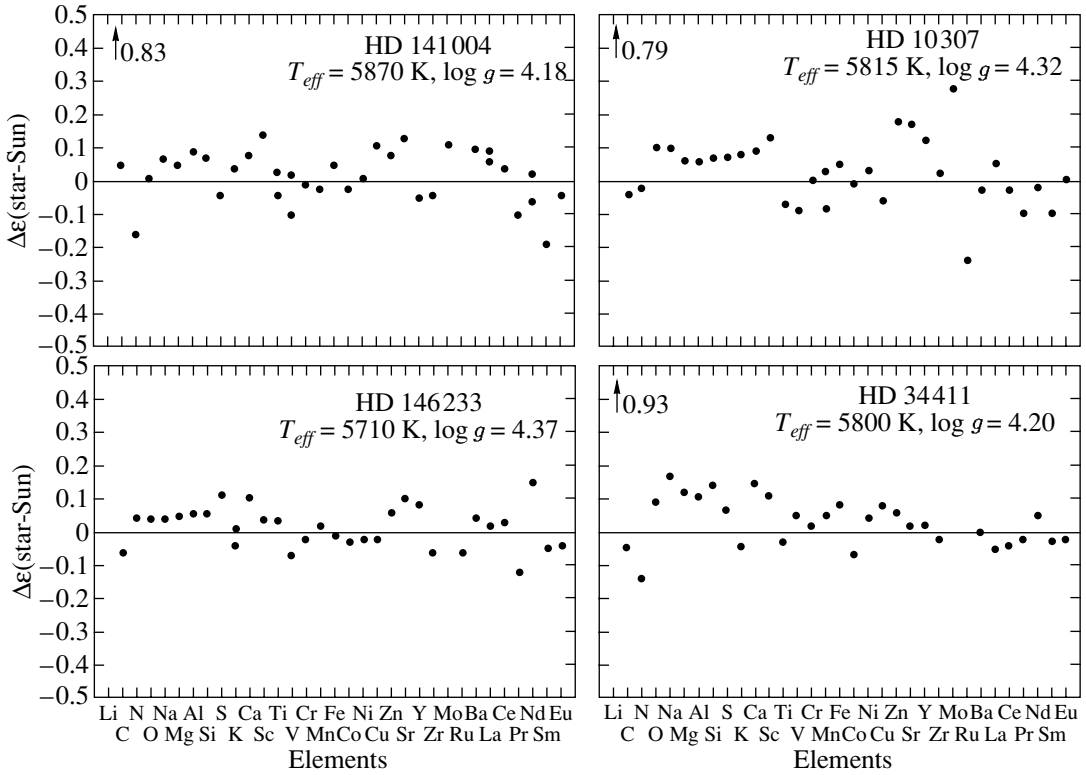

Fig. 4. Chemical composition of four solar-metallicity stars: HD 141004, HD 10307, HD 146233, and HD 34411.

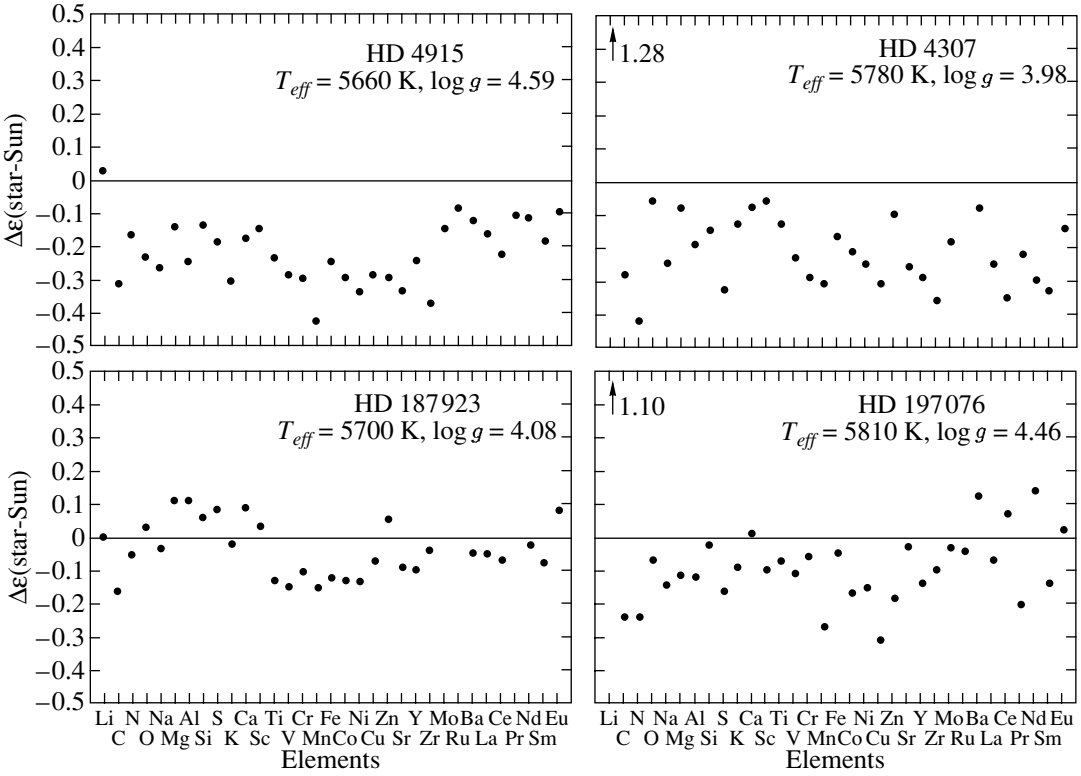

Fig. 5. Chemical composition of four stars with subsolar metallicities: HD 4915, HD 4307, HD 187923, and HD 197076.

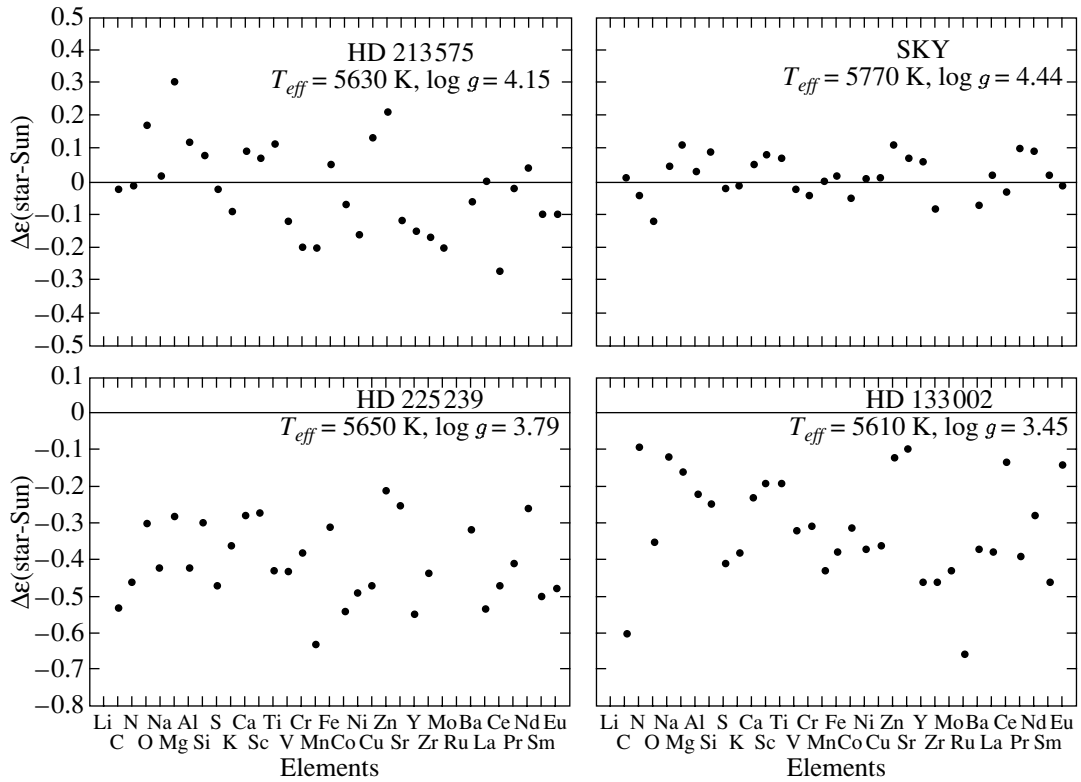

Fig. 6. Chemical composition of three stars with various metallicities (HD 213575, HD 225239, HD 133002), with the same plot for solar light reflected in the Earth's atmosphere (SKY) given for comparison.

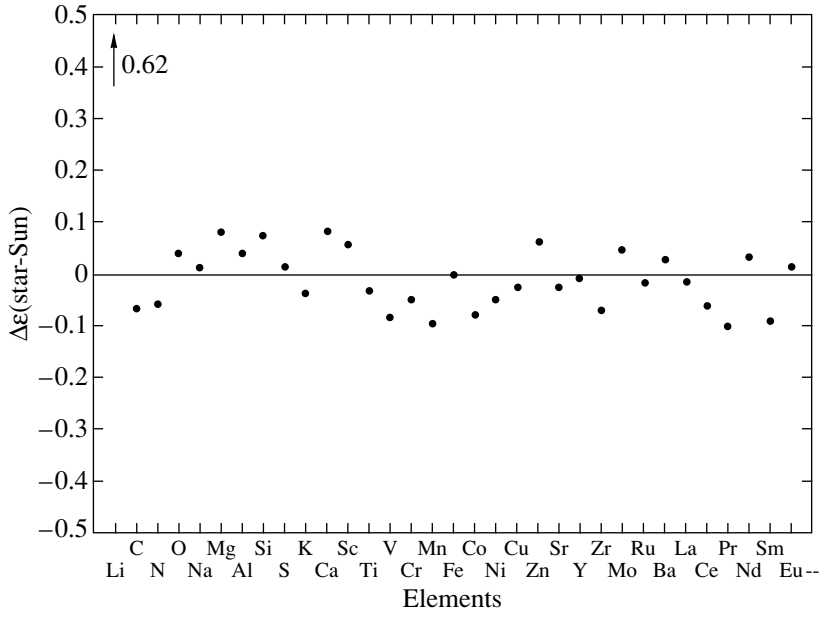

Fig. 7. Chemical composition of a "mean star" obtained by averaging over 13 of the stars in the sample.

We could not determine the abundances of some heavy elements (molybdenum and ruthenium) in several stars in whose spectra each of these elements was represented by only one extremely weak or unmeasurable line. The tables and figures give the non-LTE lithium and potassium abundances, which we calculated earlier using synthetic spectra [28, 36].

The figures shown here demonstrate a certain "wave-like" pattern. The abundances of "neighboring" elements group together, forming specific sequences: Ca–Mn, Sr–Ru, Ba–Sm ("decreasing"); Mn–Zn ("increasing"); and the group of light elements (O, Na, Mg, Al, Si) overabundant relative to other elements. The overabundances of sodium, magnesium, and aluminum in solar-type stars were already pointed out by Edvardsson *et al.* [13]; however, the new observational data of Tomkin *et al.* [38] did not confirm the overabundances of these elements. Figure 7 shows the distribution of abundances for a "mean star" with atmospheric abundances equal to the mean abundance for 13 of the stars analyzed here (we excluded two stars that are obviously metal deficient from the averaging); i.e., $\Delta\varepsilon = \overline{\varepsilon(13stars)} - \varepsilon(\mathrm{Sun})$). The "sequences" of elements noted above are present, although the resulting mean abundances lie within ±0.10 dex. These sequences may reflect real differences in the distribution of elements in the atmospheres of the stars studied compared to the corresponding abundances in the solar atmosphere (the Sun may exhibit peculiarities in the abundances of certain groups of elements); alternatively, the effects noted above may be due to some effects that have not been properly taken into account by the analysis.

A correct analysis of the behavior of the distributions of various elements in solar-type stars requires a more representative stellar sample, and we defer such an analysis to another paper.

6.2. Comparison with the Results of Other Authors

The chemical compositions of only the brightest of the 15 sample stars have been investigated in detail, i.e., based on more than five elements (the number of elements with abundance estimates and the corresponding references are given in parentheses): HD 4307 (10 [13], 11 [18]), 41 And (= HD 10307; 7 [12], 10 [13], 13 [15]), λ Aur (= HD 34411; 7 [12], 10 [13], 13 [15]), λ Ser (= HD 141004; 10 [13]), 18 Sco (= HD 146233; 24 [21]), 16 Cyg A (= HD 186408; 8 [20], 15 [40], 11 [41], 26 [16]), 16 Cyg B (= HD 186427; 8 [20], 15 [40], 17 [17], 11 [41]), and HD 225239 (26 [16]). Abundances of single elements (Fe, O, Li, Eu, Sc, Mn, Be, etc.) have been published in a number of studies, but we do not list them here, since our aim is to analyze the full chemical compositions of solar analogues.

The main difference between our results and those obtained by the above authors is that we determined the abundances of up to 33 elements (from lithium to europium), for many of them for the first time. Second, we used more lines than most previous studies, in particular, infrared lines, which were of crucial importance in some cases (e.g., for nitrogen, sulfur, carbon, etc.). Using Table 9 and Fig. 8a, let us compare our

Table 9. Number of lines of 20 elements measured in the spectrum of HD 186 408 by us and Gonzalez [40]

Number of lines	Li	C	O	Na	Mg	Al	Si	S	K	Ca	Sc	Ti	V	Cr	Mn	FeI	FeII	Co	Ni	Ba
This paper	1	8	5	6	9	6	24	2	1	28	17	23	22	18	14	181	13	15	53	5
Gonzalez [40]	1	1	3	–	1	2	1	1	–	3	2	1	–	2	–	29	3	2	1	1

Table 10. Abundance differences $\delta\varepsilon = \varepsilon(\text{this paper}) - \varepsilon([18])$ and $\delta\varepsilon = \varepsilon(\text{this paper}) - \varepsilon([16])$ in HD 4307 and HD 225 239 for 24 elements common with those analyzed in this paper

Star	C	O	Na	Mg	Al	Si	S	Ca	Sc	Ti	V	Cr
HD 4307	–	–	0.11	–	–	0.06	–	0.14	0.12	0.06	0.05	−0.09
HD 225 239	−0.33	−0.2	0.02	0.14	−0.07	0.14	−0.48	0.20	0.17	0.05	0.12	0.16
Star compared	Mn	Fe	Co	Ni	Cu	Zn	Sr	Y	Ba	Ce	Nd	Eu
HD 4307	–	0.09	−0.02	0.04	–	–	–	–	–	–	−0.12	–
HD 225 239	0.03	0.22	−0.02	0.05	0.13	0.20	0.28	0.08	0.42	0.07	0.20	−0.09

data and those used by Gonzalez [40] for the analysis of 16 Cyg A. Table 9 indicates the number of lines whose equivalent widths were measured and used to calculate the abundances of the corresponding elements.

The accuracy of the derived abundances also depends on the quality of the spectra used. The observational data used in earlier analyses of the chemical compositions of solar analogues were very similar to our own. The stars were observed using 2-m-class reflectors (of the McDonald Observatory, European Southern Observatory, Beijing Observatory, and Okayama Astrophysical Observatory). The spectral resolutions range from 40 000 to 100 000, and the signal-to-noise ratios, from 120 to 400, depending on the resolution and spectral region considered. Our observations (Section 3) had comparable characteristics. Most modern data (except those of Porto de Mello and da Silva [21] and Gonzalez [40]) have been obtained with Coudé spectrometers.

Table 10 gives the abundance differences relative to the Sun ($\Delta\varepsilon$) between our results and those of Thoren and Feltzing [18] and Reddy *et al.* [16] for HD 4307 and HD 225239. Figure 8 compares the distribution of abundances for HD 186427 and HD 146233. The various symbols show our own and previously published data. For 16 Cyg B, upper limits for the errors in the abundances are given for all elements (from Table 5). The abundances for most elements agree within the quoted errors. Appreciable discrepancies can be seen for the lightest (Li, C, N) and several heavy (Y, Ba, Sr) elements. These discrepancies are most likely due to the use of uncertain data (based on measurements of only one or two lines) in the earlier studies.

7. THE SIMILARITY OF PHOTOMETRIC ANALOGUES TO THE SUN

In this section, we attempt to answer the question posed by Friel *et al.* [20]: is it possible to find stars whose fundamental physical parameters are very close to the solar parameters among photometric solar analogues?

This was the motivation for our use of a homogeneous sample of stars whose various photometric indices are close to the solar color indices. We calculated the fundamental parameters of these objects either using published data or new high-dispersion spectra of these stars. We analyze the compliance of the parameters of the stars studied (Table 3) with the criteria proposed in Table 1. This procedure enables us to identify solar-twin candidates in our sample of solar analogues.

We summarize our results in Table 11, which groups the stars in accordance with various solar-analogue and solar-twin criteria.

Analysis of the fundamental parameters of the stars (T_{eff}, $\log g$, [Fe/H]) immediately reveals two objects that fail to meet the criteria for both solar twins and solar analogues—HD 133002 and HD 225239. The temperatures of these stars are 100 K or more lower than that of the Sun, the surface gravities are 0.5–1.0 dex lower than that of the Sun, and the metallicities differ by more than 0.3 dex from the corresponding solar values. The distribution of the elemental abundances (Fig. 8) shows that both stars

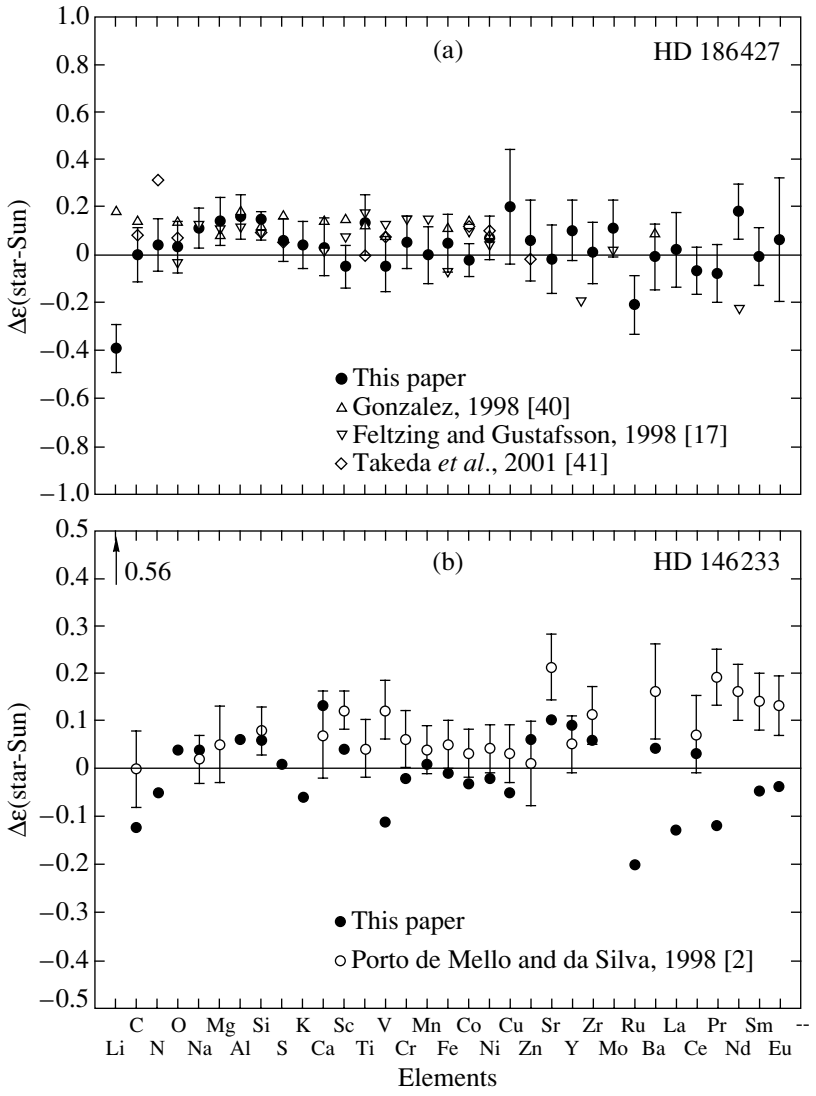

Fig. 8. Comparison of elemental abundances in the atmospheres of (a) HD 186427 and (b) HD 146233 with the results of other authors.

are metal-deficient. The masses and radii of these two objects likewise show that they cannot be considered solar analogues. Moreover, one of the stars is too young and the other too old compared to the Sun.

These stars proved to be accidental members of our sample, despite the fact that their color indices agree with those of the Sun (although the $B-V$ index of HD 133002 is the highest among those of the stars suggested by Kharitonov and Mironov [22]). The physical parameters of the two stars differ strongly from the corresponding solar parameters. It follows that photometric parameters alone are not sufficient for identifying full analogues of the Sun. The atmospheric parameters must also be determined using various methods for a sufficiently large number of stars (e.g., in her catalog of metallicities, Cayrel de Strobel *et al.* [27] lists the fundamental parameters of 3365 cool stars).

Thus, only 13 stars of the initial list of 15 objects meet some of the criteria (apart from chemical composition) for solar analogues. Imposing the additional criterion of chemical composition leaves only six stars (HD 10307, HD 34411, HD 141004, HD 146233, HD 187923, HD 213575) whose distributions of elemental abundances are close to that for the Sun.

The four stars HD 10307, HD 34411, HD 146233, and HD 186427 are genuine solar analogues according to both their fundamental parameters and chemical compositions. However, is there any solar twin among these stars? To answer this question, let us consider each star again based on the data given in Tables 3 and 1.

Table 11. HD numbers of stars selected as solar analogues or solar twins according to the criteria listed in the first column

Criterion	Analogue	Twin
By chemical composition	34 411, 186 427, 187 923, 213 575	10 307, 141 004, **146 233**
By metallicity	4307, 4915, 34 411, 159 222, 186 408 187 923, 222 143	10 307, 141 004, **146 233**, 186 427, 197 076 213 575
By mass	4307, 10 307, 141 004, 159 222, 186 408	34 411, **146 233**, 186 427, 187 923, 197 076 213 575, 222 143
By log g	4915, 10 307, 34 411, 141 004, 186 408 187923	**146 233**, 159 222, 186 427, 197 076, 22 143
By temperature	4915, 133 002, 141 004, **146 233**, 186 427 187 923, 213 575	4307, 10 307, 34 411, 159 222, 186 408 197 076, 222 143
By age	4307, 34 411, 186 408, 186 427	10 307, **146 233**
By Li abundance	**146 233**, 186 427	4915, 186 408, 187 923

HD 10307 and HD 34411 have temperatures, [Fe/H], chemical compositions, and masses that qualify them to be solar twins; however, their surface gravities (luminosities) and ages fall slightly short of the boundary for the solar-twin criteria we have adopted.

On the other hand, HD 146233 (18 Sco) has been considered to be a genuine solar-twin candidate for a number of years [2]. Virtually all the parameters of this star—luminosity, log g, metallicity, mass, and the abundances of essentially all elements—meet the criteria imposed for solar twins. In Table 11, where 18 Sco is printed in bold, it is immediately apparent that this star satisfies almost all criteria for a solar twin.

Almost all the parameters of HD 186427 (16 Cyg B) are also close to the corresponding solar parameters. However, it is immediately obvious from the chemical composition of this star (Fig. 8a) that the abundances of most elements lie above the line indicating the solar chemical composition. We therefore do not believe HD 186427 to be a likely solar twin.

We thus conclude that 18 Sco is the most likely full solar twin. It is interesting that it is the best chemical analogue among the 15 stars studied. The lower part of Fig. 8b shows the chemical composition of this star according to our data and those of Porto de Mello and da Silva [21] (the $\Delta\varepsilon$ values of [21] are shown with error bars).

Because the lithium abundance in the atmospheres of solar-type stars can vary over the star's lifetime on the main sequence and lithium is represented by only one line in the stellar spectra, we analyzed the abundances of this element in the photometric solar analogues in a separate paper [28]. The stars analyzed break up into two groups according to their lithium abundances: (1) stars with nearly solar lithium abundances and (2) stars with lithium abundances an order of magnitude higher than the solar value (Figs. 3–6). We called stars of the first group (HD 4915, HD 146233, HD 186408, HD 186427, and HD 187923) "lithium solar analogues." However, among these, only 18 Sco and 16 Cyg B proved to be genuine solar-twin candidates, although their lithium abundances differ somewhat from the solar lithium abundance. For example, lithium is overabundant in HD 146233 by 0.56 dex.

8. CONCLUSIONS

We have analyzed a sample of 15 photometric solar analogues selected based on similarity of their color indices to the solar color indices. The analysis used high-resolution spectra obtained with a Coudé spectrometer mounted on the 2-m telescope of the Terskol Observatory. We applied the model-atmospheres method to analyze the equivalent widths of the spectral lines for our own and previously published data to determine the main parameters of the stellar atmospheres ($T_{\rm eff}$, log g, and [Fe/H]) and to calculate the atmospheric chemical compositions of each star for more than 30 elements.

The accuracies of the derived parameters are comparable to those for results obtained with similar instruments using similar reduction and calculation

methods (100 K, 0.2 dex, about 0.10–0.15 dex, and 0.2 km/s for the temperature, $\log g$, elemental abundances, and ξ_t, respectively). The parameters of most of the stars are close to the corresponding solar parameters and in agreement with the results of other studies. However, the photometric solar analogues included two stars with clearly subsolar elemental abundances (metal-poor stars), which cannot be true solar analogues.

We calculated the LTE abundances for 33 elements from lithium to europium based on a large number of spectral lines (we were the first to perform such extensive chemical analyses for most of the stars in our list). Comparison of our abundances with those obtained for the same stars with other similar telescopes shows that our results agree well with those of other studies. The abundance distributions for various groups of elements exhibit a certain pattern. The sample stars break up into three groups according to the chemical compositions of their atmospheres: four stars have overabundances of metals, five have underabundances of metals, and only six photometric analogues of the Sun have solar chemical compositions.

Analysis of all the stars to determine how similar they are to the Sun in terms of various criteria and to search for a solar twin among them yielded the following results.

Two stars (HD 133002 and HD 225239) are not even solar analogues; they are clearly subgiants and have metal deficiency. Only four stars (HD 10307, HD 34411, HD 146233, and HD186427) meet all the criteria imposed on solar analogues. The last two stars have long been listed as solar analogues. In the end, HD 146233 proves to also be a solar twin. Our analysis confirms that nearly all the parameters of this star coincide with the corresponding solar parameters within the errors. This star is consequently a genuine solar twin.

ACKNOWLEDGMENTS

This work was supported by the Russian Foundation for Basic Research (project nos. 99-02-17488, 02-02-17174, and 02-02-17423), the Program for the Support of Leading Scientific Schools (grant no. NSh-1789.2003.2), and the Academy of Sciences of the Republic of Tatarstan. A.I. Galeev also acknowledges support from the Russian Foundation for Basic Research (grant MAS 01-02-06068). We are grateful to the staff of the Peak Terskol Observatory for offering us the possibility of performing successful observations and to V.V. Shimanskiĭ and N.A. Sakhibullin for useful discussions and multifaceted assistance when performing this work.

REFERENCES

1. D. R. Soderblom and J. L. King, in *Solar Analogues: Characteristics and Optimum Candidates* (Lowell Observatory, Flagstaff, Arizona, 1998), p. 41.
2. G. F. Porto de Mello and L. da Silva, Astrophys. J. **482**, L89 (1997).
3. I. N. Glushneva, V. I. Shenavrin, and I. A. Roshchina, Astron. Zh. **77**, 285 (2000) [Astron. Rep. **44**, 246 (2000)].
4. A. Altamore, C. Rossi, L. Rossi, and M. Villada de Arnedo, Astron. Astrophys. **234**, 332 (1990).
5. J. Fernley, H. Neckel, E. Solano, and W. Wamsteker, Astron. Astrophys. **311**, 245 (1996).
6. T. Farnham and D. Schleicher, in *Solar Analogues: Characteristics and Optimum Candidates* (Lowell Observatory, Flagstaff, Arizona, 1998), p. 137.
7. G. Cayrel de Strobel, Astron. Astrophys. Rev. **7**, 243 (1996).
8. G. Cayrel de Strobel and C. Bentolila, Astron. Astrophys. **211**, 324 (1989).
9. J. B. Laird, Astrophys. J. **289**, 556 (1985).
10. B. Barbuy and M. Erdelyi-Mendes, Astron. Astrophys. **214**, 239 (1989).
11. E. Nissen and B. Edvardsson, Astron. Astrophys. **261**, 255 (1992).
12. J. Tomkin, D. L. Lambert, and S. Balachandran, Astrophys. J. **290**, 289 (1985).
13. B. Edvardsson, J. Andersen, B. Gustafsson, *et al.*, Astron. Astrophys. **275**, 101 (1993).
14. E. Carretta, R. G. Gratton, and C. Sneden, Astron. Astrophys. **356**, 238 (2000).
15. Y. Q. Chen, E. Nissen, G. Zhao, *et al.*, Astron. Astrophys., Suppl. Ser. **141**, 491 (2000).
16. B. E. Reddy, J. Tomkin, D. L. Lambert, and C. Allende Prieto, Mon. Not. R. Astron. Soc. **340**, 304 (2002).
17. S. Feltzing and B. Gustafsson, Astron. Astrophys., Suppl. Ser. **129**, 237 (1998).
18. Thoren and S. Feltzing, Astron. Astrophys. **363**, 692 (2000).
19. E. J. Gaidos and G. Gonzalez, New Astron. **7**, 211 (2002).
20. E. Friel, G. Cayrel de Strobel, Y. Chmielewski, *et al.*, Astron. Astrophys. **274**, 825 (1993).
21. G. F. Porto de Mello and L. da Silva, in *Solar Analogues: Characteristics and Optimum Candidates* (Lowell Observatory, Flagstaff, Arizona, 1998), p. 129.
22. A. V. Kharitonov and A. V. Mironov, in *Solar Analogues: Characteristics and Optimum Candidates* (Lowell Observatory, Flagstaff, Arizona, 1998), p. 149.
23. F. A. Musaev, G. A. Galazutdinov, A. V. Sergeev, *et al.,* Kinemat. Fiz. Neb. Tel **13**, 282 (1999).
24. G. A. Galazutdinov, Preprint Spets. Astron. Obs. **92**, 1 (1992).
25. A. Alonso, S. Arribas, and C. Martinez-Roger, Astron. Astrophys. **313**, 873 (1996).
26. *The HIPPARCOS Catalogue,* ESA SP-1200, ESTEC, Nordwijk (1997).
27. G. Cayrel de Strobel, C. Soubiran, and N. Ralite, Astron. Astrophys. **373**, 159 (2001).

28. A. I. Galeev, I. F. Bikmaev, L. I. Mashonkina, *et al.,* Astron. Zh. **81** (2004, in press).
29. F. Spite and M. Spite, Astron. Astrophys. **115**, 357 (1982).
30. R. L. Kurucz, Atmospheric Models on CD-ROMs (1993).
31. F. Kupka, N. Piskunov, T. A. Ryabchikova, *et al.*, Astron. Astrophys., Suppl. Ser. **138**, 119 (1999).
32. K. Fuhrmann, Astron. Astrophys. **338**, 161 (1999).
33. H. M. Qiu, G. Zhao, and Z. W. Li, Astrophys. Space Sci. **277**, 565 (2001).
34. A. Ibukiyama and N. Arimoto, Astron. Astrophys. **394**, 927 (2002).
35. S. Feltzing, J. Holmberg, and J. R. Hurley, Astron. Astrophys. **377**, 911 (2001).
36. V. V. Shimanskiĭ, I. F. Bikmaev, A. I. Galeev, *et al.,* Astron. Zh. **80**, 816 (2003) [Astron. Rep. **47**, 750 (2003)].
37. S. Yu. Gorda and M. A. Svechnikov, Astron. Zh. **75**, 896 (1998).
38. J. Tomkin, B. Edvardsson, D. L. Lambert, and B. Gustafsson, Astron. Astrophys. **327**, 587 (1997).
39. R. L. Kurucz, I. Furenlid, J. Brault, and L. Testerman, *Solar Flux Atlas from 296 to 1300 nm* (KPNO, Tucson, 1984).
40. G. Gonzalez, Astron. Astrophys. **334**, 221 (1998).
41. Y. Takeda, B. Sato, E. Kambe, *et al.*, Publ. Astron. Soc. Jpn. **53**, 1211 (2001).

Translated by K. Maslennikov

Astronomy Reports, Vol. 48, No. 6, 2004, pp. 511–521. Translated from Astronomicheskiĭ Zhurnal, Vol. 81, No. 6, 2004, pp. 561–573.

The Atmospheric Lithium Abundances of Solar Analogues

A. I. Galeev[1, 2], I. F. Bikmaev[1], L. I. Mashonkina[1], F. A. Musaev[3], and G. A. Galazutdinov[3]

[1] *Kazan State University, Kremlevskaya str. 18, Kazan, Tatarstan, 420008 Russia*

[2] *Department of Physics, Kazan State Pedagogical University, Mezhlauk str. 1, Kazan, Tatarstan, 420021 Russia*

[3] *Special Astrophysical Observatory, Russian Academy of Sciences, Nizhniĭ Arkhyz, Karachaĭ-Cherkessian Republic, 369167 Russia*

Received October 13, 2003; in final form, January 9, 2004

Abstract—We have analyzed the lithium abundance in the atmospheres of 20 stars that are solar analogues based on high-resolution echelle spectra using model atmospheres in a non-LTE approach. In terms of their lithium abundances, the stars (which are located in a narrow range of temperatures of 5650–5900 K) can be divided into two groups: one with low lithium abundances, as in the solar atmosphere, and one with lithium abundances that are higher than the solar value by about 1 dex (with the accuracy of the lithium abundances being 0.15 dex). © *2004 MAIK "Nauka/Interperiodica"*.

1. INTRODUCTION

Lithium, the lightest metal, is unique among the various chemical elements, because its abundance in stellar atmospheres varies substantially during the course of a star's evolution. This is because the lithium is burned in thermonuclear reactions when the temperature is still relatively low (around 2.5×10^6 K). For this reason, the concentration of Li in stellar atmospheres can vary dramatically as a result of large-scale convection motions inside a star in various stages of its evolution. The light elements Be and B are similar to lithium in this way. For example, over the Sun's evolution, the lithium abundance in its atmosphere has become two orders of magnitude lower than the meteoritic Li abundance [1].

The study of lithium abundances in stars is further complicated by the fact that only the LiI 6708 resonance doublet is usually observed in stellar spectra, and these lines can be observed only in cool stars. Lithium abundances can provide clues to the nature of nucleosynthesis occurring in the stellar core and can be useful in modeling the structure and evolution of stars.

The lithium abundances in late-type stars have been considered in many studies over the last 20 years. The solar Li abundance is relatively low, even compared to other solarlike stars [2]. The lithium abundance is related to the abundances of the other light elements Be and B [3] and varies depending on a star's metallicity [4].

The Li abundances are different for different stellar populations and in disk objects of different ages, for example, in different clusters. This provides further evidence for the existence of a relationship between Li abundance and age. However, the accuracy of this correlation remains low, and its universality doubtful, mainly due to the large scatter of the Li abundances in the studied stars and difficulties in determining the ages of certain stellar groups.

The Li abundance is also correlated with rotation, which may be a key factor in the Li deficiency in cool stars. The isotope ratio ^{6}Li : ^{7}Li is a very important evolutionary parameter; attempts have been made to determine this ratio from high-resolution profiles of the Li resonance line in the spectra of bright stars, and it appears to be different from the ratio in the solar system.

Essentially all observational studies have used relationships between the Li abundance and the effective temperature (A(Li)–T_{eff}) such as that presented in Fig. 1, taken from the study of Pasquini *et al.* [5]. The flat portion near 6000 K is clearly visible; according to other studies, it extends toward higher temperatures, up to the "lithium gap" found for the Hyades. The lithium abundance decreases toward lower temperatures and reaches $A(\mathrm{Li}) = -1$ dex [6] in K dwarfs.

This dependence is observed for cool stars of various types: normal G–K dwarfs (see, for example, [4, 6]); subgiants [7, 8] and subdwarfs [9]; disk [10] and halo [11, 12] stars; young [13], intermediate [14], and old [15, 16] clusters; and stars with planets [17]. Deviations are observed only for unusual objects; for example, extremely low Li abundances have been measured for K supergiants [18]. On the contrary, the asymptotic giant branch contains lithium-enriched (super lithium-rich) stars [19]. A composite diagram for various types of stars is presented in [20].

1063-7729/04/4806-0511$26.00

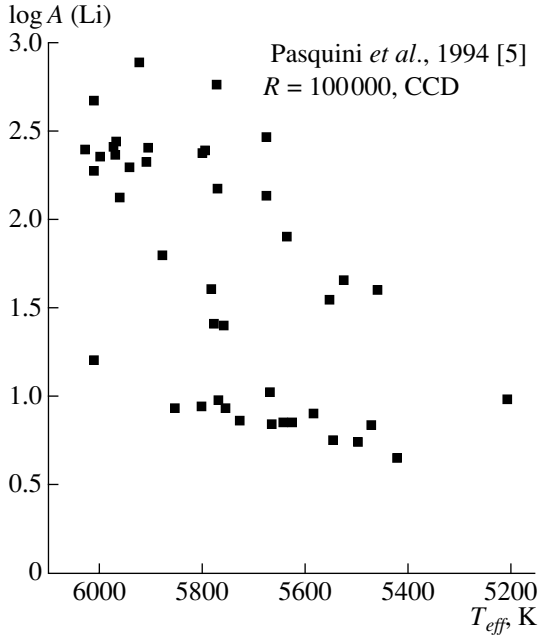

Fig. 1. Li abundance as a function of effective temperature for a sample of nearby solar-type stars (from the study of Pasquini *et al.* [5]).

In all studies, however, lithium in cool stars has been considered within a large temperature interval (at least 700 K). Here, we consider a sample of stars that occupy a small temperature interval, 5650–5900 K, which corresponds to the solar temperature. What is the behavior of the Li abundances within such a narrow temperature (and luminosity) interval? Does the distribution of the Li abundances in this interval agree with the $A(\mathrm{Li})$–T_{eff} diagrams plotted for other types of stars? Another problem is indicated in [5]: is the solar Li abundance typical for stars with masses, ages, and chemical compositions similar to those of the Sun? Here, we consider these problems for the group of photometric analogues of the Sun proposed by Kharitonov and Mironov [21]. We studied the chemical compositions of these stars in [22]. Since Be and B lines are in the UV and are inaccessible to our equipment, we do not consider the abundances of these elements here.

2. OBSERVATIONS AND REDUCTION

We observed 13 stellar analogues of the Sun in July–August, 1998, with the 2-m Zeiss-2000 Telescope of the Terskol Peak Observatory of the International Center of Astronomical and Medical-Ecological Research (North Caucasus). Spectra with a resolution of $R = 45\,000$ at wavelengths of 3500–10 000 Å were obtained with the Coudé echelle spectrograph [23] and WI 1242 × 1152-pixel CCD camera.

Table 1 presents basic information about the observations. The letter T followed by a number indicates the number of the observing night on this telescope. The next column contains a coded name for the spectrum (file) consisting of the night number, the number of the spectrum obtained on this night, and a letter s if the spectrum was combined from two spectra. The third column gives the HD numbers of the studied stars, and the following columns present the date, mid-exposure (Moscow time), and exposure for each spectrum.

All the spectra were processed in the standard way (transformation to one-dimensional vectors, normalization, wavelength calibration, etc.) using a modified version of the DECH20 program package [24]. Dispersion curves for the purpose of establishing the wavelength system were constructed from spectra of scattered sunlight obtained each evening or morning.

3. ANALYSIS OF THE LITHIUM LINE

3.1. Determination of the Parameters of the Stars

In order to determine the atmospheric Li abundances, the basic parameters of the studied stars must be known. We determined the effective temperatures of the stars using various photometric indices for the stars (primarily in the Johnson system) found in various studies. The temperature was calculated using the calibrations of [25], based on the Infrared-Flux Method. Table 2 presents the selected color indices, as well as the calculated and averaged (and, for comparison, previously published) effective temperatures for the studied stars. References to the published color indices are given in square brackets. The last column contains the spectroscopic temperatures derived from the Balmer hydrogen lines by Fuhrmann [31, 34]. In most cases, the spectroscopic temperatures are somewhat higher than those derived from the photometric indices. As we can see from Table 2, the photometric data are fairly inhomogeneous, resulting in appreciable scatter of the temperatures; however, the average T_{eff} values used in the calculations are equal to the results of previous studies within the errors.

We calculated the gravitational accelerations ($\log g$) using the HIPPARCOS trigonometric parallaxes [28]. Table 3 presents the resulting absolute magnitudes and surface gravities, M_v and $\log g$. The errors in $\log g$ were 0.1–0.2 dex.

The average effective temperature calculated for 12 stars is 5758 K, which is very close to the solar value determined with the same calibrations ($T_{eff}(\odot) = 5768$ K). In most cases, the surface gravities indicate that the object is a dwarf; however, fewer than half of the stars display $\log g$ values close to the solar value (4.44 dex).

Table 1. Observations

Night number	Spectrum	Star HD number	Date	Time	Exposure, min
T014	t01406	HD 159 222	21 Jul 98	22 h 56 m	60
	t01407	HD 186 408		23 h 45 m	30
T016	t01609s	HD 187 923	3 Aug 98	00 h 02 m	120
T018	t01805	HD 133 002	6 Aug 98	00 h 06 m	30
	t01810s	HD 34 411		05 h 24 m	40
T019	t01904	HD 146 233	8 Aug 98	22 h 21 m	60
	t01910s	HD 186 408		01 h 14 m	60
	t01912s	HD 186 427		02 h 30 m	60
	t01914s	HD 10 307		04 h 35 m	30
T022	t02215s	HD 4915	12 Aug 98	05 h 20 m	60
T025	t02502s	HD 197 076	16 Aug 98	02 h 28 m	60
	t02504s	HD 4307		04 h 11 m	180
T026	t02604	HD 141 004	17 Aug 98	00 h 06 m	30
	t02606	HD 186 408		01 h 57 m	60
	t02608	HD 186 427		03 h 05 m	60
	t02610s	HD 222 143		04 h 31 m	60

HD 133002, which has been studied little previously, clearly stands out from the sample. It is 100–150 K cooler than the other stars and its surface gravity is lower by roughly an order of magnitude. The chemical composition of its atmosphere is also very different [22]. We suggest that this photometric analogue of the Sun is, in fact, a subgiant that was included in the sample accidentally. This example indicates that the search and selection of solar analogues using purely photometric criteria may not always be correct.

3.2. Equivalent Widths

To study the LiI 6707.8 line in the spectra of the photometric analogues of the Sun, we used the corresponding order of the echelle spectra, which encompasses the wavelength interval 6620–6720 Å. The linear dispersion is 0.075 Å/pix at these wavelengths, and the average signal-to-noise ratio in each spectrum was 200.

We measured the equivalent widths of unblended lines in the studied wavelength interval in all the spectra using the DECH20 code. The number of measured lines for individual stars was 10–30, most being FeI lines. The accuracy in the equivalent widths was 3 mÅ. In several stars, it was not possible to distinguish the lithium line against the noise; the same is true of the spectrum of the solar light scattered in the Earth's atmosphere.

Our analysis of the equivalent widths of the lithium line in the spectra of the studied stars indicates that they can be divided into two groups: those for which the Li 6708 equivalent width is less than 10 mÅ and those for which the Li 6708 equivalent width substantially exceeds this value [36]. Figures 2a and 2b present fragments of the studied spectra at 6700–6712 Å for stars from the first and second groups. The spectra are arranged in order of increasing intensity of the lithium lines. The wavelengths of measured lines are marked.

We can clearly see that, for the stars in the first group (Fig. 2a), the LiI 6707.8 line either disappears in the noise or is weaker than the adjacent FeI 6707.4 line. At the same time, for stars in the second group (Fig. 2b), the intensity of the LiI 6707.8 line appreciably exceeds that of the FeI line. In one of the stars (18 Cet), the lithium line was even stronger than the FeI 6705.1 line!

Along with the stellar spectra, Fig. 2a also presents fragments of spectra from the solar atlas [37] (SUN) and spectra of the twilight sky (SKY).

3.3. Lithium Abundance

The Li abundances A(Li) were determined from the LiI 6708 line profiles or the measured equivalent

Table 2. Color indices and effective temperatures

Star HD number	Color index	Temperature T_{eff}, K	Average T_{eff}, K	T_{eff} from literature, K
HD 4307	$B-V=0.612$ [26]	5794	5776 ± 50	–
	$B-V=1.504$ [27]	5742		
HD 4915	$B-V=0.663$ [28]	5616	5657 ± 50	–
	$V-R=0.543$ [26]	5692		
HD 10 307	$B-V=0.623$ [26]	5755	5815 ± 75	–
	$R-I=0.324$ [29]	5792		
	$B-V=1.39$ [30]	5921		
HD 34 111	$B-V=0.622$ [26]	5758	5803 ± 65	5875 [31]
	$R-I=0.319$ [29]	5825		
	$B-V=1.418$ [32]	5876		
HD 133 002	$B-V=0.671$ [28]	5589	5606 ± 40	–
	$V-K=0.555$ [26]	5634		
HD 141 004	$B-V=0.598$ [33]	5845	5868 ± 65	5864 [34]
	$V-K=1.38$ [30]	5937		
	$R-I=0.321$ [29]	5812		
HD 146 233	$B-V=0.650$ [26]	5660	5709 ± 55	5786 [31]
	$V-K=0.524$ [26]	5786		
	$R-I=0.335$ [35]	5723		
HD 159 222	$B-V=0.639$ [28]	5698	5805 ± 100	5845 [31]
	$V-K=0.510$ [26]	5858		
	$B-V=1.423$ [32]	5868		
HD 186 408	$B-V=0.643$ [28]	5684	5736 ± 65	5805 [34]
	$V-K=0.521$ [26]	5802		
	$B-V=1.477$ [27]	5784		
HD 186 427	$B-V=0.661$ [28]	5623	5700 ± 65	5766 [34]
	$V-K=0.531$ [26]	5751		
	$R-I=0.343$ [29]	5673		
	$B-V=1.494$ [32]	5758		
HD 187 923	$B-V=0.642$ [28]	5688	5700 ± 90	5713 [34]
	$V-K=0.520$ [26]	5807		5729 [31]
	$R-I=0.349$ [29]	5637		
HD 197 076	$B-V=0.611$ [28]	5798	5806 ± 30	–
	$B-V=1.449$ [32]	5828		
HD 222 143	$B-V=0.652$ [26]	5653	5722 ± 100	–
	$V-K=0.522$ [26]	5797		

Table 3. Absolute magnitudes and logarithm of gravities

Star	π, 0.001″	M_v	$\log g$
HD 4307	31.39	3.63	3.98
HD 4915	45.27	5.26	4.59
HD 10 307	79.09	4.45	4.32
HD 34 411	79.08	4.18	4.20
HD 133 002	23.08	2.45	3.45
HD 141 004	85.08	4.07	4.18
HD 146 233	71.30	4.67	4.37
HD 159 222	42.20	4.65	4.39
HD 186 408	46.25	4.32	4.24
HD 186 427	46.70	4.60	4.34
HD 187 923	36.15	3.95	4.08
HD 197 076	47.65	4.82	4.46
HD 222 143	43.26	4.76	4.41

Table 4. Atomic parameters of components of the LiI resonance line

λ, Å	f_{ij}	Isotope	λ, Å	f_{ij}	Isotope
6707.761	0.453	7	6707.912	0.227	7
6707.919	0.037	6	6708.070	0.018	6

Table 5. Parameters of supplementary stars (from the list of Fuhrmann)

Star	T, K	$\log g$	ζ	$v \sin i$	Reference
HD 9407	5663	4.42	3.1	2.0	[31]
HD 95 128	5892	4.27	4.0	1.5	[34]
HD 122 742	5537	4.43	2.6	1.8	[31]
HD 154 345	5507	4.57	2.5	2.4	[34]
HD 157 347	5643	4.31	3.2	2.0	[31]
HD 168 009	5785	4.23	3.8	1.5	[31]
HD 179 957	5738	4.38	3.6	1.0	[31]
HD 179 958	5758	4.32	3.6	1.0	[31]

widths. Synthetic spectra were calculated using the SYNTH code (developed by R. Kurucz, kindly presented to us by V. Tsymbal, and then modified by us), which calculates the profiles of atomic and molecular lines in a local-thermodynamic-equilibrium (LTE) approximation, based on the grid of model atmospheres [38].

In our calculations of the theoretical profiles of the lithium line and adjacent FeI 6703 and 6705 Å lines, we used the atmospheric parameters of the stars determined in the present study. We took the microturbulence velocity (ξ) for all the stars to be 1.0 km/s, based on the weakness of the lines. For some stars, the rotational and macroturbulence (ζ) velocities were taken from the literature; for stars for which these parameters had not been determined previously, we specified them to be within $v \sin i =$ 2.0–3.0 km/s, $\zeta = 2.8$–3.0 km/s (except for λ Aur, Fig. 3b). We also corrected for the instrumental response function, assuming it was a Gaussian whose width corresponded to 4.5 km/s. This form was derived by comparing the line profiles in the atlas [37] with those in the spectrum of scattered solar light.

The calculated LiI 6707.8 line profiles were then compared to the observed profiles. We determined the LTE Li abundance providing the best fit to the observed line profile, then introduced a non-LTE correction. The result was adopted as our final value. Since the LiI line profiles with equivalent widths EW(LiI 6708) < 5 mÅ were distorted by the noise, the abundances A(Li) (or upper limits for them) for these stars were derived from the measured equivalent widths using the non-LTE approach (see Section 3.4).

We used two stars—18 Cet and 18 Sco—as examples to analyze the effects of four input parameters (T_{eff}, $\log g$, ξ, and ζ) on the accuracy of the calculated lithium abundances. The largest error in A(Li) is introduced by uncertainty in the temperature: a temperature error of 100 K leads to an abundance error of up to 0.1 dex. Figure 3a compares the observed spectrum for 18 Cet with three synthetic spectra corresponding to temperatures of 5680, 5780, and 5880 K (for a fixed Li abundance). Variation in $\log g$ by 0.1 dex and in ζ by 0.5 km/s yields insignificant variations in the lithium abundance. Figure 3b presents the theoretical and observed spectra for λ Aur.

3.4. Non-LTE Calculations for LiI

When the LTE approximation must be abandoned, the non-LTE calculations were carried out in accordance with the model described in [39]. They indicate that the populations of the LiI energy states in the atmospheres of the studied stars are not in equilibrium in the region of formation of the lines. Therefore, the measured EW(LiI 6708) values differ from those calculated in an LTE approximation. Figure 4 presents the b factors $\log b_i = \log(n_i/n_i^*)$, which describe the deviation of a level population n_i from the equilibrium value n_i^* as a function of depth in

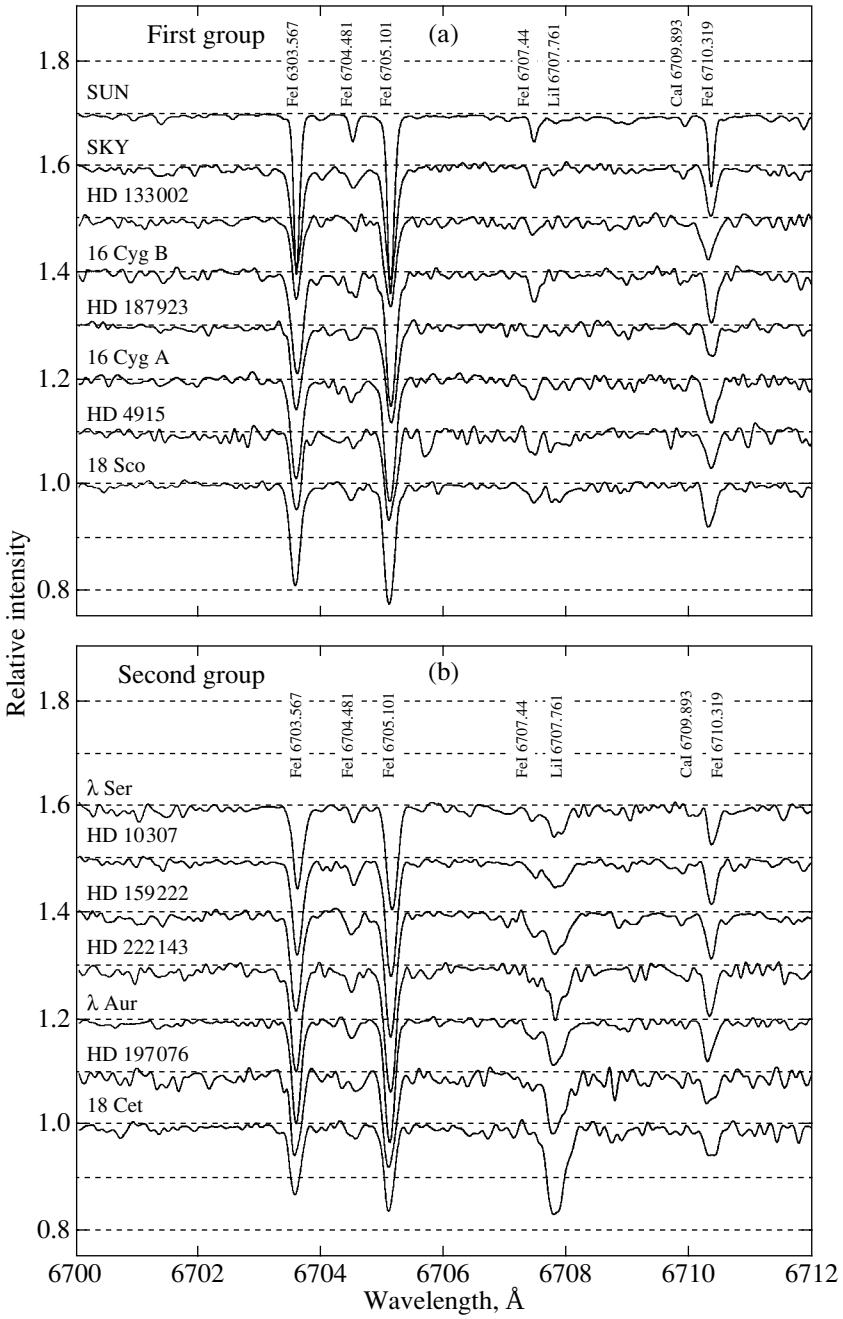

Fig. 2. Spectral fragment in the vicinity of the LiI 6708 line for stars with (a) weak and (b) strong lithium lines.

the atmosphere, for a model atmosphere with $T_{eff} = 5800$ K, $\log g = 4.20$, $[A] = 0$, and $[\mathrm{Li/H}] = 1$, which corresponds to the parameters of λ Aur, for five lower levels of Li. In deep layers with $\log \tau_{1\mu}$ values from 0.5 to -0.3, both the lower ($2s$) and upper ($2p$) level are overpopulated relative to their equilibrium state. This overpopulation has two origins: (i) recombinations dominate over ionizations for highly excited levels whose ionization thresholds lie in the IR, where the mean intensity J_ν, which specifies the photoionization rate, is lower than the local $B_\nu(T_e)$, which in part specifies photorecombination rates; (ii) due to subsequent cascade transitions to lower levels. In these layers, the medium also becomes transparent to radiation beyond the $2p$ ionization threshold, $\lambda_{thr}(2p) = 3496$ Å; however, the mean intensity in this interval exceeds the local $B_\nu(T_e)$. Therefore, when $\log \tau_{1\mu} \leq -0.3$, photoionization depopulates the $2p$ level and the related ground state. The overpopulation of the $2s$ level when $\log \tau_{1\mu} \geq -0.3$ strengthens the line com-

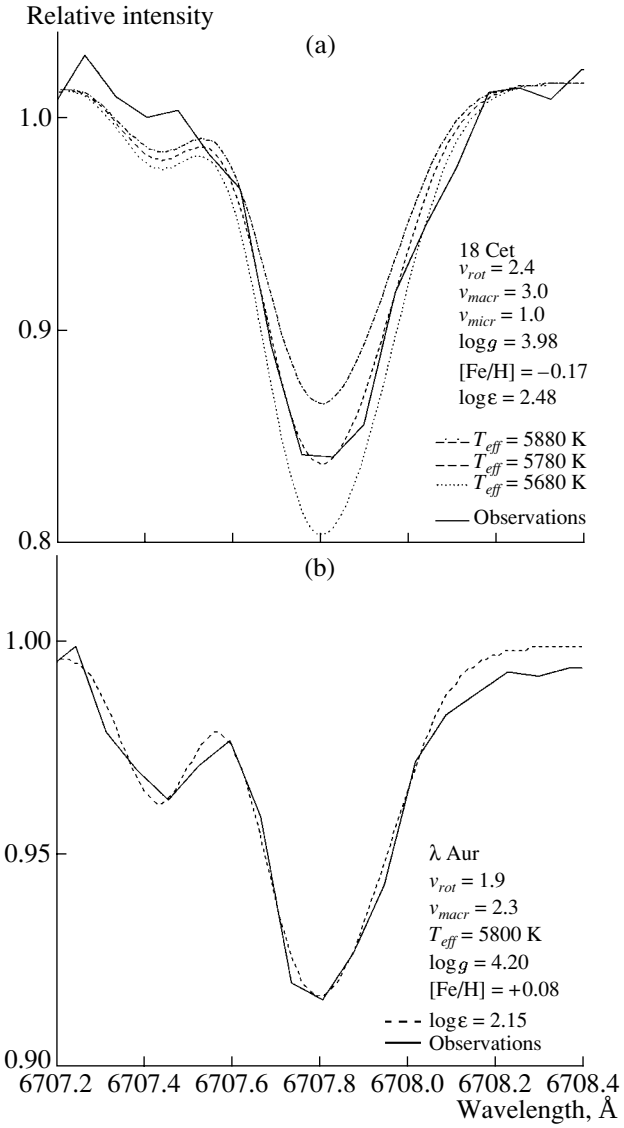

Fig. 3. (a) Observed LiI 6708 line profile in the spectrum of 18 Cet and three synthetic profiles differing by 100 K (their parameters are indicated in the figure). (b) Synthetic (dashed) and observed (solid) LiI 6708 line profiles for λ Aur.

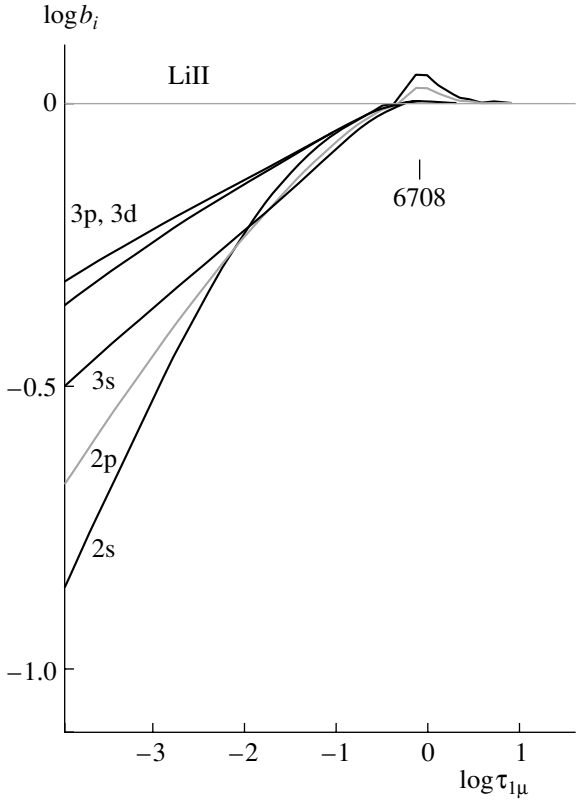

Fig. 4. The b-factors for the LiI levels as a function of depth in the atmosphere of a star with $T_{eff} = 5800$ K, $\log g = 4.20$, $[A] = 0$, and [Li/H] = 1. The vertical dash indicates the depth of formation of the radiation in the core of the LiI resonance line.

pared to the LTE case, and the depopulation of levels in higher layers has the reverse effect—weakening of the line. Therefore, overall, the non-LTE deviations in the LiI line are small. In all the studied stars, the non-LTE corrections to the lithium abundances are positive and lie in the range from 0.04 to 0.11 dex (see Table 6).

The non-LTE calculations were carried out using the NONLTE3 code [40], which is based on the method of complete linearization (the version developed by Auer and Heasley [41]). When calculating the opacities, in addition to the usual contributions from HI, H^-, H_2^+, abundant heavy elements, and electron and Raleigh scattering, we also took into account the contributions of numerous spectral lines via a direct summation of their absorption factors at each frequency. Our line list is based on that of Kurucz [38] and contains about 150 000 lines with wavelengths exceeding 912 Å.

Lithium is a mixture of the isotopes ^{6}Li and ^{7}Li. The isotope ^{7}Li dominates in the solar system, and the ratio of the isotopic abundances is $^6\mathrm{Li} : {}^7\mathrm{Li} = 7.5 : 92.5$, according to the data of Anders and Grevesse [42]. Due to the fine splitting of levels, the resonance line of each of the isotopes has two components. The isotopic shift for lithium (158 mÅ) [43] is comparable to the distance between the fine splitting components (151 mÅ). The hyperfine splitting of levels of ^{7}Li is very small and does not increase the separation between the components to more than 13 mÅ. This is substantially smaller than the isotopic shift and has essentially no effect on the final LiI 6708 line profiles and equivalent widths. As a result, we consider four components for the resonance line, whose parameters are presented in Table 4 along

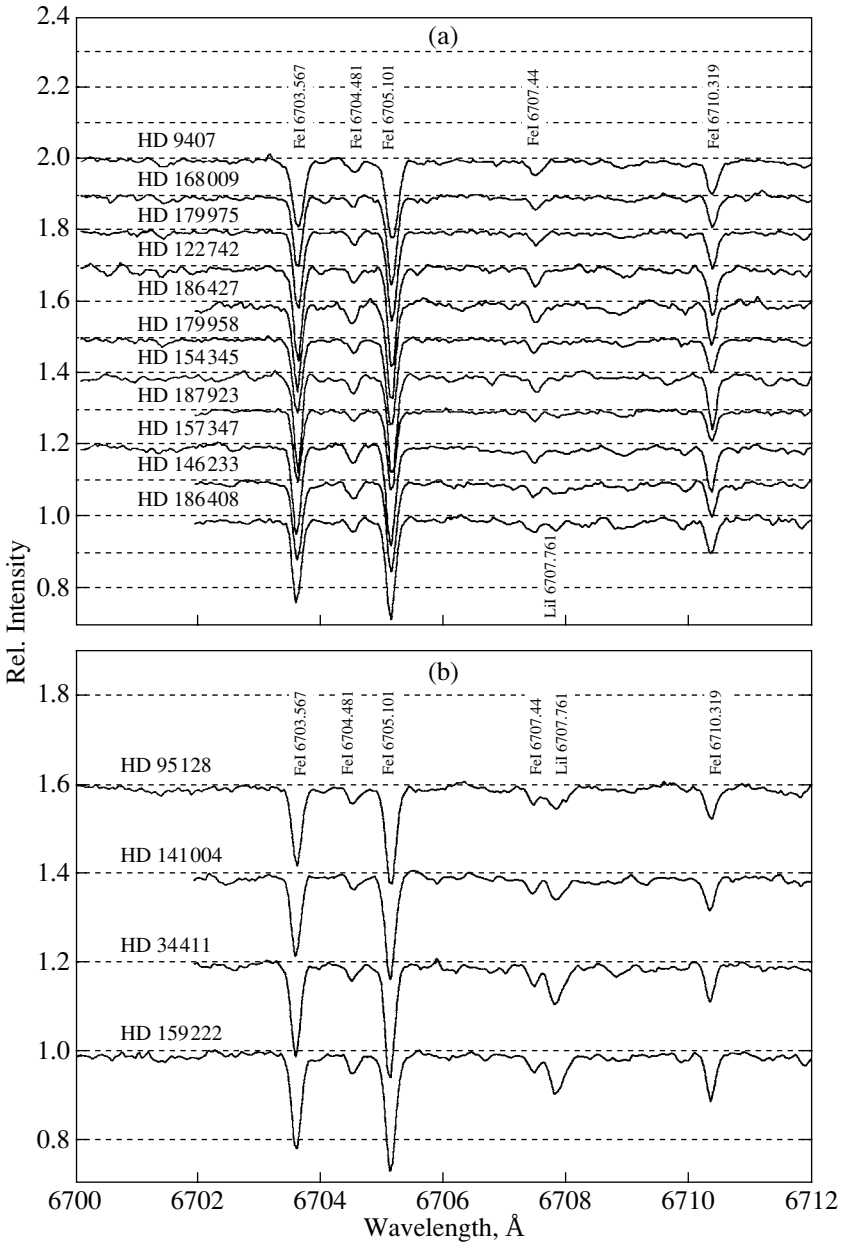

Fig. 5. (a) Same as Fig. 2a for stars from the supplementary sample. (b) Fragment of the spectrum in the vicinity of the LiI 6708 line for four stars with strong lithium lines (from the list of Fuhrmann).

with the mass number of the isotope responsible for the formation of a given component. The oscillator strengths f_{ij} were calculated for the solar ratio of the lithium-isotope abundances.

Natural damping was taken into account using the value $\gamma_R = A_{21}$, and pressure effects, using the classical Unsold constant C_6 [44] and $\gamma_4 = 10^{-8} n_e n_{eff}^5$, where n_e is the electron density and n_{eff} the effective main quantum number. Note, however, that the observed equivalent widths for the LiI 6708 line usually do not exceed 30 mÅ, so that pressure effects are negligible.

Model atmospheres with the specified parameters were interpolated in the model grid of Kurucz [38] using code developed by Yu. Pimenov, V. Suleĭmanov, and V. Shimanskiĭ.

3.5. The Additional Sample

To compare our results with independent observations, we analyzed another 15 spectra of solar-type stars kindly presented to us by Klaus Fuhrmann (Institute for Astronomy and Astrophysics, University

Table 6. LiI 6708 equivalent widths and LTE and non-LTE Li abundances

Star	Terskol observations			Calar Alto observations			Reference
HD	EW(Li)	$A(\mathrm{Li})_{LTE}$	$A(\mathrm{Li})_{NLTE}$	EW(Li)	$A(\mathrm{Li})_{LTE}$	$A(\mathrm{Li})_{NLTE}$	$A(\mathrm{Li})_{lit}$
4307	61.5	2.44	2.48	–	–	–	
4915	4.7	1.08	1.19	–	–	–	
9407	–	–	–	≤ 2.0	–	≤ 0.82	
10 307	23.1	1.95	2.02	–	–	–	≤ 1.85 [46]
34 411	28.3	2.09	2.15	24.0	2.08	2.14	2.00 [7]
95 128	–	–	–	13.0	1.94	2.00	≤ 1.70 [47]
122 742	–	–	–	≤ 2.0	0.62	0.72	
141 004	18.9	1.99	2.05	11.9	1.84	1.90	1.88 [6]
146 233	11.8	1.62	1.72	8.0	1.47	1.57	1.58 [46]
154 345	–	–	–	≤ 2.0	–	≤ 0.68	
157 347	–	–	–	≤ 2.0	–	≤ 0.80	
159 222	24.1	2.09	2.16	24.0	2.07	2.14	
168 009	–	–	–	≤ 2.0	0.82	0.91	
179 957	–	–	–	≤ 2.0	–	≤ 0.86	
179 958	–	–	–	≤ 2.0	–	≤ 0.88	
186 408	4.3	1.12	1.21	5.0	1.17	1.28	1.27 [48]
186 427	≤ 2.0	0.75	0.77	≤ 2.0	–	≤ 0.90	≤ 0.60 [2]
187 923	4.0	1.06	1.16	3.0	0.93	1.03	
197 076	35.8	2.26	2.33	–	–	–	
222 143	25.7	2.01	2.08	–	–	–	

of Munich). The observations were similar to ours: the spectra were obtained in 1996–2000 with the 2.2-m Calar Alto Telescope (Spain) using the FOCES echelle spectrometer [45], which has a resolution of 60 000. Figures 5a and 5b present fragments of these spectra at wavelengths of 6700–6712 Å. They are divided according to the intensity of the LiI 6708 line in the same way as in Fig. 2: the upper panel displays spectra in which this line is weak, whereas the lower panel shows spectra in which it is fairly intense.

Of the 15 stars whose spectra were obtained by Fuhrmann, seven are common with our sample and eight are supplementary. The stars were selected by Fuhrmann based the proximity of their basic stellar parameters to the solar values. Table 5 presents the temperatures T_{eff}, surface gravities $\log g$, macroturbulence velocities ζ, and rotational velocities $v \sin i$ for the eight supplementary stars taken from [31, 34]. These parameters were used in the calculations.

The determination of the continuum level, measurement of the equivalent widths, and calculation of the synthetic profiles and non-LTE abundances for the additional spectra were carried out using the same programs and techniques as for our spectra, described above.

4. THE Li ABUNDANCES AND TEMPERATURE IN SOLAR ANALOGUES

Table 6 presents the main results of our study. It contains the LiI equivalent widths and the LTE and non-LTE lithium abundances for 20 stars; the Terskol Observatory data are placed on the left, and Calar Alto data, on the right. It is clear that the differences in A(Li) derived using the data obtained at the two

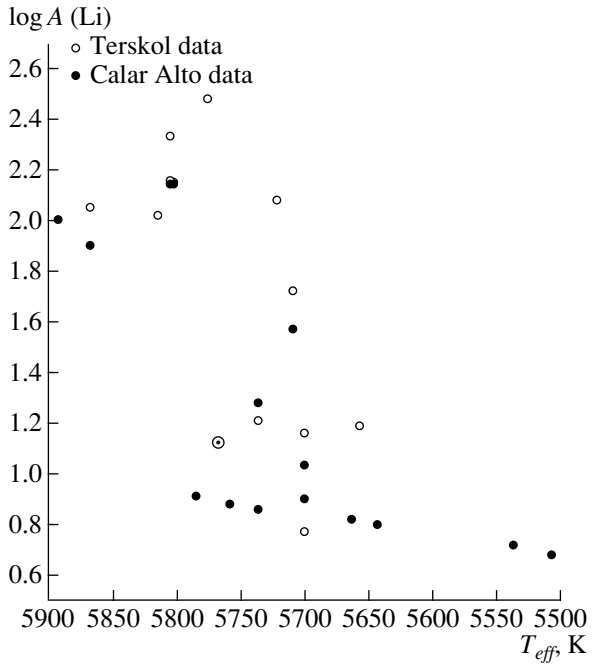

Fig. 6. Plot of lithium abundance vs. effective temperature for the studied solar analogues. The open and filled circles indicate the abundances derived from the Terskol Observatory and Calar Alto Observatory data, respectively.

observatories and with two similar detectors do not exceed 0.15 dex. The last column contains previously published lithium abundances.

Table 6 provides evidence that the Li abundances in stars with weak and strong LiI 6707.8 lines differ by roughly an order of magnitude or even more, giving rise to the formation of the two groups noted above (see Sections 3.2 and 3.3). Only HD 146233 (=18 Sco), which was artificially placed in the first group based on its equivalent width [36], displays an intermediate Li abundance ($A(\mathrm{Li}) = 1.72$ dex).

The stars in the two groups differ not only in their lithium abundances but also in their effective temperatures. The mean temperatures of stars from the first and second groups are 5700 and 5800 K. This means that the stars with higher effective temperatures also have higher lithium abundances. The stars from the supplementary sample conform to this dependence: for example, the effective temperature of HD 95128 (47 UMa) is close to 5900 K and its Li abundance is 2.0 dex, while the other stars with temperatures below 5600 K have $A(\mathrm{Li}) = 1.0$ dex.

Figure 6 presents the temperature distribution for the lithium abundances for all 20 studied stars; the filled and open circles denote data derived from spectra obtained at the Terskol and Calar Alto Observatories, respectively. Stars with stronger LiI 6707.8 lines (i.e., with higher lithium abundances) are located in the region of the plateau (Fig. 1), while stars with reduced lithium abundances occupy the region to the right and downward, which is also consistent with the published data. The symbol $\odot$ marks the position of the Sun ($A(\mathrm{Li})_\odot = 1.16$ dex) in the $A(\mathrm{Li})$–T_{eff} diagram, based on the data [49]. It is clear that the Sun belongs to the first group of stars.

5. CONCLUSIONS

We have studied the atmospheric lithium abundances derived from the Li in stars that are photometric analogues of the Sun. We obtained spectroscopic observations of 13 such stars. Using previously published data, we calculated the main parameters of their atmospheres. We measured the equivalent widths of the LiI line and determined both LTE and non-LTE lithium abundances (the non-LTE corrections for the stars are all 0.04–0.11 dex).

The stars studied can be divided into two groups according to their lithium abundances: (1) stars with Li abundances close to the solar value and (2) stars whose Li abundances are an order of magnitude higher. The stars, which cover a narrow temperature interval, follow the temperature versus Li abundance dependence typical for cool stars.

Our results are confirmed by independent observations of seven common and eight supplementary stars whose spectra were obtained using a similar telescope and spectrograph. The maximum difference between the Li abundances for the stars in common to the two samples is 0.15 dex.

The first group of stars (with weak Li lines) includes 16 Cyg A, 16 Cyg B, and 18 Sco, which were identified as candidate solar twins in other studies. The last star is the most probable solar twin, as is confirmed by our study of the chemical compositions of the photometric analogues of the Sun [22]; however, it displays a modest overabundance of Li compared to the Sun.

Since the sample of solar analogues was selected purely photometrically, one subgiant was erroneously included in the sample.

ACKNOWLEDGMENTS

The authors thank the staff of the Terskol Observatory for their assistance with the July–August 1998 observations, as well as Klaus Fuhrmann, who kindly presented us with his data. The non-LTE calculations were carried out using a personal computer presented by the Kazan Astronomical and Geodetic Society. This work was supported by the Russian Foundation for Basic Research (project nos. 99-02-17488, 02-02-17174, 02-02-17423) and a grant from the Program for Support of Leading Scientific Schools of the Russian Federation (NSh-1789.2003.2). A.I. Galeev is particularly grateful to the Russian Foundation for Basic Research for an MAS grant (MAC 01-02-06068).

REFERENCES

1. C. P. Deliyannis, in *The Light Elements Abundances*, Ed. by P. Crane (Springer, Berlin, 1995), p. 395.
2. J. R. King, C. P. Deliyannis, D. D. Hiltgen, *et al.*, Astron. J. **113**, 1871 (1997).
3. C. P. Deliyannis, A. M. Boesgaard, A. Stephens, *et al.*, Astrophys. J. **498**, L147 (1998).
4. D. L. Lambert, J. E. Heath, and B. Edvardsson, Mon. Not. R. Astron. Soc. **253**, 610 (1991).
5. L. Pasquini, Q. Liu, and R. Pallavicini, Astron. Astrophys. **287**, 191 (1994).
6. F. Favata, G. Micela, and S. Sciortino, Astron. Astrophys. **311**, 951 (1996).
7. A. Lebre, P. de Laverny, J. R. de Medeiros, *et al.*, Astron. Astrophys. **345**, 936 (1999).
8. S. Randich, R. Gratton, R. Pallavicini, *et al.*, Astron. Astrophys. **348**, 487 (1999).
9. J. A. Thorburn, Astrophys. J. **421**, 318 (1994).
10. S. Balachandran, Astrophys. J. **354**, 310 (1990).
11. S. G. Ryan and C. P. Deliyannis, Astrophys. J. **500**, 398 (1998).
12. S. G. Ryan, T. C. Beers, T. Kajino, and K. Rosolankova, Astrophys. J. **547**, 231 (2001).
13. D. R. Soderblom, J. R. King, L. Siess, *et al.*, Astron. J. **118**, 1301 (1999).
14. S. Randich, L. Pasquini, and R. Pallavicini, Astron. Astrophys. **356**, 25 (2000).
15. S. P. Strom, in *Cool Stars, Stellar Systems and the Sun*, Ed. by J-P. Caillault, ASP Conf. Ser. **64**, 211 (1995).
16. B. F. Jones, D. Fischer, and D. R. Soderblom, Astron. J. **117**, 330 (1999).
17. S. G. Ryan, Mon. Not. R. Astron. Soc. **316**, 35 (2000).
18. G. Gonzalez and G. Wallerstein, Astron. J. **117**, 2286 (1999).
19. C. Abia, Y. Pavlenko, and P. de Laverny, Astron. Astrophys. **351**, L273 (1999).
20. S. G. Ryan, T. Kajino, T. C. Beers, *et al.*, Astrophys. J. **549**, 55 (2001).
21. A. V. Kharitonov and A. V. Mironov, in *Solar Analogues: Characteristics and Optimum Candidates*, Ed. by J. Holl (1998), p. 149.
22. A. I. Galeev, I. F. Bikmaev, F. A. Musaev, and G. A. Galazutdinov, Astron. Zh. **81** (2004, in press).
23. F. A. Musaev, G. A. Galazutdinov, A. V. Sergeev, *et al.*, Kinemat. Fiz. Neb. Tel **13**, 282 (1999).
24. G. A. Galazutdinov, Preprint Spets. Astrofiz. Obs. Ross. Akad. Nauk **92**, 1 (1992).
25. A. Alonso, S. Arribas, and C. Martinez-Roger, Astron. Astrophys. **313**, 873 (1996).
26. V. G. Kornilov, I. M. Volkov, A. I. Zakharov, *et al.*, *Catalog of WBVR Magnitudes of Bright Stars of the Northern Sky*, Tr. Gos. Astron. Inst. Sternberga **63**, 1 (1991).
27. A. Alonso, S. Arribas, and C. Martinez-Roger, Astron. Astrophys., Suppl. Ser. **117**, 227 (1996).
28. *The HIPPARCOS and TYCHO Catalogues*, ESA-SP-1200 (1997).
29. B. J. Taylor, Publ. Astron. Soc. Pac. **106**, 452 (1994).
30. J. Fernley, H. Neckel, E. Solano, and W. Wamsteker, Astron. Astrophys. **311**, 245 (1996).
31. K. Fuhrmann, private communication (2000).
32. G. P. Di Benedetto, Astron. Astrophys. **339**, 858 (1998).
33. T. Oja, Astron. Astrophys. **286**, 1006 (1994).
34. K. Fuhrmann, Astron. Astrophys. **338**, 161 (1998).
35. M. S. Bessell, Astron. Astrophys., Suppl. Ser. **83**, 357 (1990).
36. A. I. Galeev, I. F. Bikmaev, F. A. Musaev, and G. A. Galazutdinov, Roman. Astron. J. Suppl. **9**, 137 (1999).
37. R. L. Kurucz, I. Furenlid, J. Brault, and L. Testerman, *Solar Flux Atlas from 296 to 1300 nm* (KPNO, Tucson, 1984).
38. R. L. Kurucz, CD-ROMs, *ATLAS9 Stellar Atmospheres Programs and 2 km/s Grid* (Cambridge, 1993).
39. L. I. Mashonkina, A. V. Shavrina, V. Khalak, *et al.*, Astron. Zh. **79**, 31 (2002) [Astron. Rep. **46**, 27 (2002)].
40. N. A. Sakhibullin, Tr. Kazan. Gos. Astron. Obs. **48**, 9 (1983).
41. L. H. Auer and J. Heasley, Astrophys. J. **205**, 165 (1976).
42. E. Anders and N. Grevesse, Geochim. Cosmochim. Acta **53**, 197 (1989).
43. A. A. Radtsig and B. M. Smirnov, *Parameters of Atoms and Atomic Ions* (Énergoatomizdat, Moscow, 1986) [in Russian].
44. A. Unsöld, *Physik der Sternatmosphären*, 2nd ed. (Springer, Berlin, 1955).
45. Pfeiffer *et al.*, Astron. Astrophys., Suppl. Ser. **130**, 381 (1998).
46. A. Stephens, A. M. Boesgaard, J. R. King, *et al.*, Astrophys. J. **491**, 339 (1997).
47. D. K. Duncan, Astrophys. J. **248**, 651 (1981).
48. L. S. Lyubimkov, *Chemical Compositions of Stars* (Astroprint, Odessa, 1995) [in Russian].

Translated by K. Maslennikov

Astronomy Reports, Vol. 48, No. 6, 2004, pp. 522–524. Translated from Astronomicheskiĭ Zhurnal, Vol. 81, No. 6, 2004, pp. 574–576.

Near-Polar Starspots and Polar Dynamo Waves

S. V. Novikov[1], N. E. Piskunov[2], and D. D. Sokoloff[1]

[1] *Moscow State University, Moscow, Russia*

[2] *Institute of Astronomy and Space Physics, Uppsala University, Uppsala, Sweden*

Received September 28, 2003; in final form, November 11, 2003

Abstract—A possible mechanism for the formation of near-polar magnetic spots on some stars with convective envelopes is proposed. The mechanism is based on the idea that the maximum of the dynamo waves that are excited in thin convective shells by the dynamo mechanism is shifted appreciably from the maximum of the magnetic-field sources in the direction of motion of the dynamo wave. If there is no region of super-rotation near the equator for some reason (as a consequence of disruption due to tidal interaction with a companion in a binary system, for example) and the wave of stellar activity propagates toward the poles rather than toward the equator, this maximum will be in the near-polar regions.

Sunspots, which reflect the solar-activity cycle, are encountered primarily at relatively low latitudes. This fits in well with solar-dynamo theory, which associates solar activity with the propagation of a toroidal magnetic-field wave near the base of the convective zone. This wave, called a dynamo wave, is born at middle latitudes and propagates toward the solar equator during the solar cycle.

Of course, cyclic activity and spots are also encountered on other stars, but they are not always similar to sunspots. In particular, spots in near-polar regions have been reported for a number of stars [1–4]. Note that, in all known cases of near-polar starspots, the activity level appreciably exceeds that for the Sun, and polar spots are detected either on active stars in close binary systems (RS CVN stars) or on stars that have formed as a result of a merger of a binary system (FK Comae). Although the methods developed to reconstruct the temperature distributions over stellar surfaces, and thereby identify cool stellar spots, have limited applicability in near-polar regions, the existence of high-latitude spots in at least some stars is beyond doubt. This must somehow be explained by the dynamo theory, although there is no reason to expect that this explanation need necessarily be universal.

One obvious possible reason for the appearance of spots in the near-polar regions of some stars would be that the internal structure of these stars is such that their dynamo waves propagate toward the poles rather than toward the equator [5]. The direction of the dynamo wave's motion is determined by the sign of the product of the helicity of the convective motions and the radial shift of the angular velocity in the part of the convective zone where the dynamo mechanism operates efficiently. It is convenient to characterize this product by the so-called dynamo number D, which is defined such that the correct direction for the propagation of solar dynamo waves corresponds to $D < 0$. Data on the solar differential rotation obtained from helioseismological measurements [6–8] and helicity computations for the convective zone of the Sun [9, 10] indicate that the solar dynamo wave propagates toward the equator, although the signs of the factors involved have sometimes been revised during the development of helioseismological techniques and the solar-dynamo theory. It therefore seems likely that the dynamo waves in some stars propagate toward their poles. Indeed, according to our current understanding, the direction of propagation of the solar dynamo wave is determined by the presence of a region of super-rotation [7] in the near-equatorial zone of the Sun; however, it is quite plausible that the region of super-rotation in close binary systems is disrupted by tidal interactions [11], so that the dynamo number becomes positive. Hints of waves of activity propagating toward the poles are provided by the observational data for some stars [4].

It is clear that a detailed study of possible scenarios for the appearance of spots in near-polar regions must be based on the construction of fairly complex models for the stellar dynamo using numerical methods. However, it seems expedient first to identify the proposed effect in fairly simple models that admit analytical analysis. This is the aim of the present paper.

Let us consider the self-excitation of a dynamo wave in a Parker approximation [12]. This approximation considers an axially symmetrical dynamo wave

1063-7729/04/4806-0522$26.00

in a thin convective zone; the toroidal magnetic-field strength B and the quantity A, which is proportional to the toroidal component of the vector potential and describes the longitudinal magnetic field, are considered as functions of the latitude θ measured from the equator, while the radial dependence of these functions is neglected. In this case, the mean-field electrodynamical equations have the form [13]

$$\frac{\partial A}{\partial t} = \alpha(\theta)B + \frac{\partial^2 A}{\partial \theta^2}, \quad (1)$$

$$\frac{\partial B}{\partial t} = -D\cos\theta\frac{\partial A}{\partial \theta} + \frac{\partial^2 B}{\partial \theta^2}. \quad (2)$$

Here, we assume for simplicity that the toroidal field is formed from the longitudinal field purely due to differential rotation (which has only a radial shift; this is the $\alpha\omega$-dynamo approximation), neglect the curvature of the convective zone, and assume that the magnitude of the shift is constant with latitude, so that it can be absorbed into the dynamo number. Equations (1) and (2) are supplemented by the boundary conditions at the pole and equator. To demonstrate the physical effect in question, we chose the simplest latitude distribution (that is still consistent with the antisymmetry of the helicity about the solar equator), $\alpha = \sin\theta$, and include the amplitude of this function in the defintion of the dynamo number. We must compare the behavior of growing (and oscillating) solutions of (1) and (2) for negative and positive values of D.

We selected the distribution of magnetic-field sources such that the dynamo operates most intensely halfway between the pole and equator, at $\theta = 45°$. The essence of the proposed effect is that the maximum amplitude of the dynamo wave excited by this configuration of sources is not located at latitude $\theta = 45°$. As was shown by Kuzanyan and Sokolov [14], in the case of negative and large-amplitude dynamo numbers, this maximum is appreciably shifted toward the equator. To convince oneself of this fact, it is useful to consider the solution of (1) and (2) in the form of a traveling wave with a large wave vector, $k|D|^{1/3}$, where we have explicitly written the dependence on the dynamo number. It turns out that, due to Eqs. (1) and (2), the wave vector satisfies the equation

$$(\Gamma_0 + k^2)^2 - i\alpha\cos\theta k = 0, \quad (3)$$

which is analogous to the Hamilton–Jacobi equation in the quasi-classical approximation in quantum mechanics. Here, $\Gamma_0|D|^{2/3}$ is the complex growth rate of the dynamo wave, where we have again explicitly written the dependence on the wave number. The imaginary part of the growth rate determines the length of the cycle.

Equation (3) is a fourth-order algebraic equation in k that depends on the latitude as one of its parameters. We are interested in a solution that is continuous at all latitudes and decreases near the poles and at the equator. Kuzanyan and Sokolov [14] showed that this solution exists only for a single (more precisely, two complex-conjugate) value of Γ_0, with $\mathrm{Re}\,\Gamma_0 > 0$. The wave number k is an appreciably complex quantity, with $\mathrm{Im}\,k = 0$ when $\theta \approx 27°$. We can readily see that this is the condition that the amplitude of the dynamo wave be maximum in the short-wavelength approximation we are considering.

Thus, the maximum of the solar dynamo wave propagating from middle latitudes toward the equator is located approximately halfway between the equator and the maximum in the distribution of the magnetic-field sources. It is evident that the distribution of sunspots reflects this tendency.

Kuzanyan and Sokolov [14] did not consider the case of positive dynamo numbers directly, but the corresponding calculations are straightforward, and we omit them here. It is important that we obtain as a result the following Hamilton–Jacobi equation:

$$(\Gamma_0 + k^2)^2 + i\alpha\cos\theta k = 0, \quad (4)$$

which differs from (3) in the sign of the second term. It is clear that a change in the sign of the dynamo number reduces to a change in the direction of propagation of the dynamo wave, so that it reaches its maximum at an angle 27° from the pole, i.e., at latitude $\theta = 63°$. This is the essence of the proposed effect.

This result is expected but not trivial. In fact, the latitude propagation of the dynamo wave is not associated with a latitude shift of the stellar material, or even a shift of the sunspots (it is the places where the spots arise that drift). Therefore, the shift in the dynamo-wave maximum from the source maximum is a nontrivial effect. The boundary problem for Eqs. (1) and (2) does not exhibit precise symmetry upon changing the sign of the dynamo number due to the asymmetry of the conditions at the pole and equator. The symmetry arises only at the level of the Hamilton–Jacobi equations. Nevertheless, the shift of the dynamo-wave maximum when the direction of propagation is changed is appreciable (in our model, about 36°) and can explain the appearance of near-polar spots in some stars, at least in a kinematic approximation.

ACKNOWLEDGMENTS

This work was supported by the Russian Foundation for Basic Research (project no. 01-02-17693).

REFERENCES

1. A. P. Hatzes, S. S. Vogt, T. F. Ramseyer, and A. Misch, Astrophys. J. **469**, 808 (1996).
2. K. Oláh, K. G. Strassmeier, and M. Weber, Astron. Astrophys. **389**, 202 (2002).
3. K. G. Strassmeier and J. B. Rice, Astron. Astrophys. **399**, 315 (2003).
4. S. S. Vogt, A. P. Hatzes, A. A. Misch, and M. Kürster, Astrophys. J., Suppl. Ser. **121**, 547 (1999).
5. G. Belvedère, A. F. Lanza, and D. D. Sokoloff, Sol. Phys. **183**, 435 (1998).
6. J. Schou, H. M. Anita, S. Basu, *et al.*, Astrophys. J. **505**, 390 (1998).
7. A. G. Kosovichev, J. Schou, P. M. Scherrer, *et al.*, Sol. Phys. **170**, 43 (1997).
8. M. J. Thompson, J. Toomre, E. Anderson, *et al.*, Science **272**, 1300 (1996).
9. S. D. Bao, A. A. Pevtsov, T. J. Wang, and H. Q. Zhang, Sol. Phys. **195**, 75 (2000).
10. A. A. Pevtsov, R. C. Canfield, and T. R. Metcalf, Astrophys. J. **440**, L109 (1995).
11. D. D. Sokoloff and N. Piskunov, Mon. Not. R. Astron. Soc. **334**, 925 (2002).
12. E. N. Parker, Astrophys. J. **122**, 293 (1955).
13. F. Krause and K. H. Rädler, *Mean-Field Magnetohydrodynamics and Dynamo Theory* (Pergamon Press, Oxford, 1980).
14. K. M. Kuzanyan and D. D. Sokoloff, GAFD **81**, 113 (1995).

Translated by D. Gabuzda